

Electronic Thesis and Dissertation Repository

2-24-2023 10:30 AM

Investigating the structure of Metal-Organic Frameworks and the behaviors of adsorbed guest molecules in MOFs via Solid-state NMR Spectroscopy

Yihao Shen, *The University of Western Ontario*

Supervisor: Huang, Yining, *The University of Western Ontario*

A thesis submitted in partial fulfillment of the requirements for the Master of Science degree in Chemistry

© Yihao Shen 2023

Follow this and additional works at: <https://ir.lib.uwo.ca/etd>

 Part of the [Inorganic Chemistry Commons](#), and the [Materials Chemistry Commons](#)

Recommended Citation

Shen, Yihao, "Investigating the structure of Metal-Organic Frameworks and the behaviors of adsorbed guest molecules in MOFs via Solid-state NMR Spectroscopy" (2023). *Electronic Thesis and Dissertation Repository*. 9139.

<https://ir.lib.uwo.ca/etd/9139>

This Dissertation/Thesis is brought to you for free and open access by Scholarship@Western. It has been accepted for inclusion in Electronic Thesis and Dissertation Repository by an authorized administrator of Scholarship@Western. For more information, please contact wlsadmin@uwo.ca.

Abstract

Metal-organic frameworks (MOFs) are a class of hybrid organic-inorganic microporous materials with lots of significant applications including gas capture and storage, gas separation, batteries, catalysis, ion exchange and drug delivery. MOFs based on s-block metals are important due to their many practical applications. These MOFs are also very interesting because the s-block MOFs often exhibit unpredictable behavior of coordination. In this thesis, the structures of six s-block metal (Li, Na, Cs, Mg, Ca, Sr) based MOFs involving V-shaped link, 4, 4'-sulfonyldibenzoate (SDB) are characterized by various techniques including, powder X-ray diffraction, TGA and solid-state NMR spectroscopy. ^{13}C CPMAS NMR was used to probe the local structure around SDB linkers. ^7Li , ^{23}Na , ^{133}Cs , and ^{25}Mg SSNMR were utilized to directly characterize the metal center surroundings. Explicitly, variable temperature (VT) ^{13}C SSNMR spectroscopy is used to investigate the behavior of $^{13}\text{CO}_2$ in four selected MOFs with porous channels. The analysis of ^{13}C static spectra reveals that CO_2 molecules undergo localized wobbling and non-localized hopping within these MOFs. Additionally, all these s-block MOFs based on SDB ligands share the common adsorption site (π -pocket of SDB ligands). Moreover, another novel MOF, UTSA-280, with Ca center and C_4O_4 ligands is also studied. Based on its rigid channel size, UTSA-280 shows a high separation performance of CO_2 from CH_4 and C_2H_4 from C_2H_6 under ambient condition. In this thesis, the behaviors of $^{13}\text{CO}_2$ and C_2D_2 within UTSA-280 are investigated via VT ^{13}C wide-line SSNMR experiments and VT ^2H wide-line SSNMR experiments, respectively. The results show a tight guest-host interactions. Meanwhile, with the same ligands as UTSA-280, MOF $(\text{Zn}(\text{bipy})(\text{C}_4\text{O}_4)(\text{H}_2\text{O})_2)$ is studied as well.

Keywords:

MOFs, s-block metals, H_2SDB , solid-state NMR, CO_2 dynamics, squaric acid.

Summary of Lay Audience

Metal-organic frameworks (MOFs) are a class of materials composed of metal centers linked by organic ligands. Most MOFs have porous channels, in this case, they can be widely used in gas capture and storage, gas separation, batteries, catalysis, ion exchange and drug delivery. MOFs based on s-block metals are important due to their many practical applications. These MOFs are also very interesting because the s-block MOFs often exhibit unpredictable geometry around the metal centers. In this thesis, the structures of six s-block metal (Li, Na, Cs, Mg, Ca, Sr) based MOFs involving V-shaped link, 4, 4'-sulfonyldibenzoate (SDB) are characterized by various techniques to confirm the structure of the sample obtained is consistent with the one discussed in literature. For four selected MOFs with porous channels, the behaviors of $^{13}\text{CO}_2$ within frameworks are revealed by variable temperature (VT) ^{13}C SSNMR spectroscopy. The results show the CO_2 molecules are jumping between two sites in channels while rotating itself at the same time. The MOFs based on another ligand, C_4O_4 , are also studied. Especially, USTA-280, which is a Ca based MOF, shows a high separation performance of CO_2 from CH_4 and C_2H_4 from C_2H_6 under ambient condition, due to rigid porous channels size. In this thesis, the behaviors of $^{13}\text{CO}_2$ within frameworks are revealed by variable temperature (VT) ^{13}C SSNMR spectroscopy; the behaviors of C_2D_2 within frameworks are revealed by VT ^2H SSNMR spectroscopy. The results exhibit a tight interaction between adsorbed molecules and UTSA-280 frameworks.

Acknowledgements

First of all, I want to give my deepest gratitude to my advisor, Prof. Yining Huang for providing me the opportunity to be his student at Western University. Since forth year in undergraduate, he has orientated and helped me in my studying and lab work as a mentor. Without his numerous suggestions, none of my project would have been achieved.

Next, I want to say thank you to my whole family. They encouraged me to peruse my study in Canada and gave me great supports. I also want to extend my appreciation to the family of my aunt, who came to London whenever there is a break and let me feel the warmness of the home in Canada.

I want to thank Prof. Johanna M. Blacquiere, Prof. Yang Song and Prof. François Laguné-Labarthe for serving as my committee. I especially appreciate all the advice on my first-year report from Prof. Johanna M. Blacquiere and Prof. Yang Song. I also want to take this chance to thank Prof. Elizabeth Gillies, Prof. Yang Song, Prof. Yining Huang, Dr. Paul Boyle and Prof. Tsun-Kong Sham for their inspiring courses in my graduation study, which really helps my research. I would like to thank Dr. Mathew Willans for his help on NMR experiment. Additionally, I want to thank Dr. Paul Boyle and Aneta Borecki for their assistance on the X-ray data collection. Besides, a special thanks is given to Ms. Darlene McDonald for her great help during my program.

Last but not the least, I would like to thank the past members in our research group: Dr. Shoushun Chen, Dr. Vinicius Martins, Dr. Natália Hadler Marins and Yingxian Li. And it is also an honour to work with current group members: Sandamini Alahakoon, Jiabin Xu, Tahereh Azizivahed, Wanli Zhang, Jingyan Liu and Yan Ham Ng. They not only provided valuable suggestions on my project but also made it a joyful time working in the lab.

Table of Contents

Abstract.....	ii
Summary of Lay Audience	iii
Acknowledgements.....	iv
Table of Contents.....	v
List of Tables	vii
List of Figures	vii
List of Abbreviation.....	xv
Chapter 1.....	1
1. General introduction.....	1
1.1 Composition and properties of MOFs.....	1
1.2 S-block metals in MOFs	3
1.3 Organic ligands in MOFs.....	12
1.4 Organic ligands studied in this thesis.....	18
1.5 Introduction of solid-state nuclear magnetic resonance (SSNMR)	18
1.6 NMR interactions.....	20
1.7 Techniques of SSNMR	27
1.8 SSNMR spectrum simulations.....	31
1.9 Outline of the thesis	33
1.10 Reference	34
Chapter 2.....	44
2. Investigating the coordination environments using MAS SSNMR.....	44
2.1 Introduction.....	44
2.2 Experimental	51
2.3 Results and discussion	54
2.4 Conclusion	76
2.5 Reference	77
Chapter 3.....	79

3.	Exploring the dynamics and adsorption of $^{13}\text{CO}_2$ in four porous SDB MOFs using VT ^{13}C static SSNMR	79
3.1	Introduction.....	79
3.2	Experimental	81
3.3	Results and discussion	82
3.4	Conclusion	99
3.5	Reference	100
	Chapter 4.....	102
4.	Investigating the dynamics and adsorption of small molecules in MOFs with squarate linker (C_4O_4)	102
4.1	Introduction.....	102
4.2	Experimental	105
4.3	Results and discussion	108
4.4	Conclusion	123
4.5	Reference	123
	Chapter 5.....	126
5.	Overall conclusions	126
5.1	Summary and critical analysis	126
5.2	Future work.....	126
	Curriculum Vitae	128

List of Tables

Table 1-1 Most usual coordination numbers for each s-block metals within MOFs.	12
Table 1-2 The prediction of spin quantum number I according to the number of protons and neutron.....	19
Table 1-3 Estimated magnitudes of typical NMR nuclear spin interactions.	20
Table 2-1 The experimental parameters setup of ^{13}C , ^7Li , ^{23}Na , ^{25}Mg and ^{133}Cs SSNMR.	53
Table 2-2 The number of inequivalent C1 and C5 atoms in each MOF (based on each crystal structure) and the number of C1 and C5 that can be observed from the ^{13}C NMR spectra.	60
Table 2-3 The chemical values of each resonance at C1 and C5 site in all ^{13}C NMR spectra. (The chemical shift value for shoulder are shown in bracket).....	60
Table 2-4 The integral ratio of each resonance at C1 and C5 site in all ^{13}C NMR spectra.	61
Table 2-5 Simulated ^{23}Na MAS NMR parameters for as-made and activated Na_2SDB	74
Table 2-6 Simulated ^{25}Mg MAS NMR parameters for as-made MgSDB	75
Table 3-1 The static ^{13}C SSNMR parameters of adsorbed $^{13}\text{CO}_2$ associated resonance and the CO_2 motional data of adsorbed $^{13}\text{CO}_2$ in Na_2SDB at various temperature. All motion rates are $\geq 10^7$ Hz.....	85
Table 3-2 The static ^{13}C SSNMR parameters of adsorbed $^{13}\text{CO}_2$ associated resonance and the CO_2 motional data of adsorbed $^{13}\text{CO}_2$ in MgSDB at various temperature. All motion rates are $\geq 10^7$ Hz.....	88
Table 3-3 The static ^{13}C SSNMR parameters of adsorbed $^{13}\text{CO}_2$ associated resonances in CaSDB and SrSDB at various temperature.	93
Table 3-4 The CO_2 motional data of adsorbed $^{13}\text{CO}_2$ in CaSDB and SrSDB at various temperature. All motion rates are $\geq 10^7$ Hz.....	94
Table 4-1 The ^2H SSNMR parameters of D_2O exchanged UTSA-280 and $\text{Zn}(\text{bipy})\text{C}_4\text{O}_4(\text{H}_2\text{O})_2$	114
Table 4-2 The ^2H SSNMR parameters and motional data of adsorbed C_2D_2 in UTSA-280	

at various temperature. (All motion rates are $\geq 10^7$ Hz)	116
Table 4-3 The ^{13}C chemical shift parameters of adsorbed $^{13}\text{CO}_2$ in UTSA-280 at various temperature.	120
Table 4-4 The CO_2 motional data of adsorbed $^{13}\text{CO}_2$ in UTSA-280 at various temperature. All motion rates are $\geq 10^7$ Hz.	121

List of Figures

Figure 1-1 Schematic diagram of basic composition of metal-organic frameworks. ¹	1
Figure 1-2 Changing in porosity with different types of organic linkers in the IRMOF-n series. ¹⁴ (the size of channels are labeled in yellow).....	2
Figure 1-3 (a). 1D windmill-like structure along c direction, Z-shaped 2D layer structure and 3D hinged network of Li ₄ (pdda)(OC-NMe ₂). (b). The connection mode of NTB ³⁻ ligand in {(Me ₂ NH ₂) ₂ [Li(NTB)](H ₂ O) ₃ (DMF) ₂ } _n . (Li sites are labeled with pink tetrahedrons) ^{21,22}	4
Figure 1-4 (a). Silicon-centered linkers L1-H ₂ , L2-H ₃ and L3-H ₄ . (b). The coordination environment around each Na ⁺ cation in IMP-23. (c). The coordination environment around each Na ⁺ cation in IMP-25 and IMP-26. (d). The repeat unit in the metal node of IMP-27. ²³	5
Figure 1-5 (a). The coordination environment around potassium ion of [C ₇ H ₃ KNO ₄] _n . (b). 1D and 2D structure of [C ₇ H ₃ KNO ₄] _n . ²⁴	6
Figure 1-6 (a). Crystal packing of CD-MOF-3. (b),(c). Side-on view and top view of the arrangement of Cs ⁺ ions around two γ -CD units. (d). Local coordination environment of Cs ⁺ center. ²⁶	7
Figure 1-7 (a). Up down view of BCF-3. ²⁸ (b). Side view of BCF-4. ²⁹	8
Figure 1-8 Organic linkers (H ₄ TDA(left) and H ₄ ODA(right)) and the structure of MOFs formed by Mg ²⁺ and two linkers respectively. ³¹	9
Figure 1-9 (a). The organic linker 3,5-PDC and 2,4-PDC. (b). The view of Mg(3,5-PDC)(H ₂ O) along c-axis. (c). The asymmetric unit of Mg(2,4-PDC)(H ₂ O) ₃ . ³⁰	9
Figure 1-10 Local coordination environment of Ca ²⁺ ion and structure of (a). Ca(BDC)(DMF)(H ₂ O); (b). Ca(H ₂ dhtp)(DMF); (c). Ca(H ₂ dhtp)(DMF) ₂ . ³²	10
Figure 1-11 (a). Local coordination environment of Sr ²⁺ ions within {Sr _{1.5} (ptc)·5H ₂ O} _n . (b). Local coordination environment of Ba ²⁺ ions within {[Ba(ptc)(H ₂ O)][Ba(ptcH ₂)H ₂ O]} _n . ³³	11
Figure 1-12 Three mono-carboxylate ligands and resulted 2D structures. ⁴⁴	13
Figure 1-13 The organic linkers used to construct ZJNU-46, ZJNU-47 and ZJNU-48. ⁴⁵	

.....	14
Figure 1-14 (a). The organic linkers used to construct ZJNU-91 and ZJNU-92. (b),(c). The structure of ZJNU-91 and ZJNU-92. ⁴⁷	15
Figure 1-15 (a). The organic linkers used in Ni-MOFs and the helical chains. (b).The organic linkers used in Mn-MOF and the structure of Mn-MOF (c). The 2D network and 3D structure in Zn-MOF. (d). The organic linkers used in Zn-MOF and Cd-MOF. (e). 3D structure of Cd-MOF.....	17
Figure 1-16 2D and 3D structure of H ₂ SDB (a) and H ₂ C ₄ O ₄ (b).....	18
Figure 1-17 Illustration of Zeeman interaction within nucleus with $I=1/2$	21
Figure 1-18 A typical powder spectrum with labelled three chemical shift components. ⁷³	22
.....	22
Figure 1-19 The influence of δ_{iso} (a), Ω (b), and κ (c) on a static NMR spectrum. ⁷⁸	23
Figure 1-20 PAS of CO ₂ molecule ⁷⁶ and the ¹³ C SSNMR spectrum of rigid CO ₂ molecule where $\delta_{iso}=125$ ppm, $\Omega=335$ ppm and $\kappa=1$. ⁷⁷	24
Figure 1-21 (a). The demonstration of the principle of dipolar interaction. (b). Pake doublet and patterns (dotted lines) which refers to the dipole perturbation of nuclei S either enhance or cancel the magnetic field that I experiences. ⁸⁰	25
Figure 1-22 (a). the energy level and transition with Zeeman interaction, first-order and second-order quadrupolar interaction. ($I=3/2$ as example; $\omega_Q = 3C_Q/4I(2I-1)$, called quadrupolar splitting parameter) (b). The typical spectrum with only first-order quadrupolar interaction. (c). The CT peak affected by the second order quadrupolar interaction. ⁸⁴	27
Figure 1-23 The scheme of one pulse sequence. ⁷²	28
Figure 1-24 The scheme of echo sequence. ⁸⁵	29
Figure 1-25 Pulse sequence of CP (Cross polarization) ⁷⁹	30
Figure 1-26 Schematic diagram of Magic-angle spinning. ⁷⁹	30
Figure 1-27 Two-pulse sequence and the example of 3Q-MAS in a spin $I=5/2$ system. ⁸⁹	31
.....	31
Figure 1-28 ¹³ C SSNMR simulation spectra of CO ₂ with changing wobbling and hopping	

angles in fast motion regime with a motional rate of $1 \times 10^7 \text{ s}^{-1}$	32
Figure 1-29 ^2H SSNMR simulation spectra of C_6D_6 (left) and CD_4 (right) with changing motion rates under different motion types.	33
Figure 2-1 (I). 3D framework of Li_2SDB . (II). The local coordination geometries of the central Li(1) and Li(2) atoms. (All H atoms are omitted for clarity).....	44
Figure 2-2 (I). 3D framework of Na_2SDB . (II). The local coordination geometries of the central Na(1) and Na(2) atoms. (All H atoms are omitted for clarity)	45
Figure 2-3 (I). 3D framework of Cs_2SDB . (II). The local coordination geometries of the central Cs(1) and Cs(2) atoms. (All H atoms are omitted for clarity)	46
Figure 2-4 (I). 3D framework of $\text{Mg}_3(\text{OH})_2(\text{SDB})_2(\text{EtOH})(\text{H}_2\text{O})_3$. (II). The local coordination geometries of the central Mg(1), Mg(2) and Mg(3) atoms. (All H atoms are omitted for clarity)	48
Figure 2-5 (I). 3D framework of $\text{Mg}_3(\text{OH})_2(\text{SDB})_2$. (II). The local coordination geometries of the central Mg(1) and Mg(2) atoms. (All H atoms are omitted for clarity)	49
Figure 2-6 (I). 3D framework of MSDB (M=Ca or Sr). (II). The local coordination geometries of the central M (M=Ca or Sr) atom. (All H atoms are omitted for clarity)	50
Figure 2-7 Powder x-ray diffraction patterns for MOFs.....	54
Figure 2-8 Powder x-ray diffraction patterns for MgSDB with elevating temperature. ³	55
Figure 2-9 Powder x-ray diffraction patterns for Cs_2SDB with solvent exchange in ethanol and acetone.....	56
Figure 2-10 TGA curves for MOFs.	56
Figure 2-11 The overview of ^{13}C CPMAS NMR spectra for pure H_2SDB (organic linker) and six SDB MOFs based on s-block metals. (* corresponds to spinning side bands)	59
Figure 2-12 ^{13}C CP MAS NMR spectrum of dried Li_2SDB . (* corresponds to spinning side bands) (Experimental patterns are in blue and resolved peaks are labeled in yellow)	62
Figure 2-13 ^{13}C CP MAS NMR spectra of as-made and activated Na_2SDB . (* corresponds	

to spinning side bands) (Experimental patterns are in blue or red, and resolved peaks are labeled in yellow).....	63
Figure 2-14 ^{13}C CP MAS NMR spectra of dried Cs_2SDB . (* corresponds to spinning side bands).....	65
Figure 2-15 ^{13}C CP MAS NMR spectra of as-made and activated MgSDB . (* corresponds to spinning side bands) (Experimental patterns are in blue or red, and resolved peaks are labeled in yellow).....	67
Figure 2-16 ^{13}C CP MAS NMR spectra of as-made and activated CaSDB . (* corresponds to spinning side bands) (Experimental patterns are in blue or red, and resolved peaks are labeled in yellow).....	68
Figure 2-17 ^{13}C CP MAS NMR spectra of as-made and activated SrSDB . (* corresponds to spinning side bands) (Experimental patterns are in blue and resolved peaks are labeled in yellow).....	70
Figure 2-18 ^7Li MAS and static NMR spectra of Li_2SDB (* indicates spinning sidebands)	71
Figure 2-19 ^{23}Na 2D 3Q MAS NMR spectra of as-made and activated Na_2SDB	72
Figure 2-20 Experimental ^{23}Na MAS NMR spectra of as-made and activated Na_2SDB	72
Figure 2-21 Simulated ^{23}Na MAS NMR spectra of as-made and activated Na_2SDB	74
Figure 2-22 ^{133}Cs MAS NMR spectra of dried Cs_2SDB with spinning rate 5 kHz and 20 kHz (top) (* indicates spinning sidebands) and ^{25}Mg MAS NMR spectrum of as-made MgSDB	76
Figure 3-1 Global atmospheric CO_2 level. ⁶	80
Figure 3-2 The scheme of CO_2 capture in Aqueous alkanolamine solutions.	81
Figure 3-3 (a). The experimental (blue) and simulated (red) static ^{13}C VT SSNMR spectra of Na_2SDB loaded with 0.2 mole $^{13}\text{CO}_2$ per mole of Na. (b). The specific patterns for free (orange) and adsorbed (green) $^{13}\text{CO}_2$. (c). Comparison of experimental and stacked simulated patterns.....	83
Figure 3-4 (a). Analytical simulated and motional simulated static ^{13}C SSNMR spectra of $^{13}\text{CO}_2$ loaded Na_2SDB , including both threefold wobbling angles (α) and twofold	

hopping angles (β) at different temperature. (b). The model of CO ₂ dynamics in Na ₂ SDB with both wobbling and hopping.....	86
Figure 3-5 (a). The experimental (blue) and simulated (red) static ¹³ C VT SSNMR spectra of MgSDB loaded with 0.2 mole ¹³ CO ₂ per mole of Mg. (b). The specific patterns for free (orange) and adsorbed (green) ¹³ CO ₂ . (c). Comparison of experimental and stacked simulated patterns.....	87
Figure 3-6 Analytical simulated and motional simulated static ¹³ C SSNMR spectra of ¹³ CO ₂ loaded MgSDB, including both threefold wobbling angles (α) and twofold hopping angles (β) at different temperature.....	89
Figure 3-7 (a). The experimental (blue) and simulated (red) static ¹³ C VT SSNMR spectra of CaSDB loaded with 0.2 mole ¹³ CO ₂ per mole of Ca. (b). The specific patterns for free (orange) and adsorbed (green and purple) ¹³ CO ₂ at different sites. (c). Comparison of experimental and stacked simulated patterns.....	91
Figure 3-8 (a). The experimental (blue) and simulated (red) static ¹³ C VT SSNMR spectra of SrSDB loaded with 0.2 mole ¹³ CO ₂ per mole of Sr. (b). The specific patterns for free (orange) and adsorbed (green and purple) ¹³ CO ₂ at different sites. (c). Comparison of experimental and stacked simulated patterns.....	92
Figure 3-9 Analytical simulated and motional simulated static ¹³ C SSNMR spectra of ¹³ CO ₂ loaded SrSDB, including both threefold wobbling angles (α) and twofold hopping angles (β) at different temperature.....	97
Figure 3-10 Analytical simulated and motional simulated static ¹³ C SSNMR spectra of ¹³ CO ₂ loaded CaSDB, including both threefold wobbling angles (α) and twofold hopping angles (β) at different temperature.....	97
Figure 3-11 The model of CO ₂ C2 hopping within MgSDB as an example (left) and the location of π -pocket (right). (CO ₂ molecules are zoomed out for the clearer view of four sites)	99
Figure 4-1 (I). 3D framework of UTSA-280, (II). the local coordination geometries of the central Ca atoms, (III). the local coordination geometries of C ₄ O ₄ linker (all H atoms are omitted for clarity)	104

Figure 4-2 (I). 3D framework of $Zn(bipy)(C_4O_4)(H_2O)_2$, (II). the local coordination geometries of the central Zn atom. (In model, all terminal O atoms and N atoms are connected to Zn atoms, and all H atoms are omitted for clarity).....	105
Figure 4-3 PXRD patterns for UTSA-280 and $Zn(bipy)C_4O_4(H_2O)_2$	108
Figure 4-4 TGA curves for UTSA-280 and $Zn(bipy)C_4O_4(H_2O)_2$	110
Figure 4-5 CO_2 sorption isotherm of UTSA-280 at 273K.	111
Figure 4-6 Experimental (top) and simulated (middle) static 2H SSNMR spectra of D_2O exchanged UTSA-280 before and after activation with stacked resonances of each site (bottom).	112
Figure 4-7 Experimental (top) and simulated (middle) static 2H SSNMR spectra of D_2O exchanged $Zn(bipy)C_4O_4(H_2O)_2$ before activation. (Left: the 2H SSNMR experiment was performed after the sample was exposed to air for several days. Right: the 2H SSNMR experiment was immediately performed after the sample was dried).....	114
Figure 4-8 Experimental (blue) and simulated (red) static 2H VT SSNMR spectra of C_2D_2 loaded UTSA-280. (0.1 mole C_2D_2 was loaded per mole of Ca)	115
Figure 4-9 (a). Analytical simulated and motional simulated static 2H SSNMR spectra of C_2D_2 loaded UTSA-280, including both threefold wobbling angles (α) and fourfold hopping angles (β) at different temperatures. (b). The model of C_2D_2 C4 hopping within UTSA-280. (C_2D_2 molecules are zoomed out for the clearer view of four sites)	117
Figure 4-10 (a). The experimental (blue) and simulated (red) static ^{13}C VT SSNMR spectra of UTSA-280 loaded with $^{13}CO_2$. (b). The specific patterns for free (orange) and adsorbed (green and purple) $^{13}CO_2$ at two different sites. (c). comparison of experimental and stacked simulated spectra of $^{13}CO_2$	119
Figure 4-11 Analytical simulated and motional simulated static ^{13}C SSNMR spectra of $^{13}CO_2$ loaded UTSA-280, including both threefold wobbling angles (α) and twofold hopping angles (β) at different temperatures.	122
Figure 4-12 The model of CO_2 C4 hopping within UTSA-280. (CO_2 molecules are zoomed out for the clearer view of four sites)	122

List of Abbreviation

1D	One dimension
2,4-PDC	2,4-Pyridinedicarboxylate
2D	Two dimensions
3,5-PDC	3,5-Pyridinedicarboxylate
BDC	1, 4-Benzenedicarboxylate
BET	Brunauer–Emmett–Teller
bipy	Bipyridine
BPDC	4,4'-Biphenyldicarboxylic acid
btb	1,3,5-Benzenetricarboxylic acid
CCS	Carbon capture and storage
CP	Cross polarization
CSA	Chemical shielding anisotropy
CT	Central transition
DMF	Dimethylformamide
DTPD	5,5'-(2,6-Dimethoxynaphthalene-1,5-diyl)diisophthalic acid
EB	4-Ethylbenzoic acid
EFG	Electric field gradient
EXAFS	Extended X-ray Absorption Fine Structure
FID	Free induction decay
FT	Fourier transformation
FTIR	Fourier-transform infrared spectroscopy
HB	4-Heptylbenzoic acid
MAS	Magic-angle spinning
MEA	Monoethanolamide
MOFs	Metal organic frameworks

MQMAS	Multiple-quantum magic-angle spinning
NMS	Nuclear magnetic shielding interaction
NOAA	National Oceanic and Atmospheric Administration
NTB	4,4',4''-nitrilotrisbenzoate
OPIBs	Organic potassium-ion batteries
PAS	Principal axis system
pdta	5,5'-(Propane-1,3- diylbis(oxy)) diisophthalic acid
ptc	Pyridine-2,4,6-tricarboxylic acid
PXRD	Powder x-ray diffraction
pyz	Pyrazine
pzdc	Pyrazine-2,3-dicarboxylate
rf	Radio frequency
SCXRD	Single crystal x-ray diffraction
SDB	4, 4'- Sulfonyldibenzoate
SSNMR	Solid-state nuclear magnetic resonance
ST	Satellite transitions
TEA	Triethanolamine
TGA	Thermogravimetric Analysis
TMS	Tetramethylsilane
UL	Ultralight
VT	Various temperature
XANES	X-ray Absorption Near Edge Structure

Chapter 1

1. General introduction

1.1 Composition and properties of MOFs

Metal-organic frameworks (MOFs) are microporous materials composed of metal ions or clusters linked by organic ligands to form potentially infinite structures. Since the first MOF, MOF-5, was found in 1999 by Yaghi,¹ MOFs have attracted attention in the past decades. Compared with other microporous materials such as zeolites, MOFs are more diverse since they can be rationally constructed with various metal centers and designable functional organic linkers.¹ Because of their porous structure and properties, MOFs are considered to have a broad range of promising applications.^{2,3,4,5} in gas capture and storage (including CO₂ capture and storage), gas separation,^{6,7} batteries,^{8,9} catalysis,¹⁰ ion exchange¹¹ and drug delivery,¹²

Generally, there are two categories of traditional synthesis methods, solvothermal and non-solvothermal. Solvothermal synthesis implies the use of solvent in the synthesis, while the term “hydrothermal” specifically indicates the use of water as solvent. The solvothermal synthesis is carried out at or above the boiling point of the solvent in closed chemical reactors at an elevated pressure which usually results from the vapour of the solvent. Non-solvothermal methods conversely refer to the synthesis that occurs below the boiling point of the solvent in an open container, such as electrochemical synthesis and mechanochemical synthesis. Due to the high pressure caused by solvent vapour in solvothermal synthesis, it helps to raise the solubility of salts, which in turn promotes reaction.¹³

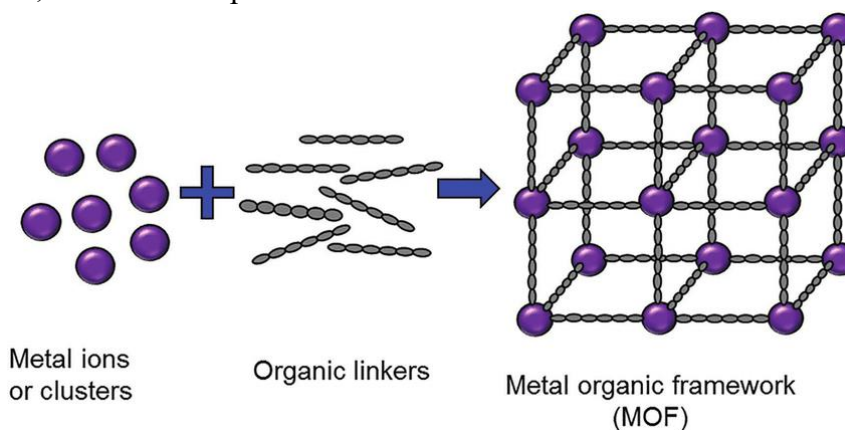


Figure 1-1 Schematic diagram of basic composition of metal-organic frameworks.¹

Metal ions or clusters and organic linkers, as two main components of MOFs, determine the properties of MOFs, such as exceptional porosity, large surface area, high thermal stabilities and variability. Depending on the length of organic linkers, high porosity MOFs usually come with longer linkers while shorter linkers result in low porosity.¹⁴ As shown in **Figure 1-2**, MOFs (IRMOF-n series) exhibit rising porosity when incorporating organic linkers with increasing length. The surface areas of MOFs are usually over hundreds m^2/g . Additionally, given the reason that C-O, C-C bonds within organic linkers and O-M bonds between metal ions and linkers are all strong bonds, MOFs are featured with high thermal stability. Last but not the least, variability, as one of the outstanding features of MOFs, is achieved by varying the internal and external factors. For instance, as the internal factors which is mostly about metal centers and organic ligands, substituting with different metal cations, the framework may vary since different metal cations have various charges and coordination numbers. Replacing the organic linkers will result in various properties of the porous channels in MOFs, such as pore shape and pore size. It is worth mentioning by introducing functional groups into organic linkers (-OH, -Cl, -Br and -NH₂), the properties of the linker are changed, such as the hydrophilicity. The different functional groups will further modify the pore size and the interactions between frameworks and guest molecules, making MOFs good material for gas selectivity and separation.^{15,16,17} Furthermore, as the external factors, the types of solvent and synthesis conditions, like synthesis temperature and time, will affect MOF formation as well.¹⁸

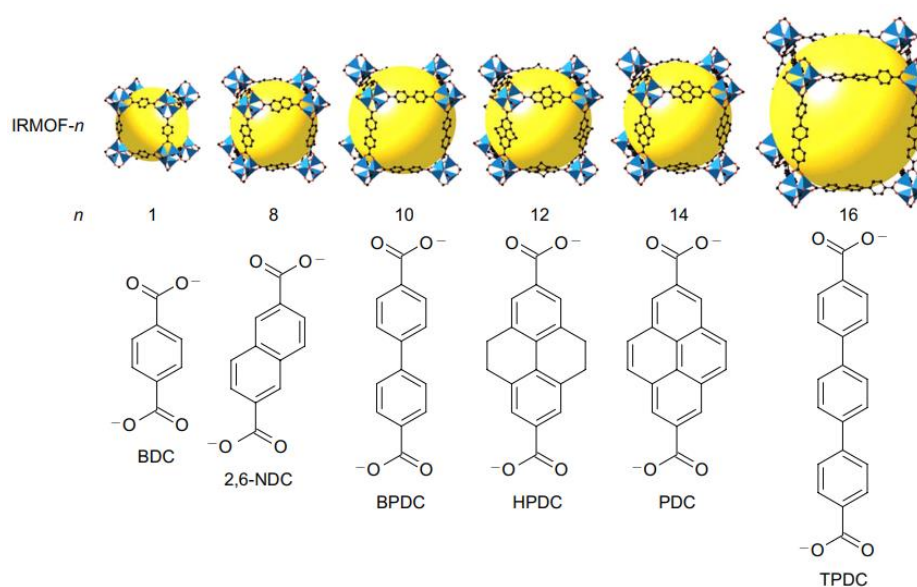


Figure 1-2 Changing in porosity with different types of organic linkers in the IRMOF-n series.¹⁴ (the size of channels are labeled in yellow)

1.2 S-block metals in MOFs

For the metal center, giving the well-known coordination behavior and stable framework formed with bridging-carboxylic acid linkers under hydro and solvothermal conditions, transition metals and rare earth metals are always considered as good candidates. For example, a report by Zhu and coworkers mentioned that zinc can adopt 4 coordination modes: tetrahedral for four-coordinated zinc, trigonal bipyramidal and square pyramidal for five-coordinated zinc, and octahedral for six-coordinated zinc.¹³ Distinguished from transition metals, s-block metals usually tend to exist in the ionic states and tend to coordinate with solvent molecules, forming the solvated metal centers. Additionally, the various possible coordination numbers resulted in a complicated situation for people to systematically study s-block metal MOFs.^{19,20}

1.2.1 Li-MOFs

Among s-block metals, lithium is the lightest element and an excellent reducing agent that easily loses electrons like all other alkali metals. Li ion normally crystallizes in the tetrahedral geometry due to the small size of the atom. With various organic ligands employed, a huge number of Li-MOFs were synthesized, where some Li-MOFs' structures showed great flexibility. A novel 3D coordination polymer $\text{Li}_4(\text{pdta})(\text{OC-NMe}_2)$ (pdta = 5,5'-(propane-1,3-diylbis(oxy)) diisophthalic acid) (**Figure 1-3a**) has been reported by Liu²¹ which exhibits large expansion upon heating, also named positive thermal expansion (PTE). Two crystallographically independent Li(I) atoms (Li[1] and Li[2]) both present a LiO_4 tetrahedral geometry constructed by four oxygen atoms, which are all from the carboxyl group of pdta ligand, except one for Li [2] atom that binds to the carbonyl group of DMF. With V-shaped pdta linker, a large windmill-like unit is constructed. Another Li-based MOF $\{(\text{Me}_2\text{NH}_2)_2[\text{Li}(\text{NTB})](\text{H}_2\text{O})_3(\text{DMF})_2\}_n$ (NTB = 4,4',4''-nitriлотrisbenzoate) (**Figure 1-3b**), reported by Chen²², is believed to be a potential luminescent probe for the detection of Fe(III) ion and nitrobenzene in solution. It contains one crystallographically independent Li(I) ion within each asymmetric unit. Li(I) ion is four-coordinated by four carboxylate O atoms from

four different NTB^{3-} ligands to furnish a slightly distorted tetrahedral geometry.

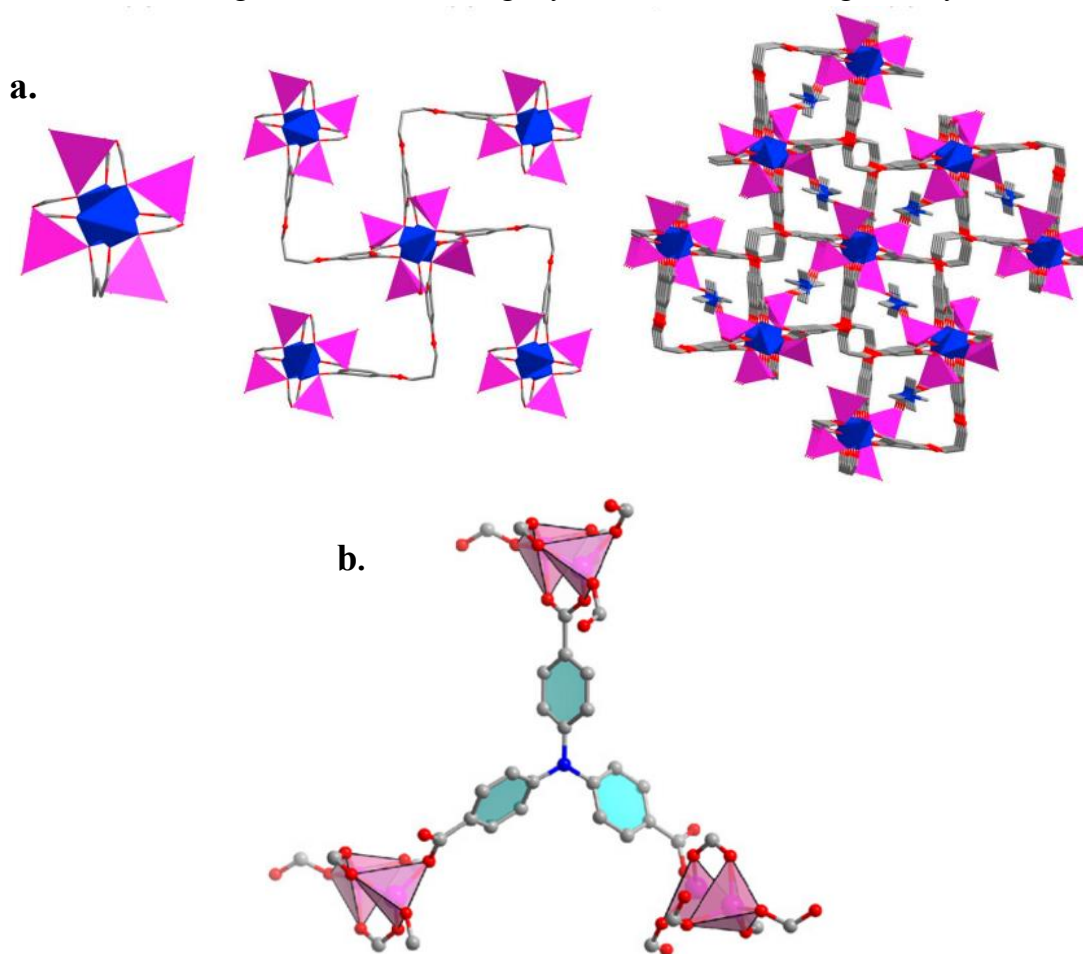


Figure 1-3 (a). 1D windmill-like structure along *c* direction, Z-shaped 2D layer structure and 3D hinged network of $\text{Li}_4(\text{pdta})(\text{OC-NMe}_2)$. (b). The connection mode of NTB^{3-} ligand in $\{(\text{Me}_2\text{NH}_2)_2[\text{Li}(\text{NTB})](\text{H}_2\text{O})_3(\text{DMF})_2\}_n$. (Li sites are labeled with pink tetrahedrons)^{21,22}

1.2.2 Na-MOFs

Same as other s-block metals, sodium normally exists as Na^+ in MOFs. As the atom gets larger than Li, the coordination mode is not limited to 4-coordinated tetrahedral geometry. Even with the same organic ligand, different Na-MOFs have been successfully synthesized with more than one coordination modes. A series of “light metal” based MOFs (from IMP-22 to IMP-27) were synthesized and reported by Pugh,²³ where IMP-23 ($\text{Na}_2(\text{L1})(\text{DMF})_2$), IMP-25 ($\text{Na}_{12}(\text{L2})_4(\text{DMF})_3$), IMP-26 ($\text{Na}_{42}(\text{L2})_{14}(\text{H}_2\text{O})_3$) and IMP-27 ($\text{Na}_4(\text{L3})(\text{DMF})_4(\text{H}_2\text{O})_4$) are Na based MOFs (**Figure 1-4**). In IMP-23, two crystallographically independent Na(I) ions are included in each asymmetric unit. Each Na(I) ion is six-coordinated by four carboxylates

groups, where one of them binds to Na atom in a bidentate chelating mode while the other three are in the monodentate chelating mode, and one DMF molecule. Unlike IMP-23, IMP-25 contains 4 crystallographically independent Na(I) ions. Na(1), Na(2) and Na(4) are all five-coordinated and Na(3) is in a four-coordinated environment since the organic linker L2 (L2= 4,4',4''-(methylsilanetriyl)tribenzoic acid) (**Figure 1-4**) is bulkier than organic linker L1 (L1= 4,4'-(dimethylsilanediy) dibenzoic acid) for IMP-23. Under the same synthesis condition, IMP-26 is formed together with IMP-25 (in a roughly 1:2 ratio for IMP-25: IMP-26), where Na⁺ cation is binding to the H₂O molecule instead of the DMF molecule. With organic linker L3 (4,4',4'',4'''-silanetetrayltetrabenzoic acid), IMP-27 is built up with four crystallographically independent Na(I) ions. Two of them are six-coordinated, while the other two are located in seven-coordinated geometry.

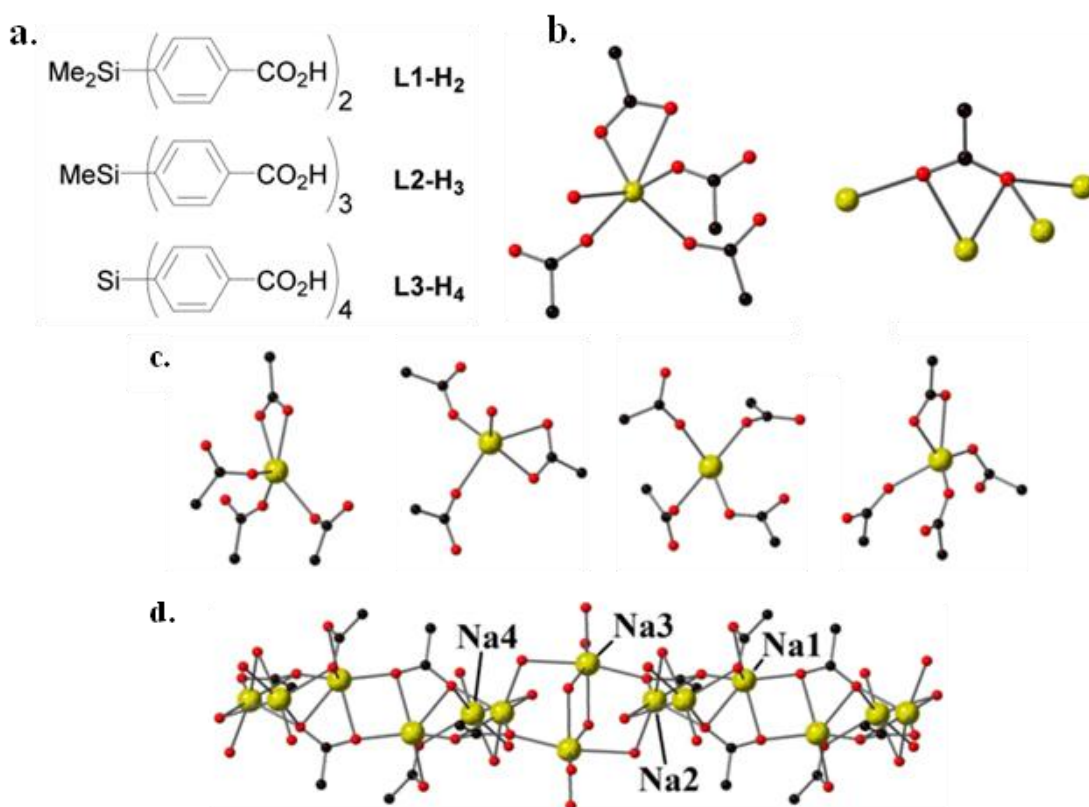


Figure 1-4 (a). Silicon-centered linkers L1-H₂, L2-H₃ and L3-H₄. (b). The coordination environment around each Na⁺ cation in IMP-23. (c). The coordination environment around each Na⁺ cation in IMP-25 and IMP-26. (d). The repeat unit in the metal node of IMP-27.²³

1.2.3 K-MOFs

Due to the fast chemical reaction rate of K^+ cation in batteries and the high abundance of potassium in the earth, organic potassium-ion batteries (OPIBs) have been widely considered as the new generation battery system after Li and Na. Many K-MOFs have been synthesized in past years for OPIBs, and there are also several K-MOFs constructed based on its intense photoluminescence properties. A novel K-MOF, $[C_7H_3KNO_4]_n$ (**Figure 1-5**), was mentioned and synthesized by Li.²⁴ Each asymmetric unit contains one crystallographically independent K(I) ion, which is seven-coordinated with two O atoms and one N atom from one organic ligand, and four O atoms from four other linkers. 1D zigzag chain is generated by the connection of O atoms and K atoms in up and down modes. Then 2D layered structures could be formed by the linkage of K^+ cations and $C_7H_3NO_4^-$ anions from the 1D chains, further generating 3D architectures. This MOF showed excellent rate capacities and superior long-cycle capacities, which proved the potential of K-MOFs as efficient electrode materials for OPIBs. Another K-MOF, $[K_8(ptca)_3(H_3O)_4]_n$,²⁵ with the linker 3,4,9,10-perylenetetracarboxylic acid (H_4ptca) contains two crystallographically independent K(I) ions in each asymmetric unit. K(1) has K_1O_8 coordination environment while K(2) is in an octahedral geometry. As Seco proved, this material displays intense photoluminescence properties in liquid and solid states at room temperature, and the potential of this compound to build humidity actuators on flexible substrates.

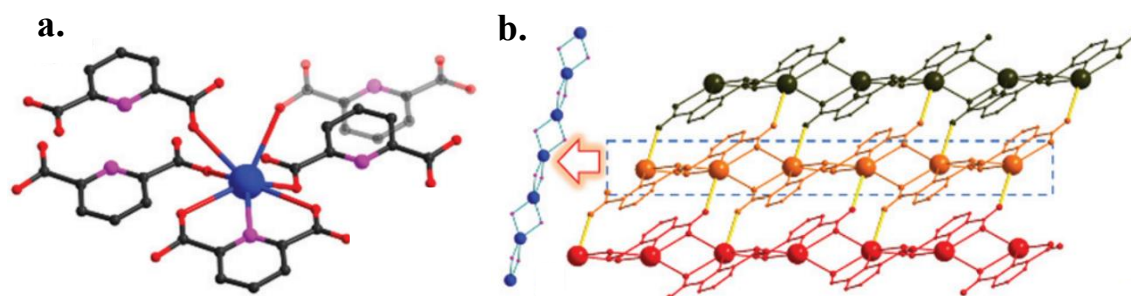


Figure 1-5 (a). The coordination environment around potassium ion of $[C_7H_3KNO_4]_n$. (b). 1D and 2D structure of $[C_7H_3KNO_4]_n$.²⁴

1.2.4 Rb-MOFs and Cs-MOFs

Eight-coordinated modes are always found in Rb and Cs MOFs due to their large ionic radius. Additionally, because of the similar properties, Rb and Cs often share the same coordination mode. Nanoporous MOFs, CD-MOF-2 and CD-MOF-3, are constructed by the γ -cyclodextrins (γ -CDs) with either Rb^+ centers or Cs^+ centers. It is proved by Forgan²⁶ that CD-MOF-2 shows potential as a simple, inexpensive and green porous material; topologically distinct MOFs could be synthesized using CD linker with different s-block metals. Only one crystallographically independent Rb(I) or Cs(I) ion is included in each asymmetric unit, where each metal ion center is eight-coordinated with 8 O atoms from 4 different γ -cyclodextrin.

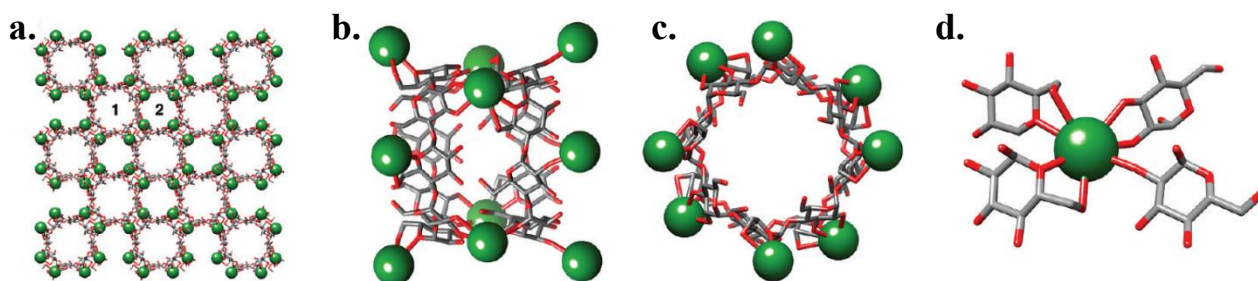


Figure 1-6 (a). Crystal packing of CD-MOF-3. (b).(c). Side-on view and top view of the arrangement of Cs^+ ions around two γ -CD units. (d). Local coordination environment of Cs^+ center.²⁶

1.2.5 Be-MOFs

Beryllium is the first member of alkali earth metals. Be only forms tetrahedrally coordinated units because of its small size and the fact that its bonds are always covalent due to the high charge/radius ratio.¹⁹ There were only a few Be-MOFs have been studied, due to the fact that Be is toxic even though it is the lightest alkaline earth metal.²⁷ The first single-crystal structure of a beryllium-based MOF was reported by Long²⁸ using 1,3,5-benzenetricarboxylic acid (btb) as the linker. $[\text{Be}_{12}(\text{OH})_{12}]^{12+}$ rings are formed by the combination of tetrahedrally coordinated Be. Further linked by the btb, $\text{Be}_{12}(\text{OH})_{12}(\text{btb})_4$ is constructed. Two other Be-MOFs, $\text{Be}_2(\text{OH})_2(\text{BDC})$ (BCF-3) (**Figure 1-7a**) and $\text{Be}_4(\text{OH})_4(\text{btcc})$ (BCF-4) (**Figure 1-7b**), were synthesized and reported by Kang²⁹. Each Be atom has a tetrahedrally coordinated

geometry in BCF-3 and BCF-4 with two oxygen atoms from hydroxyl groups and two oxygen atoms from either BDC or ttec ligands. BCF-3 shows high thermal stability up to 400 °C and BCF-4 exhibits a moderate CO₂ uptake capacity.

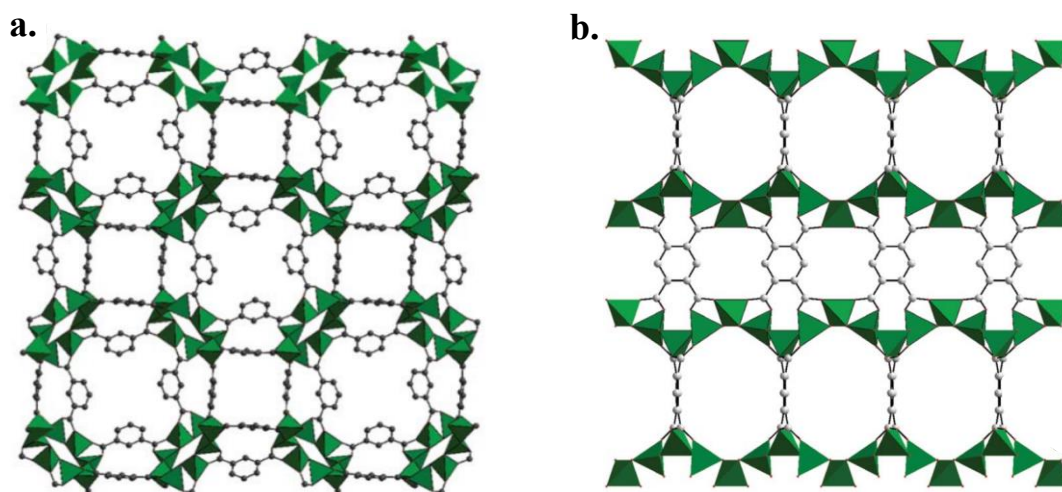


Figure 1-7 (a). Up down view of BCF-3.²⁸ (b). Side view of BCF-4.²⁹

1.2.6 Mg-MOFs

Mg is the most widely used alkali earth metal in MOFs. As similar chemical properties between Mg²⁺ and Zn²⁺, like Zn, Mg is usually in tetrahedral or octahedral coordination mode in the formation of MOFs. Several novel Mg-MOFs with large porous channels have been constructed and reported. Mg(3,5-PDC)(H₂O) and Mg(2,4-PDC)(H₂O)₃ (3,5-PDC = 3,5-pyridinedicarboxylate; 2,4-PDC = 2,4-pyridinedicarboxylate) (**Figure 1-8**) were synthesized and reported by Mallick³⁰. With the position of nitrogen within the organic linkers differing, the two MOFs show totally different structures. Mg(3,5-PDC)(H₂O) contains one crystallographically independent Mg²⁺ ion in each asymmetric unit, given an octahedral coordination environment by one nitrogen atom from the pyridine-N functionality and five oxygen atoms from four carboxylate groups of 3,5-PDC ligands and one coordinated water molecule. 1D channels with open Mg-metal sites are formed along the c-axis. While Mg(2,4-PDC)(H₂O)₃ is also six-coordinated, with two oxygen atoms and one nitrogen atom from two 2,4-PDC linkers and three oxygen atoms from coordinated water to achieve octahedral geometry. Lee³¹ reported two Mg-MOFs with two similar organic linkers, H₄TDA(4,4'-[1,4-

phenylenebis-(carbonylimino)]bis(2-hydroxybenzoic acid)] and H₄ODA(4,4'-[oxalylbis(imino)]bis(2-hydroxybenzoic acid)] (**Figure 1-9**). In both MOFs, Mg²⁺ ions are six-coordinated with 3 oxygen atoms from hydroxyl groups and 3 oxygen atoms from carboxylate groups, forming an infinite framework with one-dimensional, hexagonal channels.

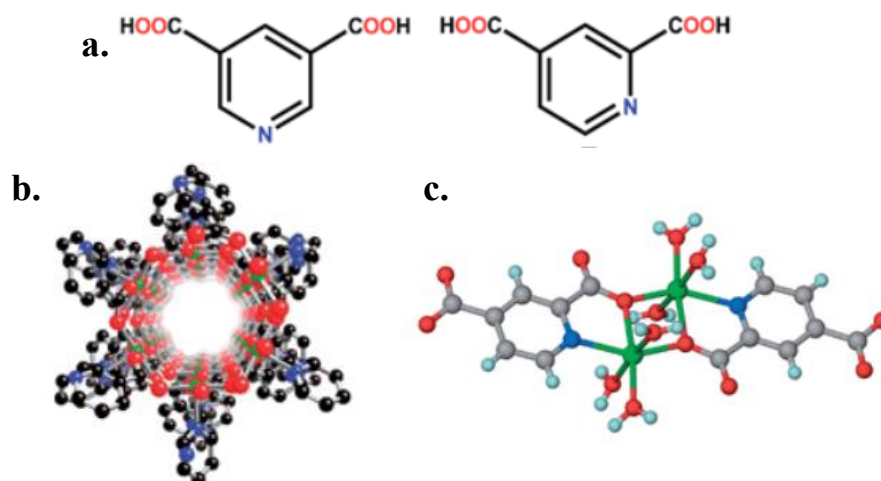


Figure 1-9 (a). The organic linker 3,5-PDC and 2,4-PDC. (b). The view of Mg(3,5-PDC)(H₂O) along c-axis. (c). The asymmetric unit of Mg(2,4-PDC)(H₂O)₃.³⁰

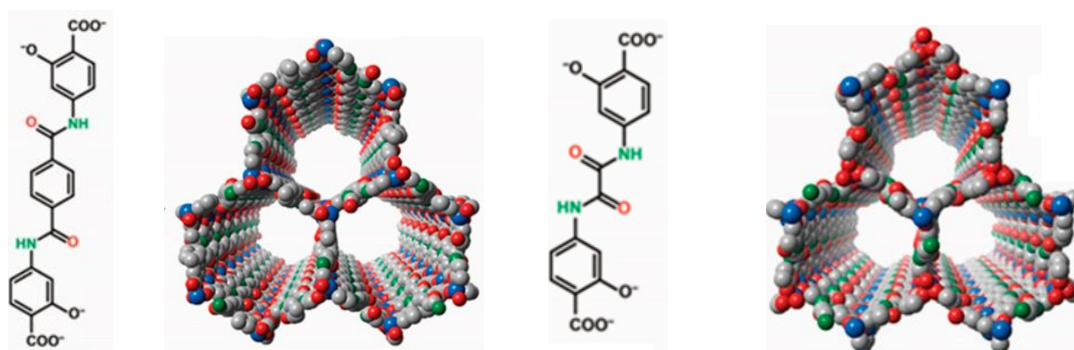


Figure 1-8 Organic linkers (H₄TDA(left) and H₄ODA(right)) and the structure of MOFs formed by Mg²⁺ and two linkers respectively.³¹

1.2.7 Ca-MOFs

Ca tends to have a higher coordination number (from 6 to 8) than Mg because of the larger ionic radius. Ca-MOFs play an important role in biological field due to its biocompatibility. However, solvent molecules are always coordinated to the Ca centers and the removal of them could lead to structural rearrangements in some cases. Liang³² reported several new Ca-MOFs

with aromatic polycarboxylates synthesized under solvothermal conditions (**Figure 1-10**). $\text{Ca}(\text{BDC})(\text{DMF})(\text{H}_2\text{O})$ includes one crystallographically independent Ca^{2+} ion in each asymmetric unit, which is eight-coordinated with six oxygen atoms from the carboxylate groups belonging to four BDC ligands, one oxygen atom from the coordinated water molecule, and one oxygen atom from DMF. 3D structure with rhomboidal channels is generated by the connection of BDC ligands. Ca^{2+} ion is seven-coordinated in $\text{Ca}(\text{H}_2\text{dhtp})(\text{DMF})$ (H_2dhtp = 2,5-dihydroxy-terephthalic acid) with five oxygen atoms of the carboxylate groups from five H_2dhtp ligands, one oxygen atom of the hydroxyl groups of H_2dhtp , and one oxygen atom of coordinated DMF molecule. $\text{Ca}(\text{H}_2\text{dhtp})(\text{DMF})_2$ could be obtained under the same synthesis condition as $\text{Ca}(\text{H}_2\text{dhtp})(\text{DMF})$ except at a lower temperature. Ca^{2+} is six-coordinated with four oxygen atoms of the carboxylate groups from four H_2dhtp ligands and two oxygen atoms from the coordinated DMF molecules. Both $\text{Ca}(\text{H}_2\text{dhtp})(\text{DMF})$ and $\text{Ca}(\text{H}_2\text{dhtp})(\text{DMF})_2$ are porous MOFs with square-grid channels.

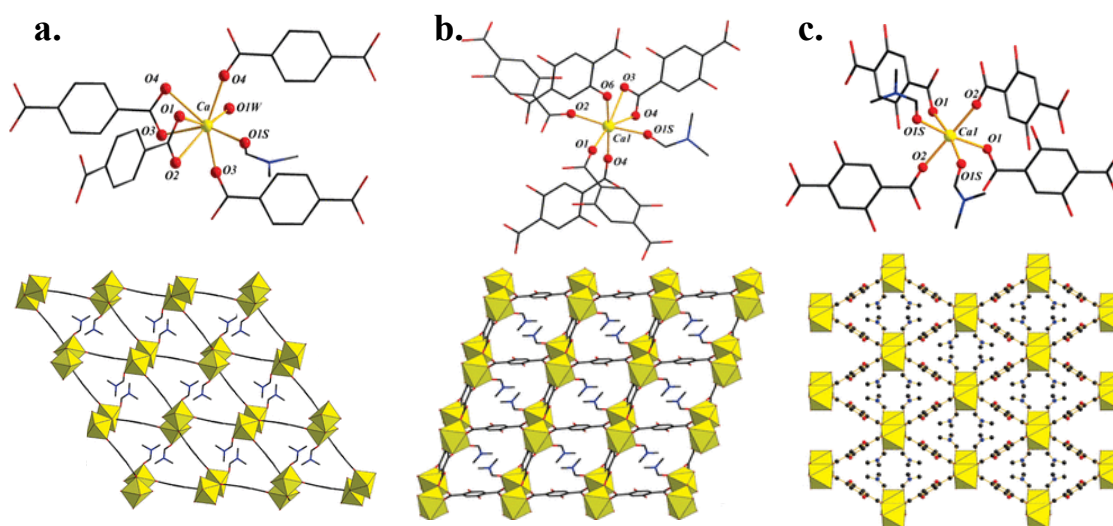


Figure 1-10 Local coordination environment of Ca^{2+} ion and structure of (a).

$\text{Ca}(\text{BDC})(\text{DMF})(\text{H}_2\text{O})$; (b). $\text{Ca}(\text{H}_2\text{dhtp})(\text{DMF})$; (c). $\text{Ca}(\text{H}_2\text{dhtp})(\text{DMF})_2$.³²

1.2.8 Sr-MOFs and Ba-MOFs

Both Sr and Ba have similar electronic character and ionic radius.³³ As the last two nonradioactive elements in alkali earth metals, they potentially have a higher coordination number compared to Ca. Employing the same organic linker, pyridine-2,4,6-tricarboxylic acid (ptcH₃), distinct structures could be constructed by introducing Sr²⁺ and Ba²⁺ ions. {Sr_{1.5}(ptc)·5H₂O}_n contains two crystallographically independent Sr(II). Sr(1) is nine-coordinated with six oxygen atoms from carboxylate groups, two nitrogen atoms from the rings of two ptc linkers, and one oxygen atom from a coordinated water molecule; Sr(2) is also in a nine-coordinated environment, but with five oxygen atoms from coordinated water molecules and four oxygen atoms from three distinct ptc ligands. {[Ba(ptc)(H₂O)][Ba(ptcH₂)H₂O]}_n undergoes more complicated construction with two distinct units. Two crystallographically independent Ba(II) ions are included, where Ba(1) is linked to four mono-dentate carboxylate oxygen atoms from four ptc ligands, two chelate oxygen atoms from another ptc ligand, one NO₂ donor from another ptc unit and one oxygen atom from coordinated water to achieve the ten-coordinated environment. Ba(2) has two less mono-dentate carboxylate oxygen atoms from two ptc units coordinated.

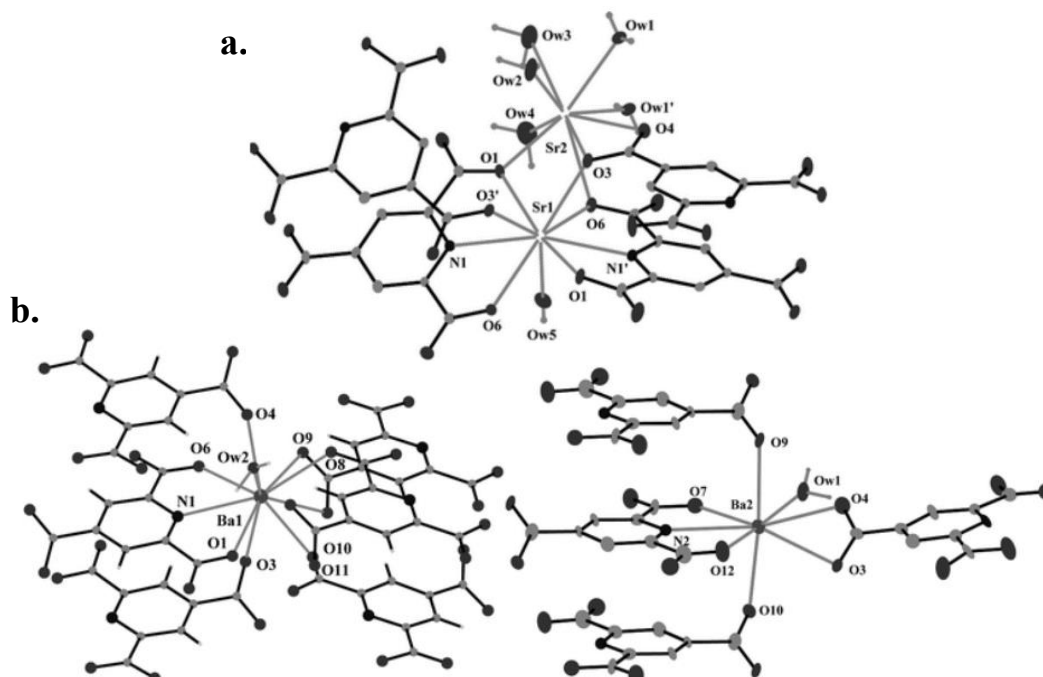


Figure 1-11 (a). Local coordination environment of Sr²⁺ ions within {Sr_{1.5}(ptc)·5H₂O}_n. (b).

Local coordination environment of Ba²⁺ ions within {[Ba(ptc)(H₂O)][Ba(ptcH₂)H₂O]}_n.³³

1.2.9 Summary of s-block metals within MOFs

All the s-block metals within MOFs are listed in the **Table 1-1** with most usual coordination number. Along the same group, as the radius of metal getting larger, the most usual coordination number gets larger as well. Additionally, the s-block metals in the same periods show the similar coordination behavior within MOFs.

Table 1-1 Most usual coordination numbers for each s-block metals within MOFs.

Alkali metal	Li	Na	K	Rb	Cs
Coordination number	4	4-7	7-8	8	8
Alkaline earth metal	Be	Mg	Ca	Sr	Ba
Coordination number	4	4 or 6	6-8	6-9	>8

1.2.10 Applications of MOFs based on s-block metals

Despite the difficulties in constructing predictable structures and investigating structures systematically, several potential applications of s-block MOFs were developed based on the unique advantages of s-block metals. Permanent porosity allows them to be used in gas storage and separation;^{28,30,34,35} active metal sites contribute to the catalytic application;^{36,37,38} nontoxicity and biocompatibility make the s-block metal-based MOFs outstanding candidates for applications within the biological field;^{39,40} with the huge abundance on the planet, Na, K, Mg, and Ca are the interested metals in MOFs for commercial purposes.

1.3 Organic ligands in MOFs

As the second component of MOFs, employing distinct organic ligands is also a key method for the design of MOFs. Usually, the type and number of donor atoms within organic ligands⁴⁴, the different atomic arrangements within ligands⁴⁵, the size of ligands⁴⁶ and the shape of ligands⁴⁷ all result in the distinct structures of MOFs and different properties of porous channels.

1.3.1 The donors within organic ligands

To construct MOFs rationally, the general strategy is to introduce the multidentate ligand with N- or O- donor, which helps form polymeric structures.⁴¹ Five membered heterocycle azolate is usually included in N-donor ligands, such as bipyridine and 1,3-bis(4-pyridyl)propane,^{42,43} where the sp^2 N-donor atoms are chelated with metal center upon deprotonation. Carboxylic acids are always considered as appropriate O-donors ligands. When the number of donor atoms in a linker is limited, it is hard to construct the 3D infinite structure. Instead, they usually generate a 2D layered structure. For instance, Moreno synthesized three Al-MOFs with organic ligands EB (4-ethylbenzoic acid), HB (4-heptylbenzoic acid) and DB (4-dodecylbenzoic acid).⁴⁴ All three ligands contain one carboxylate group where two O-donor could be found. Three 2D frameworks were formed under solvothermal conditions. (**Figure 1-12**)

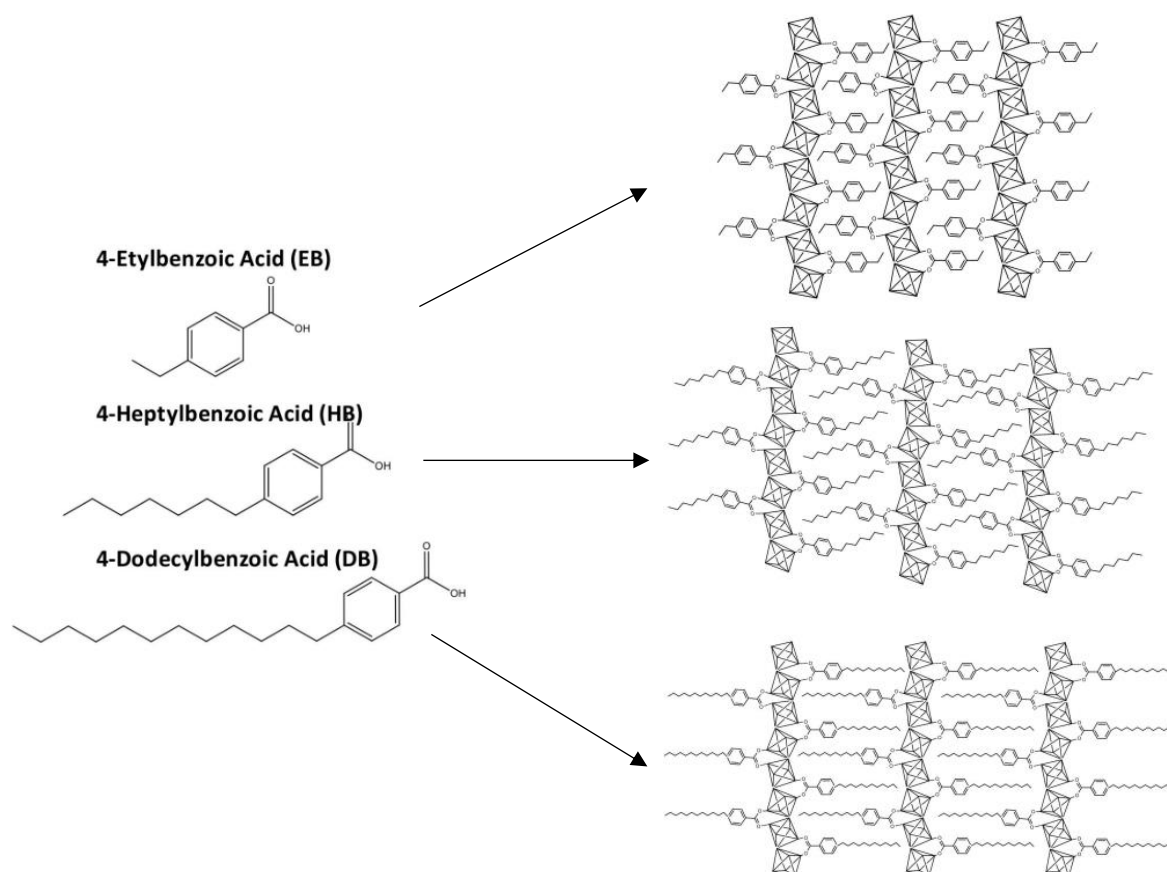


Figure 1-12 Three mono-carboxylate ligands and resulted 2D structures.⁴⁴

To construct 3D structure, di- and polycarboxylic acids are the better choices. With fully

or partially deprotonated carboxyl groups, di and polycarboxylic acid can provide various coordination cases, resulting in diverse structures with not only 2D but 3D dimensions.

1.3.2 The atomic arrangement within organic ligands

With different atom arrangements in organic linkers, such as pyrazine, pyridazine and pyrimidine, the frameworks of MOFs usually will not change. However, the properties of porous channels vary a lot, such as the gas molecule uptake capacity since the interactions between guest molecules and the frameworks are changed. Song⁴⁵ synthesized three isostructural Cu-MOFs (ZJNU-46, ZJNU-47 and ZJNU-48) with organic linkers, 5,5'-(pyrazine-2,5-diyl)diisophthalate(H₄L1), 5,5'-(pyridazine-3,6-diyl)-diisophthalate(H₄L2) and 5,5'-(pyrimidine-2,5-diyl)diisophthalate(H₄L3). All ligands have same linear structure with four carboxylate groups and three rings except the position of N atoms. Since metal centers are only coordinating with carboxylate groups, three ligands will result the MOFs with the same structure. As Song tested, all three MOFs have similar surface areas as the results of BET measurement (2622m²/g for ZJNU-46, 2638m²/g for ZJNU-47 and 2670m²/g for ZJNU-48). However, ZJNU-47 exhibited the highest C₂H₂ uptake capacity under all conditions, which demonstrated the MOFs could be further designed by rational modification of the atom sites.

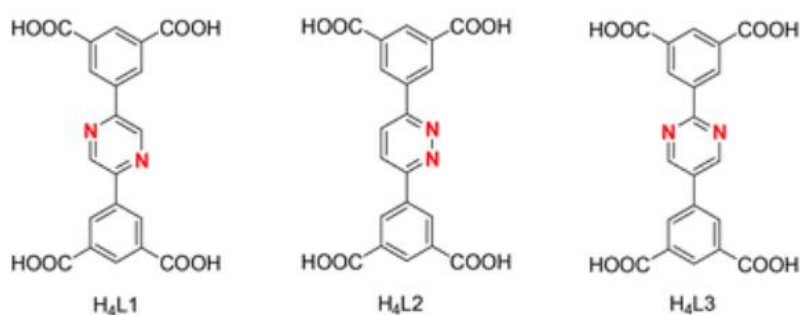


Figure 1-13 The organic linkers used to construct ZJNU-46, ZJNU-47 and ZJNU-48.⁴⁵

1.3.3 The size of organic ligands

Changing the sizes of ligands directly alters porosity. Zhang's group replaced BDC linker in Co-BDC with a longer ligand, 4,4'-biphenyldicarboxylic acid (H₂bpdc), which has an additional phenyl group. They investigated its Na⁺ storage performance as a novel anode material in sodium-ion batteries.⁴⁶ Benefiting from the expanded linear nature and the larger

cell volume, Co-bpdc exhibited a higher capacity of 169mAh/g with the desired voltage plateau for batteries and excellent capacity retention (79% after 1000 cycles).

1.3.4 The shape of organic ligands

Among thousands of organic ligands, their shapes can be linear, zigzag, V-shaped and others. Wang compared two Cu-MOFs (ZJNU-91 and ZJNU-92) (**Figure 1-14**) with zigzag and linear ligands respectively, investigating the properties of pores within these two MOFs.⁴⁷ 5,5'-(Thieno[3,2-b]thiophene-3,6-diyl) diisophthalic acid (H_4L1) and 5,5'-(thieno[3,2-b]thiophene-2,5-diyl) diisophthalic acid (H_4L2) were used where the only difference is the connection between two 5-member rings involving four carbon atoms and one sulfur atom, resulting in the linear and zigzag geometry. By single-crystal X-ray diffraction, it was proved that the coordination modes within both MOFs are identical. However, since the distinct geometries of ligands, two MOFs contain different pores in shape and size. Although ZJNU-92 showed a larger surface area of 2845 m^2/g than ZJNU-91 (2404 m^2/g) by BET measurement,

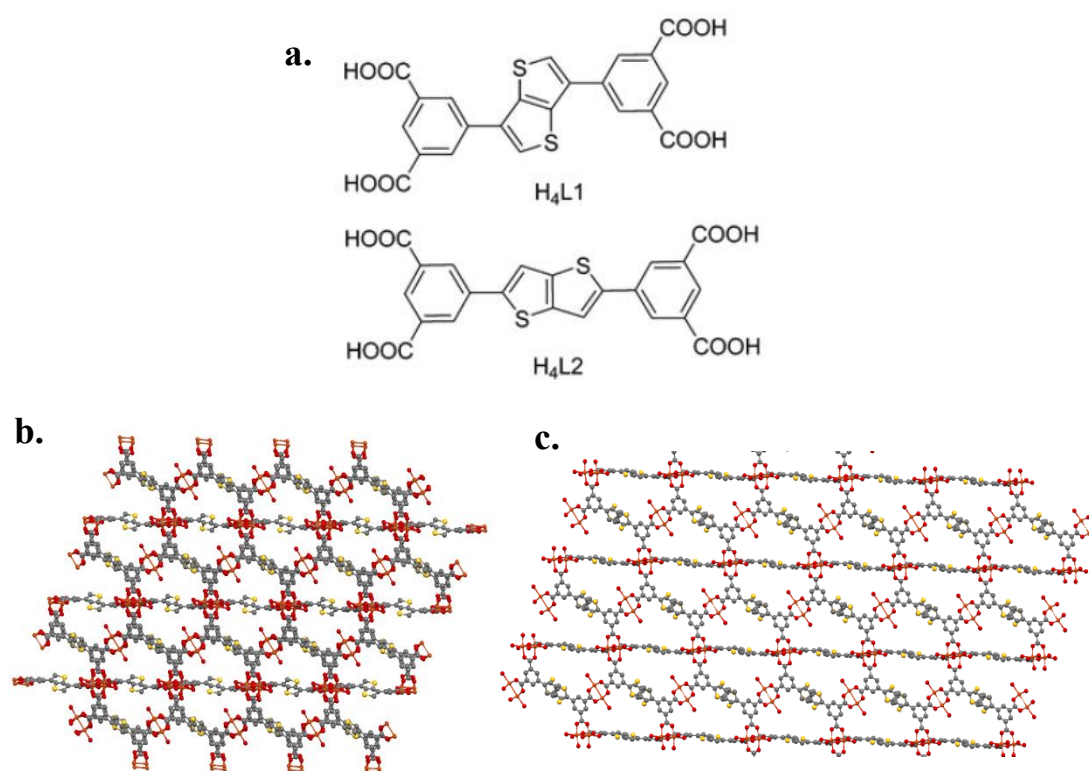


Figure 1-14 (a). The organic linkers used to construct ZJNU-91 and ZJNU-92. (b).(c). The structure of ZJNU-91 and ZJNU-92.⁴⁷

ZJNU-91 exhibited a better performance in terms of adsorption selectivity for both C₂H₂/CH₄ and CO₂/CH₄, and uptake capacity for C₂H₂ and CO₂, which could be attributed to its more optimized pore shape and size.

Compared with linear ligands, the V-shaped ligands tend to construct the helicity or other polymeric chains, which allows people to tune the structures and properties optionally.⁴⁵ With different bend angles of the V-shaped linker, diverse structures can be synthesized. Additionally, V-shaped ligands provide more opportunities for introducing distinct topologies, connectivity and chirality with unpredictable orientations.⁴⁹ Three Ni-MOFs were synthesized and reported by Wang,⁵⁰ where two asymmetric V-shaped ligands were used, 3-(4-carboxy-phenoxy)-phthalic acid (H₃L¹) and 3-(2-carboxy-phenoxy)-phthalic acid (H₃L²). [Ni₃(L¹)₂(μ-4,4'-bpy)₃(H₂O)₂]_n·(4,4'-bpy)_n·(H₂O)_{5n} was formed by Ni(II) ions, L¹ ligands and 4,4'-bpy, in which it is found to contain helices as repeating subunits. **(Figure 1-15a)** Huang also designed a novel Mn-MOF, {[Mn₂(IP)₄(oba)₂]·(oba)(H₂O)₂]_n, **(Figure 1-15b)** with both 1H-imidazo[4,5-f][1,10]-phenanthroline (IP) and V-shaped ligand 4,4'-oxybis(benzoic acid) (H₂oba).⁵¹ In this Mn-MOF, the helical chains were generated by the connections between Mn(II) ions and carboxylate groups in monodentate chelating mode. Further connected by hydrogen bonds between N atoms from IP ligands and O atoms from oba ligands, 3D network is constructed. With the π-π stacking interactions among 6-member rings, the framework was further stabilized. 3,5-bis(5-(pyridin-4-yl)thiophen-2-yl)pyridine (BPTP), a three N-donors V-shaped ligand, were employed with oba, another V-shaped ligand, to construct Zn-MOF and Cd-MOF by Han.⁵² In Zn-MOF, the 2D network with rhomb-like windows could be generated by Zn(II) ions and oba ligands. BPTP ligands further bridged to build 3D porous framework structure. **(Figure 1-15c)** It is worth mentioning the uncoordinated nitrogen atoms of middle pyridine are exposed in pores. Cd-MOF showed a more complicated structure, where the nitrogen atoms of middle pyridine are coordinated with Cd(II)(1). **(Figure 1-15e)** With four oxygen atoms from two oba ligands bidentate coordinated and one oxygen atom from coordination water, Cd(II)(1) constructs a strongly distorted octahedral geometry. Cd(II)(2) is coordinated with two oxygen atoms from one bidentate coordinated oba ligand, two oxygen atoms from two monodentate coordinated oba ligands and two nitrogen atoms from two terminal pyridines of two distinct IP

ligands. A slightly distorted octahedron is constructed around Cd(II)(2).

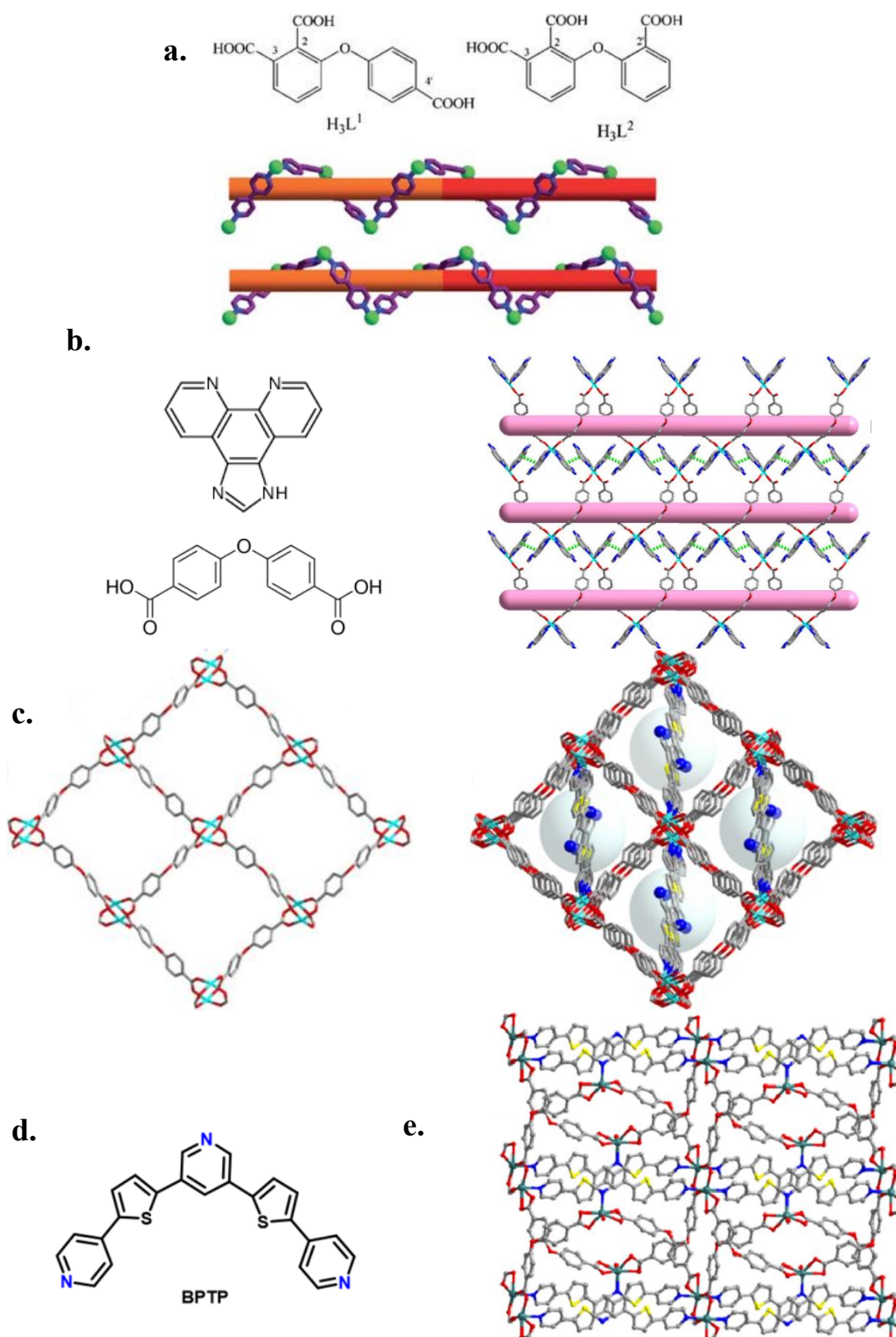


Figure 1-15 (a). The organic linkers used in Ni-MOFs and the helical chains. (b).The organic linkers used in Mn-MOF and the structure of Mn-MOF (c). The 2D network and 3D structure in Zn-MOF. (d). The organic linkers used in Zn-MOF and Cd-MOF. (e). 3D structure of Cd-MOF.

1.4 Organic ligands studied in this thesis

In this thesis, we chose 4, 4'- sulfonyldibenzoic acid (H_2SDB),⁵³ one of the typical V-shaped dicarboxylates, and squaric acid ($H_2C_4O_4$), one of the top-performing rigid organic ligands in MOFs.^{62,63}

In recent years, the MOF systems involving SDB-based linker has shown a high CO_2/N_2 selectivity⁵⁴⁻⁵⁷ And several MOFs based on s-block metal and SDB linker have been reported.⁵⁸⁻⁶¹ There are six potential donor atoms (oxygen) within the H_2SDB , which will result in a distinguished coordination environment with s-block metals.

Squaric acid ($H_2C_4O_4$) has four potential donor atoms (oxygen). By the constrained square linkers, high pore rigidity can be observed with minimum rotation and distortion after squaric acid coordinates with the metal center, which helps to control the pore size.^{62,63}

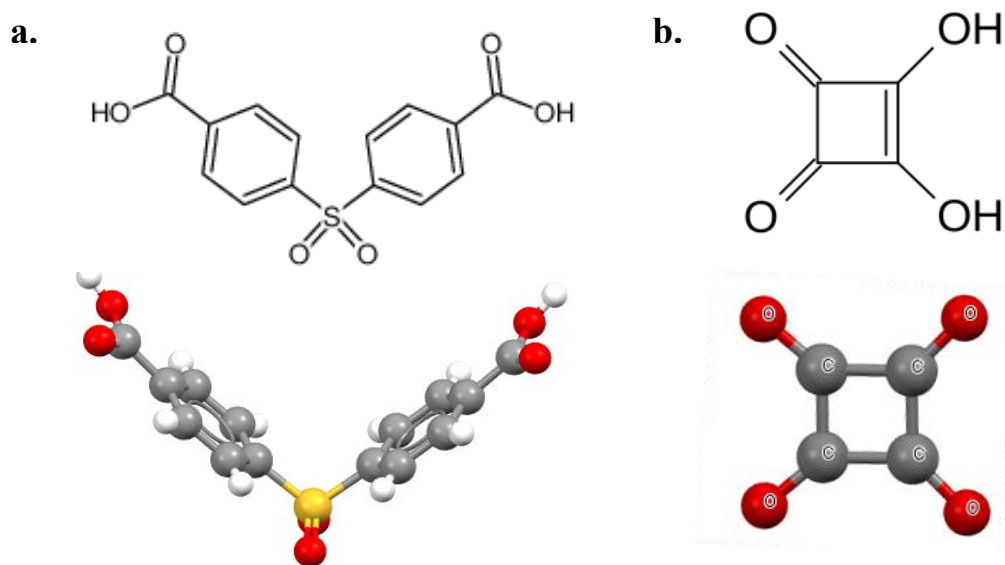


Figure 1-16 2D and 3D structure of H_2SDB (a) and $H_2C_4O_4$ (b).

1.5 Introduction of solid-state nuclear magnetic resonance (SSNMR)

Nuclear magnetic resonance (NMR) spectroscopy has been a major technique for studies of solids and liquids since it was first discovered in 1938 by Isidor Rab, which earned him the Nobel Prize in Physics in 1944. With the expansion of NMR into liquids and solids by Felix Bloch and Edward Mills Purcell in 1946, they were offered the Nobel Prize in Physics in 1952.

Several techniques are employed to characterize the synthesized MOFs, explore the

structure and investigate the local interaction between the framework and guest molecules. SSNMR is one of the most powerful methods for material characterization, especially for the investigation of the local environments of nuclei of interest.⁷⁰ One of the most typical uses of SSNMR is the determination of the local structures of target nuclei. Additionally, SSNMR can also reveal the dynamic information of adsorbed gas molecules within MOFs.

There are two fundamental factors which are critical to SSNMR: nuclei spins (I), which is an intrinsic property, and an applied magnetic field (B_0), which is an extrinsic property.^{71,72,73} To be magnetically active, the nuclei with a non-zero spin quantum number is required. By counting the number of protons or neutrons, whether the nucleus is magnetically active or not can be predicted.⁷⁴ For instance, If the numbers of protons and neutrons are both even, this nucleus is magnetically inactive; In contrast, if either the number of protons or neutrons are odd, this nucleus is magnetically active. (**Table 1-2**) ^{13}C has 6 protons and 7 neutrons with $I = 1/2$ and spherical distribution of charges in the nucleus, which makes ^{13}C a suitable nucleus in NMR measurement. Besides I and B_0 , radio frequency (rf) field is required as well. When the nuclear spin system is placed in the external magnetic field (B_0), rf radiation is employed to result in a second rf field (B_1), which is used to cause “perturbation”. A voltage change within the coil of the NMR probe will be induced when B_1 is removed, generating free induction decay (FID), where FID is a time domain signal which can be transferred into a frequency domain spectrum by Fourier transformation (FT).

Table 1-2 The prediction of spin quantum number I according to the number of protons and neutron.

Number of protons	Number of neutrons	Nuclear spin quantum number	Example
Even	Even	Zero	^{12}C
Even	Odd	Half-integer (i.e. 1/2)	^{13}C
Odd	Even	Half-integer (i.e. 3/2)	^7Li
Odd	Odd	Integer	^2H

1.6 NMR interactions

In the presence of an external magnetic field, the nuclear spin will undergo several typically interactions in NMR, which can be summarized within the formula $\hat{H}_{\text{NMR}} = \hat{H}_{\text{Z}} + \hat{H}_{\text{rf}} + \hat{H}_{\text{CS}} + \hat{H}_{\text{D}} + \hat{H}_{\text{J}} + \hat{H}_{\text{Q}}$,⁷³ corresponding to Zeeman, radio frequency interaction, magnetic shielding interaction, dipolar coupling, J-coupling and quadrupolar interactions. The magnitudes for these typical NMR nuclear spin interactions are listed in **Table 1-3**.

Table 1-3 Estimated magnitudes of typical NMR nuclear spin interactions.

Interactions	Magnitude (Hz)
Zeeman	10^7 - 10^9
Magnetic shielding	10^3 - 10^5
Dipolar coupling	10^3 - 10^4
J-coupling	0- 10^3
Quadrupolar	10^3 - 10^7

1.6.1 Zeeman interaction

Zeeman interaction, known as the strongest one among all interactions, refers to the interaction between B_0 and a nuclear spin. A nucleus with the spin I has $2I+1$ possible energy levels in the degenerate ground state when external magnetic field B_0 is not applied. Due to the interaction between the magnetic moment of the nuclear spins and B_0 when B_0 is applied, the spin states which were at the same energy will split and form $2I+1$ energy levels distinguished by magnetic quantum number m_I ($m_I = -I, -I+1, -I+2, \dots, I-2, I-1, I$). In such case, Zeeman interaction results in an energy gap between adjacent energy levels, and Larmor frequency (ν_0) refers to the rate of transitions between two adjacent energy levels which is proportional to the gyromagnetic ratio γ of a given nuclei and the strength of external magnetic field B_0 . (h is Planck's constant)^{72,75} **Figure 1-17** illustrate the Zeeman interaction in a nucleus with $I=1/2$ as an example. Thus, a stronger NMR signal is obtained when applying a higher magnetic field.

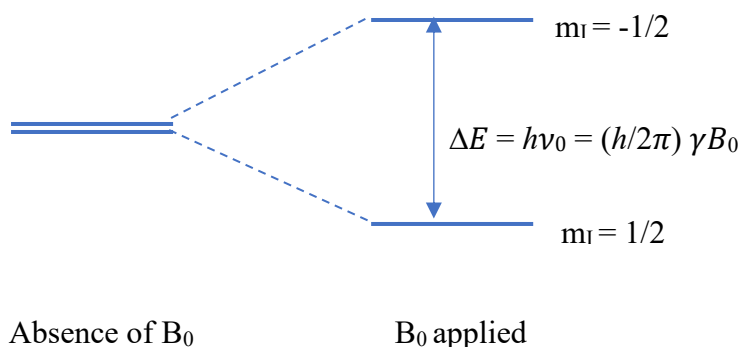


Figure 1-17 Illustration of Zeeman interaction within nucleus with $I=1/2$.

1.6.2 Magnetic shielding interaction

When applying an external magnetic field, a small secondary magnetic field will also be generated by the additional motion of the electron surrounding the nucleus (electron cloud), which shields or deshields the nucleus, resulting in a frequency deviation. For instance, if the secondary magnetic field has the opposite direction to the main magnetic field, the nucleus is shielded from the B_0 . The influence of nuclear magnetic shielding interaction (NMS) (or called chemical shielding) on Zeeman interaction is expressed as:⁷²

$$\nu = \frac{\gamma}{2\pi} B = \frac{\gamma}{2\pi} B_0 (1 - \sigma)$$

where ν refers to the modified resonance frequency, B refers to the modified magnetic field, and σ is a second-rank magnetic shielding tensor, which refers to the nuclear magnetic

shielding constant and can be described by $\sigma = \begin{pmatrix} \sigma_{xx} & \sigma_{xy} & \sigma_{xz} \\ \sigma_{yx} & \sigma_{yy} & \sigma_{yz} \\ \sigma_{zx} & \sigma_{zy} & \sigma_{zz} \end{pmatrix}$ in principal axis system

(PAS)⁷³. PAS orients within the molecular framework, where three chemical shielding tensor components ($\sigma_{11}, \sigma_{22}, \sigma_{33}$) can be defined from the diagonal of symmetrized chemical

shielding tensors matrix in PAS, $\sigma^{\text{PAS}} = \begin{pmatrix} \sigma_{11} & 0 & 0 \\ 0 & \sigma_{22} & 0 \\ 0 & 0 & \sigma_{33} \end{pmatrix}$. By further converting three principal

components using $\delta = \frac{\sigma_{ref} - \sigma}{\sigma_{ref}} \approx (\sigma_{ref} - \sigma)$, three chemical shift (δ_{11}, δ_{22} and δ_{33}) can be

obtained, which are commonly used in NMR spectra. For $\sigma_{11}, \sigma_{22}, \sigma_{33}$, σ_{11} refers to the least shielded component while σ_{33} refers to the most chemical shielded component ($\sigma_{11} < \sigma_{22} < \sigma_{33}$). In such case, δ_{11} will appear at the highest frequency while δ_{33} will show up at the lowest

frequency after converting ($\delta_{11} > \delta_{22} > \delta_{33}$).⁷³ A typical spectrum with δ_{11} , δ_{22} and δ_{33} labeled is shown in **Figure 1-18**.

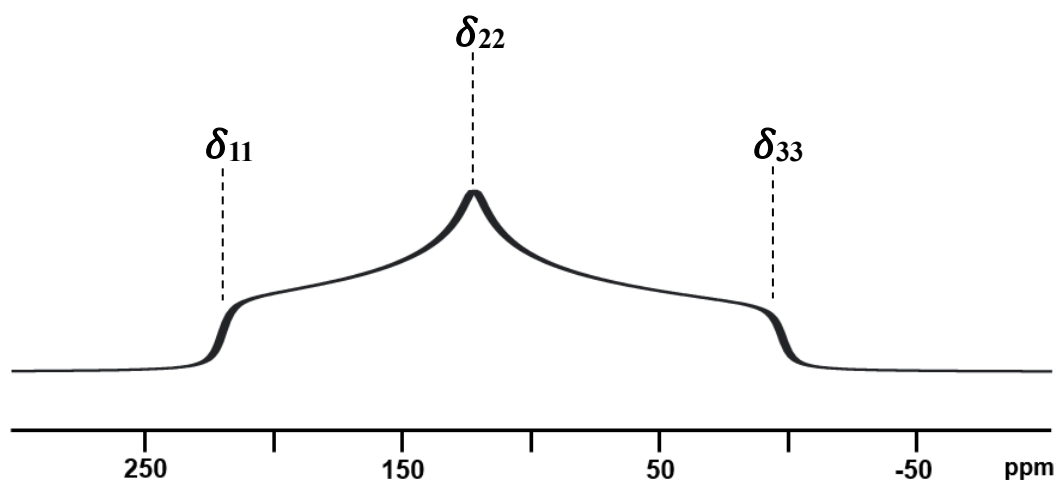


Figure 1-18 A typical powder spectrum with labelled three chemical shift components.⁷³

In solid-state NMR, due to that the magnetic shielding interaction is anisotropic, a static NMR spectrum is highly sensitive to molecular motions. The magnetic shielding interaction is anisotropic, meaning that the frequency of nuclei in a molecule depends on the orientation of the molecules with respect to the external magnetic field. All possible orientations can be found in small crystallites for a powder sample. The observed powder pattern is considered a distribution of frequency. While in solution NMR, molecules undergo rapid reorientation, which averages out the chemical shielding anisotropy (CSA) and results in sharp peaks.

A wide line NMR spectrum with chemical shielding anisotropy is usually described by three parameters including the isotropic chemical shift (δ_{iso}), span (Ω), and skew (κ) (Hertzfeld-Berger convention)⁷⁸ where $\delta_{iso} = \frac{\delta_{11} + \delta_{22} + \delta_{33}}{3}$, $\Omega = \delta_{11} - \delta_{33}$ and $\kappa = \frac{3(\delta_{22} - \delta_{iso})}{\Omega}$. In particular, isotropic chemical shift (δ_{iso}) refers to the position of the pattern. The different δ_{iso} values for the same nucleus can deliver information about the distinct chemical environments of that nucleus. Span (Ω) is the measure of the breadth of the signal and skew (κ) exhibits the symmetry of the spectrum, ranging from -1 to 1. The influence of each parameter on the observed spectrum is illustrated in **Figure 1-19**.⁷⁸

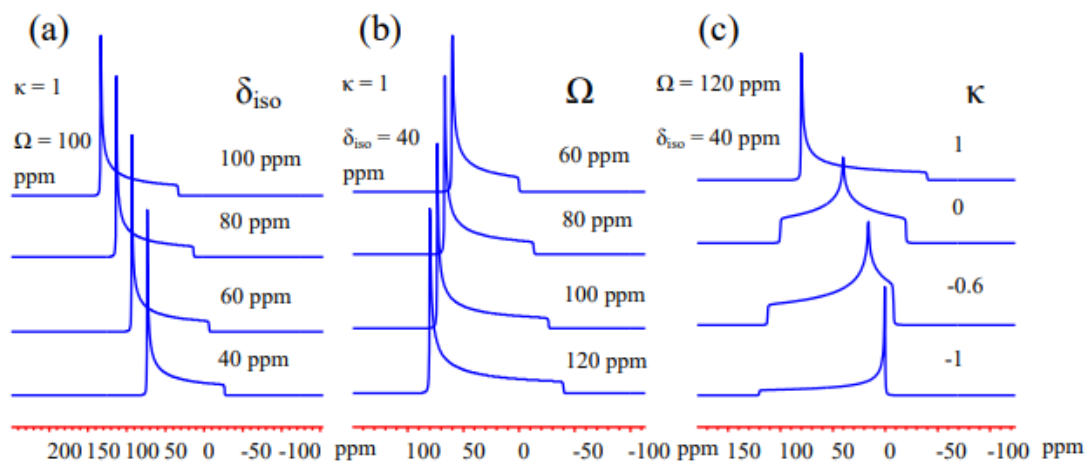


Figure 1-19 The influence of δ_{iso} (a), Ω (b), and κ (c) on a static NMR spectrum.⁷⁸

As the molecule that will be discussed in this thesis, the CO_2 in the gas phase will display a sharp line (small span) at 125 ppm due to rapid reorientation. However, when CO_2 isotropic motion is restricted, such as adsorbed by MOFs or at a lower temperature, the molecular reorientation is not fast enough to average the chemical shielding interaction to its isotropic value, resulting in a larger span. The CO_2 molecule with three chemical shielding tensor components and the ^{13}C SSNMR spectrum of solid CO_2 are shown in **Figure 1-20**. Since CO_2 molecule is axially symmetric, σ_{11} and σ_{22} are perpendicular to each other, while σ_{33} is perpendicular to $\sigma_{11}\sigma_{22}$ plane. By this theory, whether CO_2 molecules are adsorbed can easily be determined by the lineshape. temperature can often slow down the motions of CO_2 adsorbed in the MOFs, leading to a broader pattern (larger span) at low temperatures.

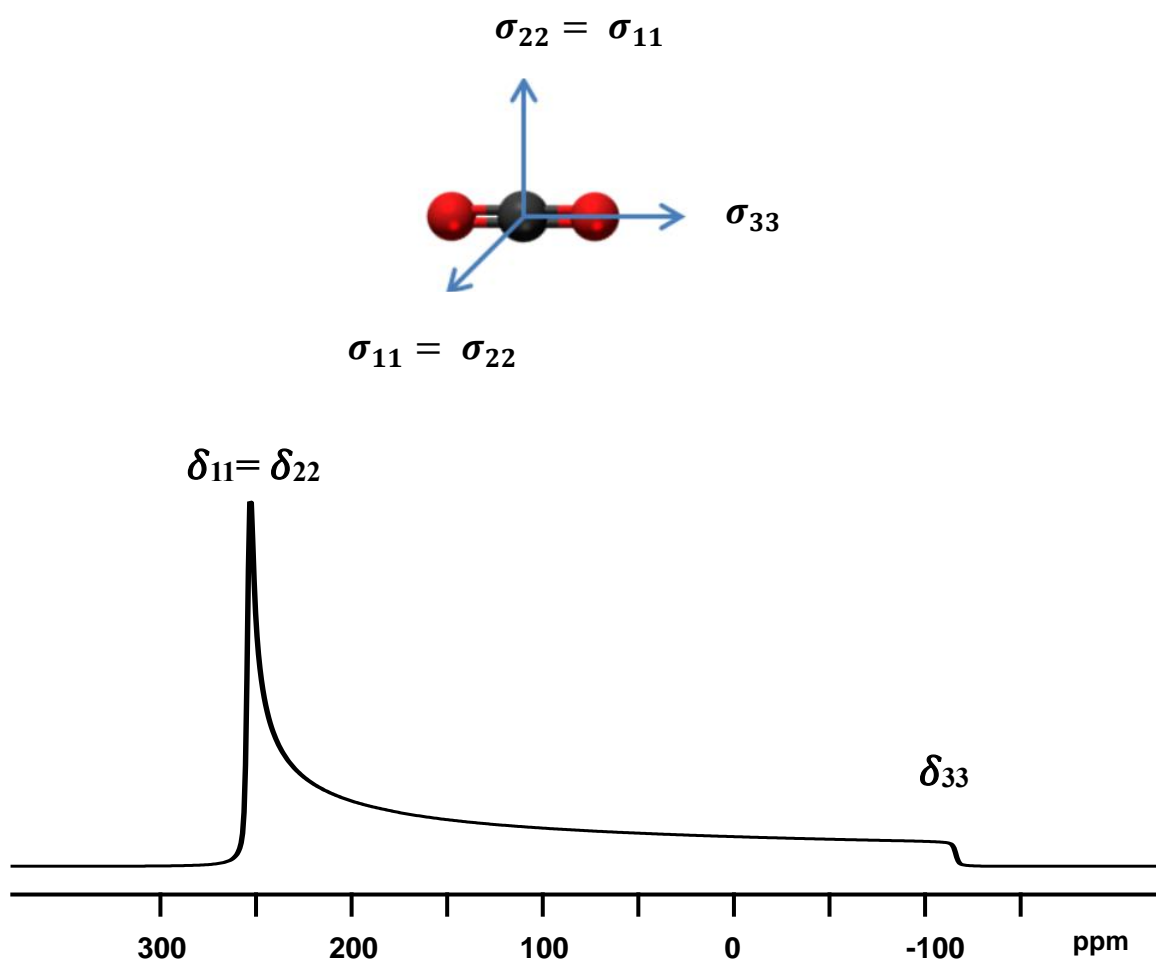


Figure 1-20 PAS of CO₂ molecule⁷⁶ and the ¹³C SSNMR spectrum of rigid CO₂ molecule where $\delta_{\text{iso}}=125$ ppm, $\Omega=335$ ppm and $\kappa=1$.⁷⁷

1.6.3 Dipolar interaction

Dipolar interaction happens via space between two spins, denoted as I and S.⁷² Two adjacent spins have distinct magnetic moments, which can be considered as two small bar magnets, and they generate two small local fields felt by each other. The strength of the dipolar interaction is quantified by dipolar coupling constant (D): (where μ_0 is the permeability of vacuum; r is the inter-nuclear distance; γ_I and γ_S are the magnetogyric ratios for the spin I and S respectively)

$$D = \frac{\mu_0 \gamma_I \gamma_S \hbar}{4\pi r^3 2\pi}$$

In such case, the modified frequency is orientation dependent and can be calculated by: (where ν_L is the Larmor frequency and α is the angle between inter-nuclear vector and the direction

of external magnetic field)

$$\nu = \nu_L \pm \frac{1}{2}D(1 - 3 \cos^2\alpha)$$

Pake doublet⁸⁰ is the typical NMR spectrum of dipolar interaction, which contains two mirrored powder patterns with two “horns” and two “feet” attributed to the opposite dipolar perturbation to Zeeman interaction. (**Figure 1-21**) When the I-S vector is perpendicular to the external magnetic field B_0 , “horns” are derived, while “feet” are exhibited when the I-S vector is parallel to the B_0 . Additionally, the frequency gaps between two “horns” and two “feet” are equal to D and $2D$ correspondingly when observing at an isolated I-S pairs. Experimentally, dipolar interactions resulting from multiple spins will broaden the NMR signals and lead to a featureless spectrum, resulting the difficulties in further analysis.

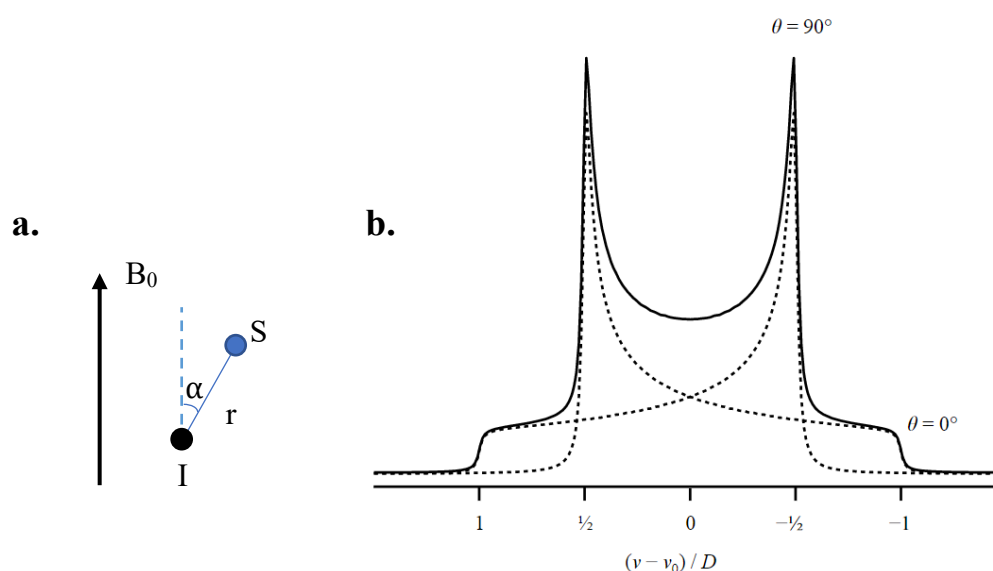


Figure 1-21 (a). The demonstration of the principle of dipolar interaction. (b). Pake doublet and patterns (dotted lines) which refers to the dipole perturbation of nuclei S either enhance or cancel the magnetic field that I experiences.⁸⁰

1.6.4 J-coupling interaction

Compared to dipolar interaction, J-coupling interaction is much weaker and originated from the chemical bonds between nuclei. Since the relatively small magnitude of J-coupling interaction, it is less often observed in broad lineshape SSNMR compared to that in solution NMR.⁷³

1.6.5 Quadrupolar interaction

A quadrupolar nucleus (spin-quantum number $> 1/2$) holds an electric quadrupole moment since the nuclear charge distribution is non-spherical. The electric quadrupole moment will interact with the electric field gradient (EFG) which is the change in electric field due to the local distribution of nuclear and electronic charges. Quadrupolar interaction is the interaction between the quadrupole moment and the EFG. Similar to chemical shielding interaction, the EFG is described by the second-rank tensor in PAS with V_{xx} , V_{yy} , V_{zz} , where $V_{zz} > V_{yy} > V_{xx}$. In such cases, quadrupolar interaction can be described by two parameters, the quadrupolar coupling constant (C_Q) and the asymmetry (η_Q):^{72,73} (where e is the elementary charge)

$$C_Q = \frac{eQV_{zz}}{h}$$

$$\eta_Q = \frac{V_{xx} - V_{yy}}{V_{zz}}$$

C_Q describes the strength of quadrupolar interaction, in which the smaller value corresponds to the higher spherical symmetry of the local environment of the quadrupolar nucleus, giving the weaker quadrupolar interaction. η_Q indicates the axial symmetry of the EFG tensors, ranging from 0 to 1, where the smaller η_Q corresponds to the higher axial symmetry.

With only Zeeman interaction, a total of $2I+1$ energy levels are generated, separated by identical transitional energy. Further affected by the quadrupolar interactions (first-order \hat{H}_Q^1 and second-order \hat{H}_Q^2), the energy levels will shift by different extents. (**Figure 1-22a**)^{81,83} For the nuclei which have relatively low quadrupole coupling constant, Zeeman interaction is still dominating. First-order quadrupolar interaction is treated as the full quadrupolar interaction. When the quadrupolar interaction is above 5% of Zeeman interaction, the second-order quadrupolar interaction will be considered as well.⁸² For nuclei with half-integer I , the energy between central transition (CT) ($\frac{1}{2} \leftrightarrow -\frac{1}{2}$) is not affected by the first-order quadrupolar interactions on two energy levels are equal. While the second-order quadrupolar interaction affects central transition and satellite transitions (ST). The spatial portion of these energy contributions from quadrupolar interactions can be further described as spherical harmonic oscillations P_2 and P_4 :⁸¹ (where θ refers to the angle between the EFG symmetry axis and the direction of the external magnetic field)

$$\hat{H}_Q^1 : P_2(\cos\theta) = \frac{1}{2}(\cos^2\theta - 1)$$

$$\hat{H}_Q^2 : P_4(\cos\theta) = \frac{1}{8}(35\cos^4\theta - 30\cos^2\theta + 3)$$

Since the ST are strongly dependent on θ , the intensity of ST peaks will spread over wide frequency range. The typical NMR patterns for nuclei ($I=3/2$) with first-order quadrupolar interaction is shown in **Figure 1-22b**, which is composed by a sharp CT peak with high intensity and two low-intensity ST peaks.⁸⁴ Further influenced by second-order quadrupolar interaction, the CT peak will exhibit two ‘‘horns’’. (**Figure 1-22c**)⁸⁴

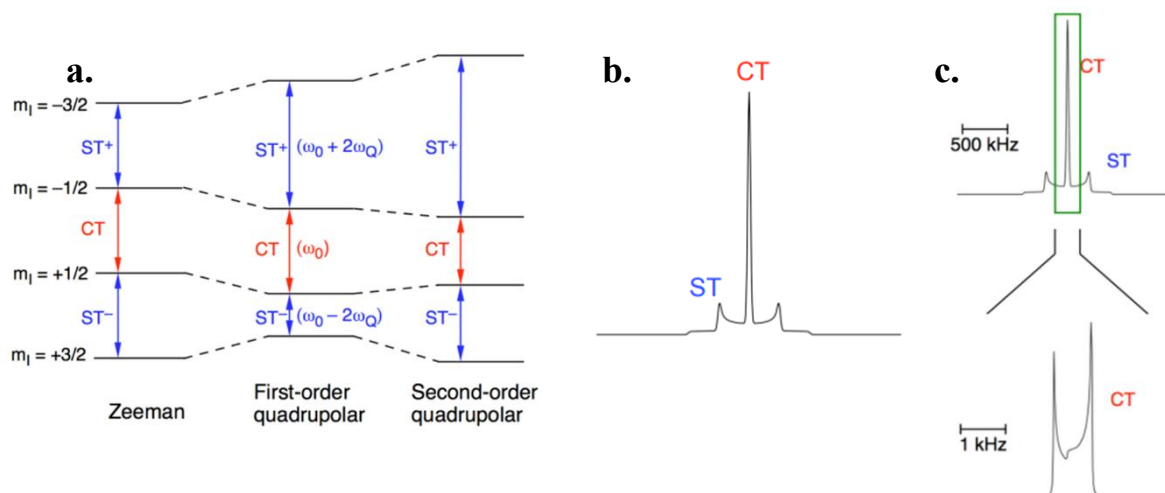


Figure 1-22 (a). the energy level and transition with Zeeman interaction, first-order and second-order quadrupolar interaction. ($I=3/2$ as example; $\omega_Q = 3C_Q/4I(2I-1)$, called quadrupolar splitting parameter) (b). The typical spectrum with only first-order quadrupolar interaction. (c). The CT peak affected by the second order quadrupolar interaction.⁸⁴

1.7 Techniques of SSNMR

1.7.1 Single-pulse

Single-pulse sequence, also called one pulse sequence, is the simplest and the most fundamental sequence in any NMR. When the sample is placed in the B_0 , a net magnetization (M_0) is generated by the net magnetic moments of the nuclei in the direction of B_0 . The detection coil of the NMR probe is lying in the xy plane of the rotating frame. Thus, to make M_0 detectable, a second magnetic field B_1 along the x axis is applied to give the 90° rotation of

magnetization from the z-axis to the xy plane. As the M_0 is rotated to the xy plane, B_1 is switched off. With the M_0 relaxes back to the z-axis, an oscillating signal, called free induction decay (FID), is recorded in the time domain. (Figure 1-23) Fourier transformation (FT) is then employed to convert the signals from time domain into the frequency domain.⁷²

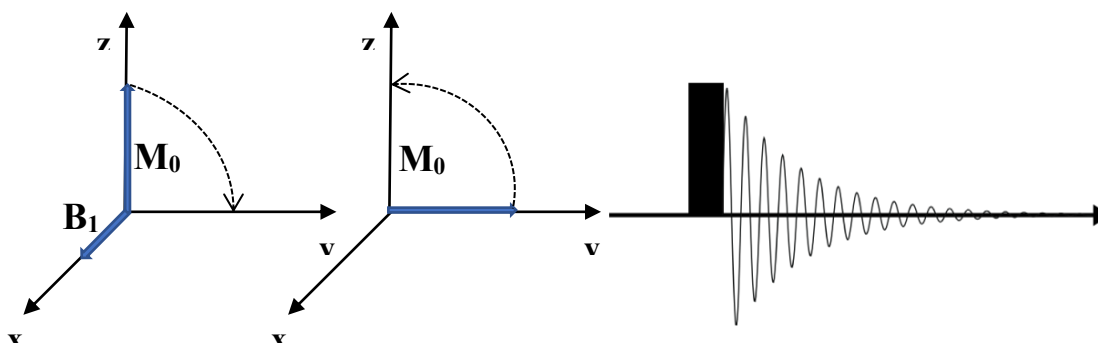


Figure 1-23 The scheme of one pulse sequence.⁷²

1.7.2 Spin-echo

Based on single-pulse, several sequences are then designed to achieve specific purposes. Spin-echo sequence is used in this thesis to acquire static ^{13}C SSNMR spectra of CO_2 . In solid state NMR, ideally, when B_1 is removed, the receiver should be turned on immediately after a perfect 90° pulse and the signal should be immediately recorded for the nuclei that have short T_2 relaxation time, such as ^{13}C . However, there is always a dead time between the end of the 90° pulse and the start of signals collection to prevent pulse breakthrough and imperfection. In such case, the signals will not be collected fully, which results in the partial loss of FID, leading to a broad and truncated powder pattern. The spin-echo sequence is then employed. Moreover, the spin magnetizations with different frequencies will lose their phase coherence during the dead time, causing a distorted NMR lineshape not only in SSNMR but also in liquid or gas phase NMR. The spin-echo sequence starts with a 90° pulse that rotates the net magnetization M_0 to the x-y plane, followed by an echo dephasing time τ_1 . During this time, M_0 starts to evolve with different pace in the x-y plane since the spins are with different frequencies. Then a 180° pulse is applied along the y axis followed by a second delay τ_2 . At the end of τ_2 , an echo is formed and the magnetization M_0 is refocused, after which FID can be fully collected.^{72,85} (Figure 1-24) Additionally, the spin-echo sequence can also be used for measuring T_2 relaxation time by optimizing the τ and obtaining the intensity of the signal,

because the natural distribution of frequencies due to T_2 relaxation process cannot be refocused.⁸⁶

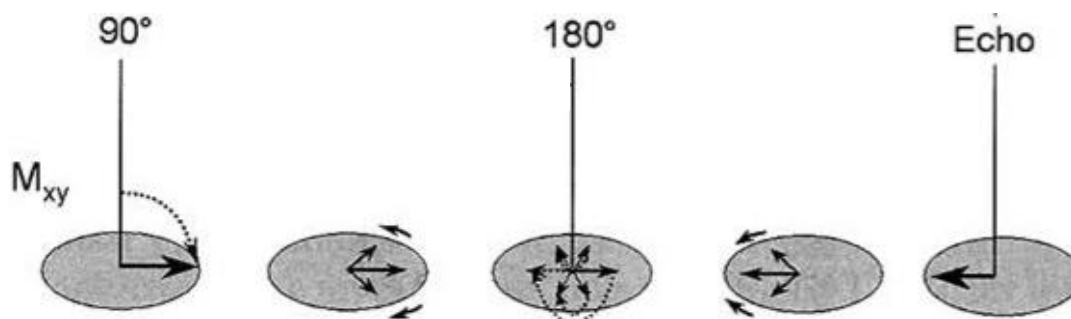


Figure 1-24 The scheme of echo sequence.⁸⁵

1.7.3 Cross polarization (CP)

Given the long relaxation time, low natural abundance or low gyromagnetic ratio, there are several nuclei that are NMR unfavorable, which means the spectra of these nuclei always exhibit low signal-to-noise ratio (S/N). Cross polarization is designed to transfer magnetization from abundant spins (such as ^1H or ^{19}F) to dilute spins (such as ^{13}C) to increase the S/N. Hartmann-Hahn condition explains the relationship between two nuclei in polarization transfer with different Larmor frequency:⁸⁷ (where B_I and B_S refer to the radio frequency field that applied for two nuclei)

$$\gamma_I B_I = \gamma_S B_S$$

^1H - ^{13}C cross polarization is the most common sequence in CP experiments. 90° pulse is firstly applied on ^1H channel followed by a spin lock pulse B_I , avoiding magnetization from dephasing. During the contact time, the magnetization of ^{13}C will be generated in the xy plane due to the dipolar coupling interaction. After that, ^1H channel starts to decouple while ^{13}C FID is collected. (**Figure 1-25**)⁷⁹

The rate of magnetization transfer in a CP experiment depends on the strength of the dipolar coupling between spin I and S . In this case, the stronger the dipolar coupling interaction, the faster the transfer. And the longer the contact time, the further the spin I that the polarization can be transferred from.

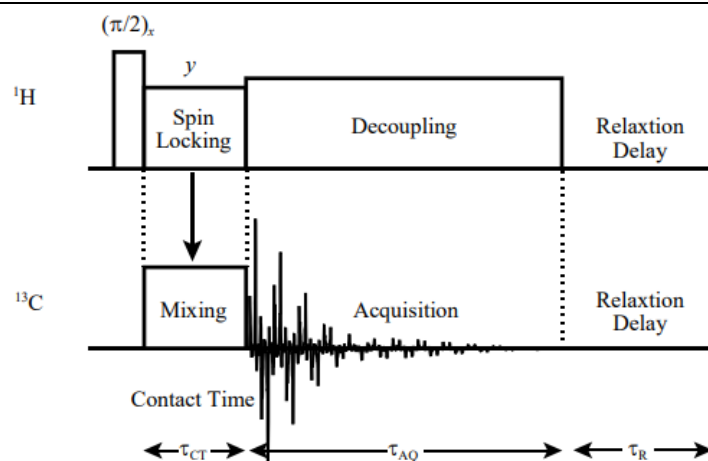


Figure 1-25 Pulse sequence of CP (Cross polarization)⁷⁹

1.7.4 Magic-angle spinning (MAS)

Besides various designed sequences, there are also several methods to eliminate or average specific interaction, which helps increase the resolution of spectra. Dipolar interaction, magnetic shielding interaction and first-order quadrupolar interaction both contain $(3\cos^2\theta - 1)$ terms where θ is the angle between the z-axis of the PAS and the direction of B_0 . By employing magic-angle spinning, where the sample will be placed in a rotor sitting on the axis at the magic angle (54.74°) with respect to B_0 ($3\cos^2(54.74^\circ) - 1 = 0$), (**Figure 1-26**)⁷⁹ the dipolar interaction, chemical shielding interaction and the first-order quadrupolar interaction are averaged out. In the other words, all the interactions are reduced to their isotropic values. However, If the spinning rate is less than the magnitude of anisotropic interactions, there will be spinning sidebands located on both sides of the isotropic peak separated in the frequency domain by a frequency equal to the rate of spinning (Hz). Additionally, only the isotropic peak does not change its frequency with different spinning speed. Thus, by increasing the spinning speed, the spectrum with more clear resonances can be obtained.

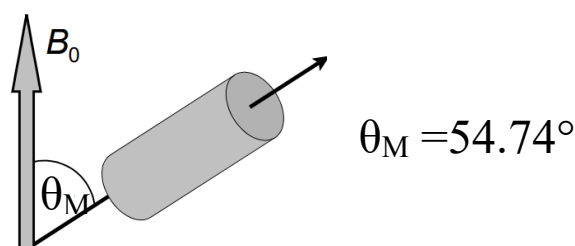


Figure 1-26 Schematic diagram of Magic-angle spinning.⁷⁹

1.7.5 Multiple-quantum magic-angle spinning (MQMAS)

As mentioned before, by using MAS, the first-order quadrupolar interaction with second-rank terms is averaged. However, if the second-order term is considered, it requires other methods to obtain the spectra with high resolution. A method called multiple-quantum magic-angle spinning experiment (MQMAS) was introduced by Frydman and his coworker in 1995.⁸⁸ They found that the second-order quadrupolar interaction can be averaged during the multiple quantum transition evolution. Although the multiple quantum transitions cannot be detected directly, they can be detected indirectly by 2D experiment. The two-pulse sequence of MQMAS is shown in **Figure 1-27**⁸⁹ where the first pulse excites transitions in the quadrupolar spin system, and the interested multiple quantum coherence then can be selected by the cycled phase. Usually, triple quantum is picked considering the excitation efficiency and every half-integer nucleus has the energy transition $\langle +3/2 \leftrightarrow -3/2 \rangle$. After t_1 evolution period, the second pulse is introduced, which converts triple quantum coherence to observable single quantum coherence. Then the normal FID is acquired during t_2 . the relationship of the signal without second order quadrupolar interaction and corresponding t_1 can be plotted as the isotropic FID (F1). While the signals acquired during t_2 give a combination of FIDs with normal MAS under different t_1 (F2). After FT, the spectrum will show two dimensions map (MAS and isotropic).



Figure 1-27 Two-pulse sequence and the example of 3Q-MAS in a spin $I=5/2$ system.⁸⁹

1.8 SSNMR spectrum simulations

The NMR spectra of molecules can be simulated in two types: analytical (WSolids) and dynamic (EXPRESS), which can help to reveal more information on the interested nuclei and even the motion of molecules where interested nuclei is included.

1.8.1 ^{13}C static NMR of CO_2

^{13}C static spectra can be calculated by WSolids package⁹¹ and EXPRESS⁹² when the motional rate and type of motions are assumed, thus, the simulated spectra, which show high agreement with experimental spectra, can reveal the possible motion of CO_2 . Two typical molecular motions are wobbling and hopping, where wobbling refers to the localized rotation along an axis at adsorption sites while hopping refers to the distinct jumping among adsorption sites. With different molecule orientations and rotation angle, various lineshapes can be calculated.⁹³ As shown in **Figure 1-28**, the left part demonstrates the powder pattern changes with increasing wobbling angle α and fixed $\beta = 0$, where α refers to the angle between the carbon-oxygen bond and C_3 rotation axis; β refers to equivalent rotation angle for C_2 hopping. While the right part shows the changes of powder pattern with various β and fixed $\alpha = 30^\circ$. It is worth mentioning that all wobbling rotations with more than 3 folds will result in the same powder pattern.

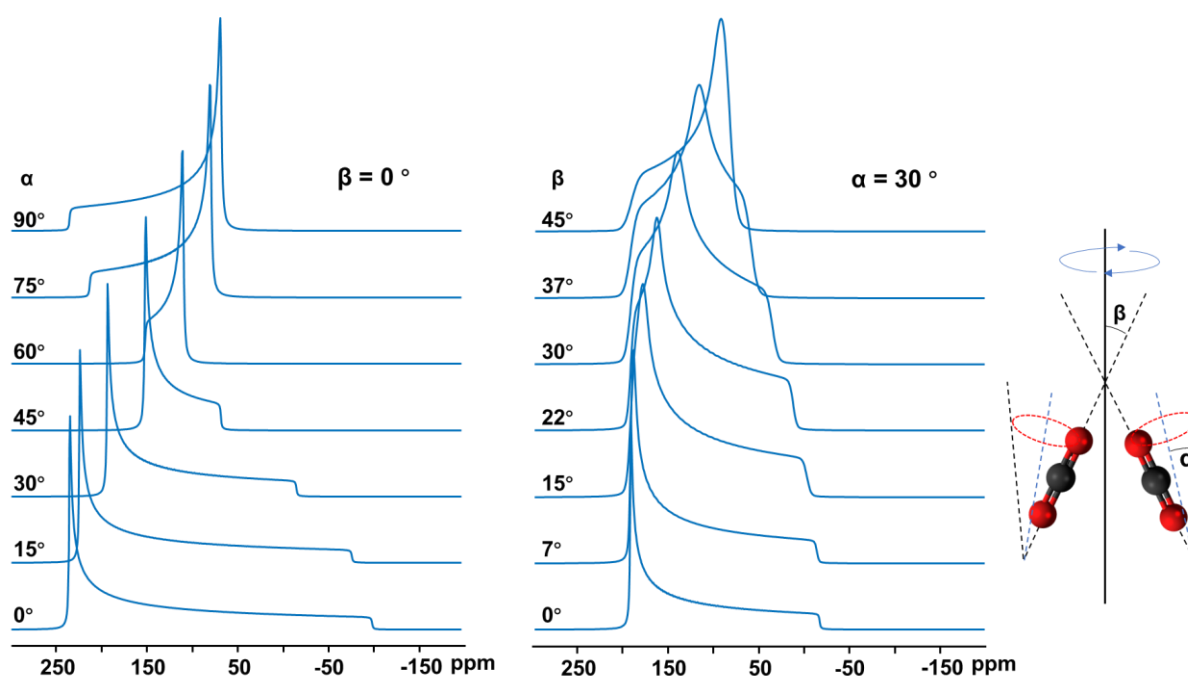


Figure 1-28 ^{13}C SSNMR simulation spectra of CO_2 with changing wobbling and hopping angles in fast motion regime with a motional rate of $1 \times 10^7 \text{ s}^{-1}$.

1.8.2 ^2H static NMR

^2H SSNMR spectroscopy is widely used for studying the molecular dynamics of molecules

that contain H. Due to the spin quantum number I is equal to 1, ^2H is a quadrupolar nucleus and the first order quadrupolar interaction is dominantly broadens the powder patterns for the ^2H spectrum.

Like CO_2 dynamic, ^2H spectra can also be calculated by EXPRESS, where the rotation types and motion rates also contribute to the line shape.⁹⁴ As shown in **Figure 1-29**, with different motion types, the motion rates decide the broadness and the shape of the powder patterns. Usually, the slow ($< 10^3$ Hz), intermediate ($10^3 < \text{rate} < 10^7$ Hz), and fast regimes ($\text{rate} > 10^7$ Hz) are used to differentiate how rapid the nuclear reorientation is.

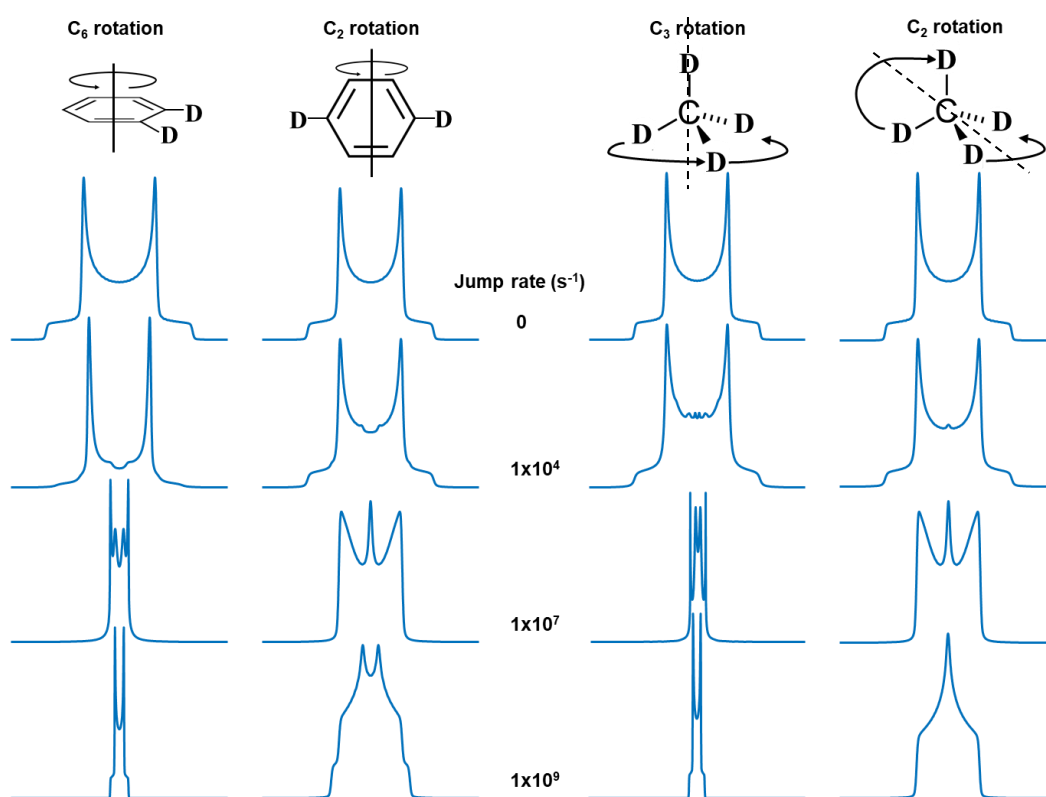


Figure 1-29 ^2H SSNMR simulation spectra of C_6D_6 (left) and CD_4 (right) with changing motion rates under different motion types.

1.9 Outline of the thesis

The main objectives of this thesis are to systematically study the MOFs based on s-block metals, as they are giving many potential applications but are not investigated as much as the MOFs based on transition metals.

In this thesis, totally five chapters are included. General introduction about the MOFs, especially s-block metal-based, and the background of solid-state NMR are given in chapter 1 and chapter 2 respectively.

The MOFs with combination of s-block metals and V-shaped SDB ligands will be discussed as the first part of the experiment. Six s-block metal-based MOFs with SDB ligands were chosen (three alkali metals: Li, Na and Cs; three alkali earth metals: Mg, Ca and Sr).⁶⁴⁻⁶⁷ Beginning with the systematic study on the structures of six s-block metal-based MOFs with SDB linker, particular attention will be paid to the coordination environments around metal centers by using solid-state nuclear magnetic resonance (SSNMR) in chapter 3. Additionally, followed by study on the properties of the porous channel, the motions of CO₂ inside the framework in four activated porous SDB MOFs (Na₂SDB, Mg₃(OH)₂(SDB)₂, CaSDB and SrSDB) at various temperatures will be examined by using variable-temperature (VT) static ¹³C SSNMR with further analytical and dynamical simulations of the spectra in chapter 4.

Chapter 5 mainly focuses on the squarate ligands, where the dynamics of guest molecules within UTSA-280 and Zn(bipy)(C₄O₄)(H₂O)₂ under various temperatures will be investigated,^{68,69} including H₂, C₂H₂ and CO₂. The structures of UTSA-280 and Zn(bipy)(C₄O₄)(H₂O)₂ will also be explored, especially on the coordinated water molecules within frameworks, with static ²H SSNMR employed.

1.10 Reference

1. H. Li, M. Eddaoudi, M. O'Keeffe & O. Yaghi. Design and synthesis of an exceptionally stable and highly porous metal-organic framework. *Nature*, 1999, **402**, 276-279.
2. K. Wada, K. Sakaushi, S. Sasaki and H. Nishihara, Multielectron-Transfer-based Rechargeable Energy Storage of Two-Dimensional Coordination Frameworks with Non-Innocent Ligands, *Angew. Chem., Int. Ed.*, 2018, **57**, 8886–8890
3. J. Long & O. Yaghi. Reviewing the latest developments across the interdisciplinary area of metal–organic frameworks from an academic and industrial perspective. *Chem. Soc. Rev.*, 2009, **38**, 1213–1214.
4. M. Alnaqbi, A. Alzamly, S. Ahmed, M. Bakiro, J. Kegere & H. Nguuyen. Chemistry and

-
- applications of s-block metal organic frameworks. *J. Mater. Chem. A*, 2021, **9**, 3828–3854.
5. C. Janiak & J. K. Vieth. MOFs, MILs and more: concepts, properties and applications for porous coordination networks (PCNs). *New J. Chem.*, 2010, **34**, 2366
 6. B. Li, H.M. Wen, W. Zhou & B.L. Chen. Porous Metal–Organic Frameworks for Gas Storage and Separation: What, How, and Why? *J. Phys. Chem. Lett.*, 2014, **5**, 3468-3479.
 7. D.J. Babu, G.W. He, L.F. Villalobos & K.V. Agrawal, Crystal Engineering of Metal–Organic Framework Thin Films for Gas Separations. *ACS Sustain. Chem. Eng.*, 2019, **7**, 49-69
 8. W. Li, J. Qian, T. Zhao, Y. Ye, Y. Xing, Y. Huang, L. Wei, N. Zhang, N. Chen, L. Li, F. Wu & R. Chen. Boosting High-Rate Li–S Batteries by an MOF-Derived Catalytic Electrode with a Layer-by-Layer Structure. *Advanced Science*. 2019, **6(16)**, 1802362.
 9. K. Wang, B. Lv, Z. Wang, H. Wu, J. Xu & Q. Zhang. Two-Fold Interpenetrated Mn-Based Metal-Organic Frameworks (MOFs) as Battery-Type Electrode Materials for Charge Storage. *Dalton transactions : an international journal of inorganic chemistry*. 2020, **49(2)**, 411-417
 10. L. Jiao, Y. Wang, H.-L. Jiang & Q. Xu, Metal–Organic Frameworks as Platforms for Catalytic Applications. *Adv. Mater.*, 2018, **30**, 1703663.
 11. D. Chen, W. Shen, S. Wu, C. Chen, X. Luo & L. Guo. Ion Exchange Induced Removal of Pb(II) by MOF-Derived Magnetic Inorganic Sorbents. *Nanoscale*, 2016, **8(13)**, 7172-7179.
 12. S. Mallakpoura, E. Nikkhoob & C. Hussainc. Application of MOF materials as drug delivery systems for cancer therapy and dermal treatment. *Coordination Chemistry Reviews*. 2022, **451**, 214262.
 13. V. V. Butova, M. A. Soldatov, A. A. Guda, K. A. Lomachenko & C. Lamberti. Metal Organic Frameworks: Structure, Properties, Methods of Synthesis and Characterization. *Russian Chemical Reviews*. 2016, **85 (3)**, 280–307.
 14. A. Y. Tsivadze, O. E. Aksyutin, A. G. Ishkov, M. K. Knyazeva, O. V. Solovtsova, I. E. Men'shchikov, A. A. Fomkin, A. V. Shkolin, E. V. Khozina & V. A. Grachev. Metal-Organic Framework Structures: Adsorbents for Natural Gas Storage. *Russian Chemical Reviews*. 2019, **88 (9)**, 925–978.

-
15. Z. Zhang, Z. Yao, S. Xiang & B. Chen. Perspective of Microporous Metal–Organic Frameworks for CO₂ Capture and Separation. *Energy & Environmental Science*. 2014, **7** (9), 2868–29.
 16. A. Torrisi, R. G. Bell & C. Mellot-Draznieks. Functionalized MOFs for Enhanced CO₂ Capture. *Crystal Growth & Design*. 2010, **10** (7), 2839–2841.
 17. N. A. Khan & S. H. Jung. Phase-Transition and Phase-Selective Synthesis of Porous Chromium-Benzenedicarboxylates. *Crystal Growth & Design*. 2010, **10** (4), 1860–1865.
 18. D. Banerjee, H. Wang, B. J. Deibert & J. Li. Alkaline Earth Metal-Based Metal–Organic Frameworks: Synthesis, Properties, and Applications. S. Kaskel (Ed.). 2016.
 19. D. Banerjee & J. B. Parise. Recent Advances in s-Block Metal Carboxylate Networks. *Cryst. Growth Des.* 2011, **11**, 4704–4720.
 20. Y. Zang, L. Li & S. Zang. Recent development on the alkaline earth MOFs (AEMOFs). *Coord. Chem. Rev.* 2021, **440**. 213955.
 21. M. Liu, Y. Feng, Y. Wang, Y. Yu, L. Sun & X. Zhang. Conformational flexibility Tuned positive thermal expansion in Li-based 3D metal–organic framework. *Inorganic Chemistry Communications*. 2019, **105**, 247–252.
 22. D. Chen, J. Tian & C. Liu. A luminescent Li(I)-based metal–organic framework showing selective Fe(III) ion and nitro explosive sensing. *Inorganic Chemistry Communications*. 2016, **68**, 29–32.
 23. D. Pugh, E. Ashworth, K. Robertson, L. Delmas, A. White, P. Horton, G. Tizzard, P. Lickiss & R. Davies. Metal–Organic Frameworks Constructed from Group 1 Metals (Li, Na) and Silicon-Centered Linkers. *Crystal Growth & Design*, 2019, **19** (1), 487–497.
 24. C. Li, K. Wang, J. Li & Q. Zhang. Nanostructured potassium–organic framework as an effective anode for potassium-ion batteries with a long cycle life. *Nanoscale*, 2020, **12**, 7870.
 25. S. J. Manuel, S. S. Eider, C. Javier, B. Blanca, S. C. Alfonso, F. Belen, M. Diego, B. Marco, G. R. Santiago, L. Florin, R. Almudena & R. D. Antonio. A Potassium Metal–Organic Framework based on Perylene-3,4,9,10-tetracarboxylate as Sensing Layer for Humidity Actuators. *Scientific Reports*, 2018, **8**(1), 14414–10.

-
26. R. S. Forgan, R. A. Smaldone, J. J. Gassensmith, H. Furukawa, D. B. Cordes, Q. Li, C. E. Wilmer, Y. Y. Botros, R. Q. Snurr, A. M. Z. Slawin & J. F. Stoddart. Nanoporous Carbohydrate Metal–Organic Frameworks. *J. Am. Chem. Soc.* 2012, **134(1)**, 406–417.
27. Y. Zang, L. Li & S. Zang. Recent development on the alkaline earth MOFs (AEMOFs). *Coordination Chemistry Reviews*, 2021, **440**, 213955.
28. S. Kenji, H. Matthew, H. Satoshi, D. Anne & L. Jefferey. Synthesis and Hydrogen Storage Properties of $\text{Be}_{12}(\text{OH})_{12}(1,3,5\text{-benzenetribenzoate})_4$. *American Chemical Society*. 2009, **131(42)**, 15120-15121.
29. M. Kang, D. Luo, Z. Lin, G. Thiele & S. Dehnen. Crystalline beryllium carboxylate frameworks containing inorganic chains of BeO_4 tetrahedra. *CrystEngComm*, 2013, **15**, 1845–1848.
30. A. Mallick, S. Saha, P. Pachfule, S. Roy & R. Banerjee. Selective CO_2 and H_2 adsorption in a chiral magnesium-based metal organic framework (Mg-MOF) with open metal sites. *J. Mater. Chem.*, 2010, **20**, 9073–9080.
31. L. J. Hyung, N. T. Binh, N. D. Khoi, K. J. Young, P. B. Thang & K. S. Sub. Gas Sensing Properties of Mg-Incorporated Metal-Organic Frameworks. *Sensors*. 2019, **19**, 3323.
32. P. Liang, H. Liu, C. Yeh, C. Lin & V. Zima. Supramolecular Assembly of Calcium Metal–Organic Frameworks with Structural Transformations. *Cryst. Growth Des.* 2011, **11(3)**, 699–708.
33. M. C. Das, S.K. Ghosh, E. C. Sanudo & P. K. Bharadwaj. Coordination polymers with pyridine-2,4,6-tricarboxylic acid and alkaline-earth/lanthanide/transition metals: synthesis and X-ray structures. *Dalton Trans.*, 2009, 1644–1658.
34. P. William, W. Antek, D. Anne & M. Adam. Beryllium benzene dicarboxylate: the first beryllium microporous coordination polymer. *J. Mater. Chem.*, 2009, **19**, 6489–6491.
35. D. Mircea & L. Jeffrey. Strong H_2 Binding and Selective Gas Adsorption within the Microporous Coordination Solid $\text{Mg}_3(\text{O}_2\text{C-C}_{10}\text{H}_6\text{-CO}_2)_3$. *J. AM. CHEM. SOC.* 2005, **127**, 9376-9377.
36. G. Glover, P. Gregory, S. Bryan, B. David & Y. Omar. MOF-74 building unit has a direct impact on toxic gas adsorption. *Chemical Engineering Science*. 2011, **66**, 163–170.

-
37. S. Debraj, M. Tanmoy, S. Rupam & K. Subratanath. Heterogeneous catalysis over a barium carboxylate framework compound: Synthesis, X-ray crystal structure and aldol condensation reaction. *Polyhedron*. 2012, **43**, 63–70.
38. M. Tanmoy, S. Debraj, D. Soma & K. Subratanath. Barium Carboxylate Metal-Organic Framework - Synthesis, X-ray Crystal Structure, Photoluminescence and Catalytic Study. *Eur. J. Inorg. Chem.* 2012, 4914–4920.
39. S. Debraj, M. Tanmoy & K. Subratanath. Alkaline earth metal-based metal-organic framework: hydrothermal synthesis, X-ray structure and heterogeneously catalyzed Claisen-Schmidt reaction. *Dalton Trans.*, 2014, **43**, 13006–13017.
40. K. Ajay, A. Mohamad & A. Rafael. PLLA-ZIF-8 metal organic framework composites for potential use in food applications: Production, characterization and migration studies. *Packag Technol Sci.* 2021, **34**, 393–400.
41. P. Lightfoot & A. Snedden. Metal–organic co-ordination frameworks based on mixed N- and O-donor ligands: crystal structures of [Co(phth)₂(bipy)] and [Co₂(mal)₂(bipy)(H₂O)₂]. *J. Chem. Soc., Dalton Trans.*, 1999, 3549-3551.
42. R. Ye, X. Zhang, J. Zhai, Y. Qin, L. Zhang, Y. Yao & J. Zhang. N-donor ligands enhancing luminescence properties of seven Zn/Cd(ii) MOFs based on a large rigid π -conjugated carboxylate ligand. *CrystEngComm*, 2015, **17**, 9155-9166
43. A. Desai, S. Sharma, S. Let & S. Ghosh. N-donor linker-based metal-organic frameworks (MOFs): Advancement and prospects as functional materials. *Coordination Chemistry Reviews*. 2019, **395**, 146-192.
44. J. M. Moreno, A. Velyt & U. Diaz. Expandable Layered Hybrid Materials Based on Individual 1D Metalorganic Nanoribbons. *Materials*, 2019, **12**, 1953.
45. C. Song, J. Jiao, Q. Lin, H. Liu & Y. He. C₂H₂ adsorption in three isostructural metal–organic frameworks: boosting C₂H₂ uptake by rational arrangement of nitrogen sites. *Dalton Trans.*, 2016, **45**, 4563–4569.
46. Y. Zhang, S. Yang, X. Chang, H. Guo, Y. Li, M. Wang, W. Li, L. Jiao & Y. Wang. MOF based on a longer linear ligand: electrochemical performance, reaction kinetics, and use as a novel anode material for sodium-ion batteries. *Chem. Commun.*, 2018, **54**, 11793—11796.

-
47. Y. Wang, M. He, X. Gao, Y. Zhang, H. Zhong, P. Long, X. Wang & Y. He. Two NbO-type MOFs based on linear and zigzag diisophthalate ligands: exploring the effect of ligand-originated MOF isomerization on gas adsorption properties. *Inorg. Chem. Front.*, 2018, **5**, 2811–2817.
48. J. Hu, X. Huang, C. Pan & L. Zhang. Photochemical and Magnetic Properties of Seven New Metal–Organic Frameworks Constructed by Flexible Tetrapyridines and V-Shaped Polycarboxylate Acids. *Cryst. Growth Des.* 2015, **15** (5), 2272–2281.
49. W. Song, L. Liang, X. Cui, X. Wang, E. Yang & X. Zhao. Assembly of Zn-coordination polymers constructed from benzothiadiazole functionalized bipyridines and V-shaped dicarboxylic acids: topology variety, photochemical and visible-light-driven photocatalytic properties. *CrystEngComm*, 2018, **20**, 668–678.
50. H. Wang, D. Zhang, D. Sun, Y. Chen, K. Wang, Z. Wang, Z. Ni, L. Tian & J. Jiang. Diverse Ni(ii) MOFs constructed from asymmetric semi-rigid V-shaped multicarboxylate ligands: structures and magnetic properties. *CrystEngComm*, 2010, **12**, 1096–1102.
51. W. Huang, L. Hou, B. Liu, L. Cui, Y. Wang & Q. Shi. Two novel interpenetrating MOFs constructed from a derivative of phenanthroline and a V-shaped flexible dicarboxylate ligand contains unique chiral structure. *Inorganica Chimica Acta*, 2012, **382**, 13–18.
52. L. Han, W. Yan, S. Chen, Z. Shi & H. Zheng. Exploring the Detection of Metal Ions by Tailoring the Coordination Mode of V-Shaped Thienylpyridyl Ligand in Three MOFs. *Inorg. Chem.*, 2017, **56**, 2936–2940.
53. F. Lian, D. Yuan, F. Jiang & M. Hong. 4,4'-Sulfonyldibenzoic acid. *Acta Crystallographica Section E: Structure Reports Online*, 2007, **63**, 2870.
54. D. Banerjee, Z. Zhang, A. Plonka, J. Li & J.B. Parise. A Calcium Coordination Framework Having Permanent Porosity and High CO₂/N₂ Selectivity. *Cryst. Growth Des.* 2012, **12**, 2162–2165
55. C. Yeh, W. Lin, S. Lo, C. Kao, C. Lin & C. Yang. Microwave Synthesis and Gas Sorption of Calcium and Strontium Metal–Organic Frameworks with High Thermal Stability, *CrystEngComm* 2012, **14**, 1219–1222
56. D. Senthil Raja, J. Luo, C. Wu, Y. Cheng, C. Yeh, Y. Chen, S. Lo, Y. Lai & C. Lin.

-
- Solvothermal Synthesis, Structural Diversity, and Properties of Alkali Metal–Organic Frameworks Based on V-Shaped Ligand *Cryst. Growth Des.* 2013, **13**, 3785–3793
57. S. Chen, B. Lucier, P. Boyle & Y. Huang. Understanding the fascinating origins of CO₂ adsorption and dynamics in MOFs. *Chem. Mater.* 2016, **28(16)**, 5829-5846.
58. D. Banerjee, L. Borkowski, S. Kim & J. Parise. Synthesis and Structural Characterization of Lithium-Based Metal-Organic Frameworks. *Crystal Growth & Design*, 2009, **9(11)**, 4922-4926.
59. D. Raja, J. Luo, C. Wu, Y. Cheng, C. Yeh, Y. Chen, S. Lo, Y. Lai & C. Lin. Solvothermal Synthesis, Structural Diversity, and Properties of Alkali Metal–Organic Frameworks Based on V-shaped Ligand. *Cryst. Growth Des.* 2013, **13**, 3785–3793.
60. C. Wu, D. Raja, C. Yang, C. Yeh, Y. Chen, C. Li, B. Ko & C. Lin. Evaluation of structural transformation in 2D metal–organic frameworks based on a 4,4'-sulfonyldibenzoate linker: microwave-assisted solvothermal synthesis, characterization and applications. *CrystEngComm*, 2014, **16**, 9308.
61. T. Kundu, S. Sahoo & R. Banerjee. Alkali earth metal (Ca, Sr, Ba) based thermostable metal–organic frameworks (MOFs) for proton conduction. *Chem. Commun.*, 2012, **48**, 4998–5000.
62. R. Lin, L. Li, A. Alsalmeh & B. Chen. An Ultramicroporous Metal-Organic Framework for Sieving Separation of Carbon Dioxide from Methane. *Small structures*, 2020, **1(3)**.
63. R. Lin, L. Li, H. Zhou, H. Wu, C. He, S. Li, R. Krishna, J. Li, W. Zhou & B. Chen. Molecular sieving of ethylene from ethane using a rigid metal–organic framework. *Nature Materials*, 2018, **17**, 1128-1133.
64. D. Banerjee, L. Borkowski, S. Kim & J. Parise. Synthesis and Structural Characterization of Lithium-Based Metal-Organic Frameworks. *Crystal Growth & Design*, 2009, **9(11)**, 4922-4926.
65. D. Raja, J. Luo, C. Wu, Y. Cheng, C. Yeh, Y. Chen, S. Lo, Y. Lai & C. Lin. Solvothermal Synthesis, Structural Diversity, and Properties of Alkali Metal–Organic Frameworks Based on V-shaped Ligand. *Cryst. Growth Des.* 2013, **13**, 3785–3793.
66. C. Wu, D. Raja, C. Yang, C. Yeh, Y. Chen, C. Li, B. Ko & C. Lin. Evaluation of structural

-
- transformation in 2D metal–organic frameworks based on a 4,4'-sulfonyldibenzoate linker: microwave-assisted solvothermal synthesis, characterization and applications. *CrystEngComm*, 2014, **16**, 9308.
67. T. Kundu, S. Sahoo & R. Banerjee. Alkali earth metal (Ca, Sr, Ba) based thermostable metal–organic frameworks (MOFs) for proton conduction. *Chem. Commun.*, 2012, **48**, 4998–5000.
68. L. Li, L. Guo, S. Pu, J. Wang, Q. Yang, Z. Zhang, Y. Yang, Q. Ren, S. Alnemrat & Z. Bao. A calcium-based microporous metal-organic framework for efficient adsorption separation of light hydrocarbons. *Chemical Engineering Journal*. 2019, **358**, 446-455.
69. C. Wang, S. Ke, Y. Hsieh, S. Huang, T. Wang, G. Lee & Y. Chuang. Water de/adsorption associated with single-crystal-to-single-crystal structural transformation of a series of two-dimensional metal–organic frameworks, $[M(\text{bipy})(\text{C}_4\text{O}_4)(\text{H}_2\text{O})_2]3\text{H}_2\text{O}$ ($M = \text{Mn}(1), \text{Fe}(2),$ and $\text{Zn}(3)$, and $\text{bipy}=4,4\text{-bipyridine}$). *J Chin Chem Soc.* 2019, **66**, 1031–1040.
70. H. Hoffmann, M. Debowski, P. Müller, S. Paasch, I. Senkovska, S. Kaskel & E. Brunner. Solid-state NMR Spectroscopy of Metal–Organic Framework Compounds(MOFs). *Materials*, 2012, **5**, 2537.
71. M. H. Levitt. *Spin Dynamics*. Second ed., John Wiley & Sons West Sussex, 2008
72. M. J. Duer. *Solid-State NMR Spectroscopy: Principles and Applications*. Blackwell Science, Oxford, 2002.
73. K. MacKenzie & M. E. Smith. *Multinuclear Solid-State Nuclear Magnetic Resonance of Inorganic Materials*. Pergamon: Oxford New York, 2002.
74. M. H. Levitt. *Spin Dynamics Basics of Nuclear Magnetic Resonance*; John Wiley & Sons Ltd: West Sussex, England, 2007.
75. J. Keeler, *Understanding NMR Spectroscopy*. Second ed., John Wiley & Sons, West Sussex, 2010
76. T. Abbott, G. Buchanan, P. Kruus & K. Lee. ^{13}C nuclear magnetic resonance and Raman investigations of aqueous carbon dioxide systems. *Canadian Journal of Chemistry*. 1982, **60(8)**, 1000-1006.
77. A. J. Beeler, A. M. Orendt, D. M. Grant, P. W. Cutts, J. Michl, K. W. Zilm, J. W. Downing,

-
- J. C. Facelli, M. S. Schindler & W. Kutzelnigg. Low-Temperature Carbon-13 Magnetic Resonance in Solids. 3. Linear and Pseudolinear Molecules. *Journal of the American Chemical Society*, 1984, **106 (25)**, 7672-7676.
78. R. K. Harris, E. D. Becker, S. M. De Menezes, P. Granger, R. E. Hoffman & K. W. Zilm. Further conventions for NMR shielding and chemical shifts. *Pure Appl. Chem.*, 2008, **80**, 59-84.
79. Y. Lu,. Dynamic studies of guest molecules in Metal- Organic Frameworks using Solid-State NMR. 2015, **16**
80. G. E. Pake. Nuclear Resonance Absorption in Hydrated Crystals: Fine Structure of the Proton Line. *The Journal of Chemical Physics*. 1948, **16 (4)**, 327-336.
81. J. Brus, S. Abbrent, L. Kobera, M. Urbanova & P. Cuba. Chapter Two - Advances in ²⁷Al MAS NMR Studies of Geopolymers. *Annual report on NMR spectroscopy*. 2016, **88**, 79-147.
82. D. C. Apperley, P. Hodgkinson & R. K. Harris. *Solid-State NMR : Basic Principles and Practice*. Momentum Press; 2012.
83. J. Klinowski. NMR of Solids. *Encyclopedia of Spectroscopy and Spectrometry*, 1999, 1537-1544
84. K. T. Mueller, B. Q. Sun, G. C. Chingas, J. W. Zwanziger, T. Terao & A. Pines. Dynamic-angle spinning of quadrupolar nuclei, *Journal of Magnetic Resonance*, 1990, **86(3)**, 470-487.
85. J. E. Tanner, E. O. Stejskal. *The Journal of Chemical Physics*. 1968, **49**, 1768.
86. E. L. Hahn. Spin Echoes, *Phys. Rev.* 1950, **80**, 580.
87. S. R. Hartmann & E. L. Hahn. *Physical Review*. 1962, **128**, 2042.
88. A. Medek, J. Harwood & L. Frydman. Multiple-Quantum Magic-Angle Spinning NMR: A New Method for the Study of Quadrupolar Nuclei in Solids. *J. Am. Chem. Soc.* 1995, **117(51)**, 12779–12787.
89. R. Hajjar, Y. Millot & P. P. Man. Phase cycling in MQMAS sequences for half-integer quadrupole spins. *Progress in Nuclear Magnetic Resonance Spectroscopy*. 2010, **57**, 306–342.

-
90. R. Knitsch, M. Brinkkötter, T. Wiegand, G. Kehr, G. Erker, M. R. Hansen, H. Eckert. Solid-State NMR Techniques for the Structural Characterization of Cyclic Aggregates Based on Borane–Phosphane Frustrated Lewis Pairs. *Molecules*. **2020**, *25(6)*, 1400.
91. K. Eichele, R. E. Wasylshen. WSolids1, University of Tübingen, Tübingen, Germany, 2009.
92. R. L. Vold, & G. L. Hoatson. Effects of Jump Dynamics on Solid State Nuclear Magnetic Resonance Line Shapes and Spin Relaxation Times. *Journal of Magnetic Resonance*, 2009, **198 (1)**, 57-72.
93. V. J. Witherspoon, J. Xu & J. A. Reimer. Solid-State NMR Investigations of Carbon Dioxide Gas in Metal–Organic Frameworks: Insights into Molecular Motion and Adsorptive Behavior. *Chem. Rev.* 2018, **118**, 10033–10048.
94. L. O’Dell & C. Ratcliffe. Quadrupolar NMR to Investigate Dynamics in Solid Materials. 2011

Chapter 2

2. Investigating the coordination environments using MAS SSNMR

2.1 Introduction

2.1.1 Alkali metal center MOFs: M_2SDB ($M=Li, Na$ and Cs)

Li_2SDB (Figure 2-1) is also named ULMOF-3 since lithium is the lightest metal (UL = ultralight; SDB = sulfonyldibenzoate).¹ The 1D chain is formed by the corner-sharing LiO_4 (highlighted with the purple Li clusters along a-axis). With bridging SDB ligands connected among 1D chain, a nonporous 3D structure is formed with space group: $P2_1/n$. Li_2SDB contains two distinguished Lithium centers: Li(1) is tetrahedrally coordinated with three oxygen atoms (O(1), O(2) and O(3)) from three carboxylic groups belonging to three SDB ligands and one oxygen atom (O(4)) from sulfonyl group in another SDB ligand; Li(2) is tetrahedrally attached with four oxygen atoms (O(1), O(2), O(3) and O(5)) from four carboxylic groups belonging to four independent SDB ligands. The average distance between the phenyl rings of each identical layer is 5.5 Å along the a-axis and the distance between two identical phenyl rings is 10.32 Å along the c-axis.

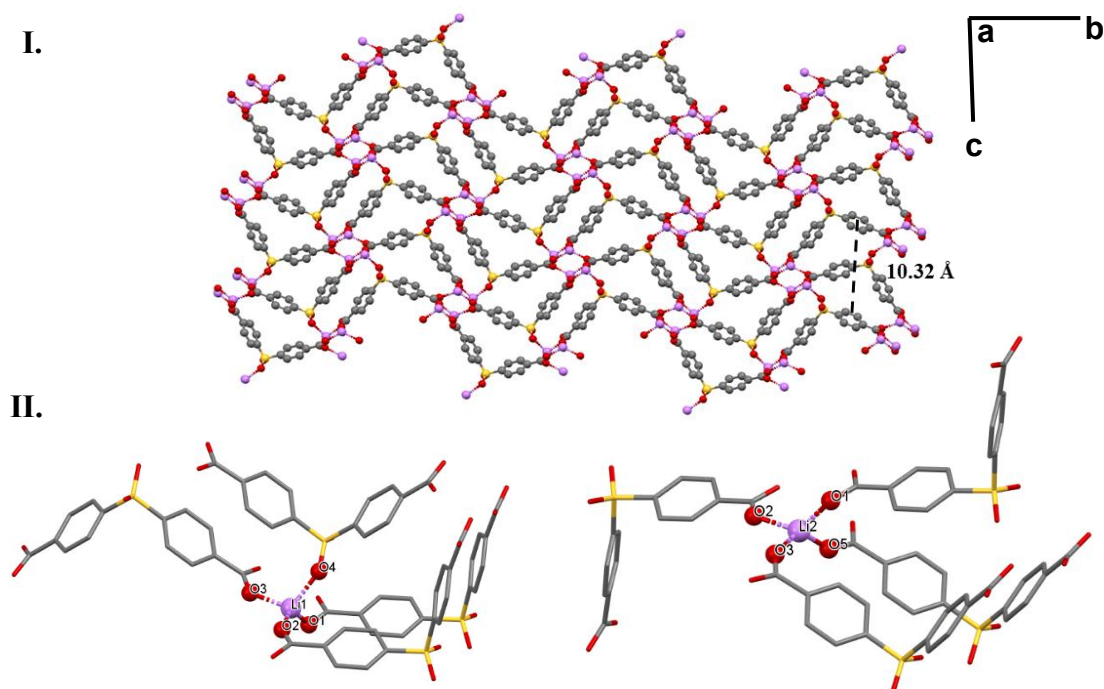


Figure 2-1 (I). 3D framework of Li_2SDB . (II). The local coordination geometries of the central Li(1) and Li(2) atoms. (All H atoms are omitted for clarity)

Na₂SDB (**Figure 2-2**) has a 1D chain formed by corner-sharing NaO₆ with bridging SDB ligands connection among Na sites. A 3D porous structure (space group: P-1) was generated with two types of channels,² where the solvent-accessible channel volume is 11.4 × 13.9 Å², while the volume of the channel that adsorbs the guest molecule is 7.6 × 9.8 Å² (The distance between benzene ring centers with van der Waals considered). Na₂SDB contains two distinguished Na atoms. Na(1) is six-coordinated with one oxygen atom (O(5)) from a sulfonyl group in one SDB ligand, three oxygen atoms (O(3) and two O(4)) from three inequivalent carboxylic groups belonging to other three SDB ligands and two independent oxygen atoms (O(1) and O(2)) from single carboxylic groups in another SDB ligand. Na(2) is five-coordinated with one sulfonyl group oxygen atom (O(6)) from one SDB ligand and four oxygen atoms (O(1), O(2), O(3) and O(4)) from four carboxylic groups belonging to other four SDB ligands. The CO₂ adsorption capacity is 1.73/1.33 mmol/g at 273/298 K under 1 atm, and no methane gas sorption ability is shown at 298 K under 1 atm.

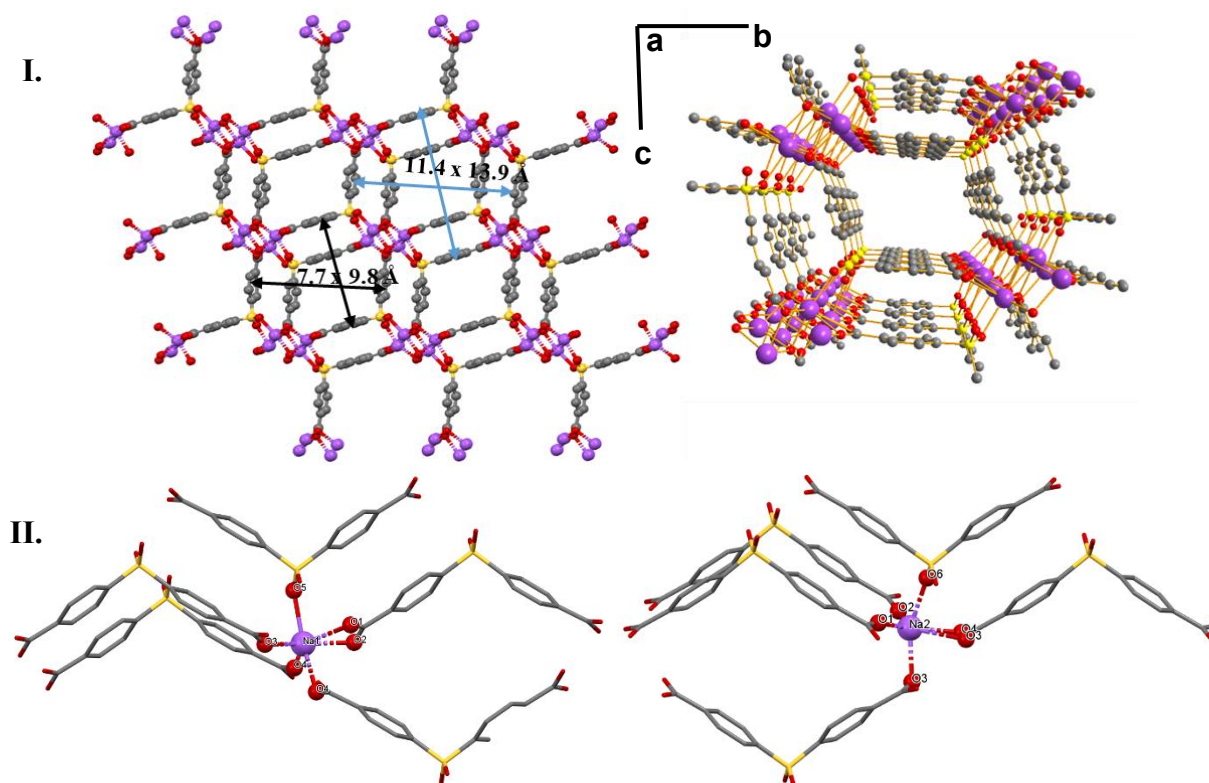


Figure 2-2 (I). 3D framework of Na₂SDB. (II). The local coordination geometries of the central Na(1) and Na(2) atoms. (All H atoms are omitted for clarity)

Cs_2SDB (**Figure 2-3**) has the 1D chains that are formed by the corner-shared and edged-shared motifs CsO_9 . Further bridged by SDB ligands among Cs sites, a 3D porous structure was generated.² Similar to Na_2SDB , Cs_2SDB has the space group of P-1 and contains two types of channels where the solvent-accessible channel volume is $12.5 \times 15.4 \text{ \AA}^2$, while the volume of the channel that adsorbs the molecule is $9.1 \times 11.4 \text{ \AA}^2$. The asymmetry unit of Cs_2SDB contains only one Cs atom: two oxygen atoms (O(1) and O(2)) from two sulfonyl groups belonging to two independent SDB ligands, five oxygen atoms (two O(3), O(4), O(5) and O(6)) from five carboxylic groups belonging to other five SDB ligands and two oxygen atoms (two O(7)) from coordinated water molecules.

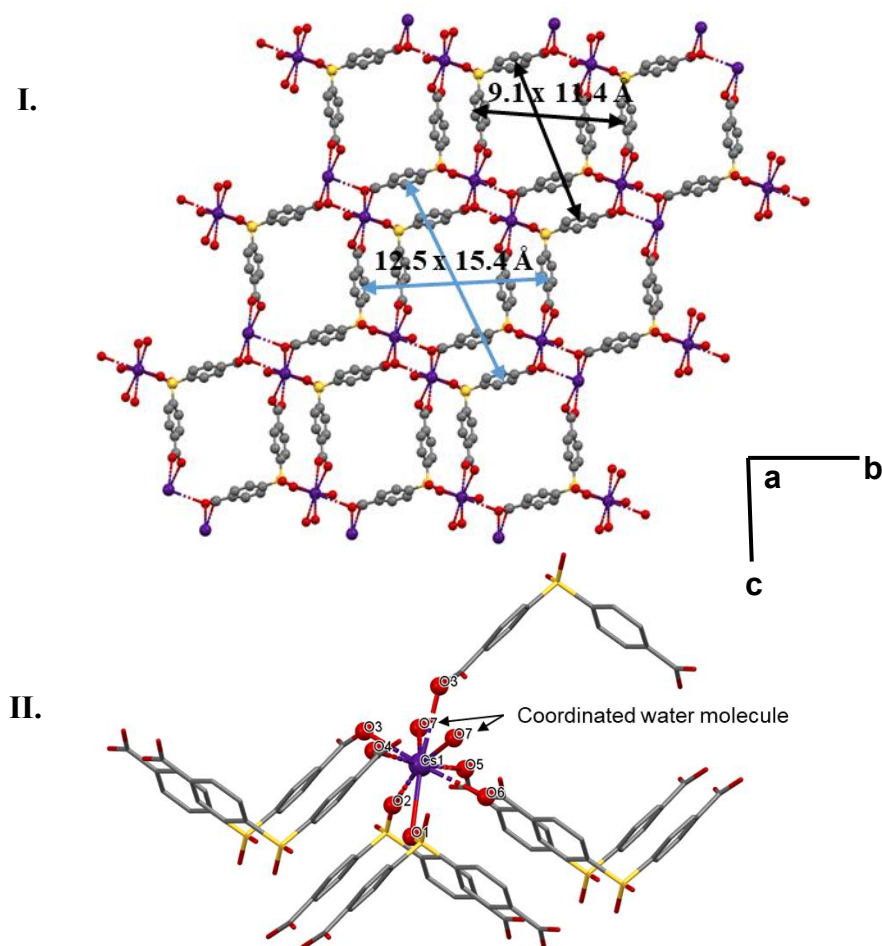


Figure 2-3 (I). 3D framework of Cs_2SDB . (II). The local coordination geometries of the central Cs(1) and Cs(2) atoms. (All H atoms are omitted for clarity)

2.1.2 Alkaline earth metal center MOFs: MSDB (M=Mg, Ca and Sr)

$\text{Mg}_3(\text{OH})_2(\text{SDB})_2(\text{EtOH})(\text{H}_2\text{O})_3$ (as-made MgSDB)(Figure 2-4) has a 2D layer structure (space group: P2/c) with porous channels.³ $[\text{Mg}_3(\mu_3\text{-OH})_2]_n$ chains along the a-axis, where $\text{Mg}(1)\text{O}_6$ and $\text{Mg}(3)\text{O}_6$ octahedra are edge-sharing and they are apex-shared with the $\text{Mg}(2)\text{O}_6$ octahedra, are linked by SDB ligands, extending to the layered structure within the ab-plane. Each layer contains rhomboidal channels with $5.2 \times 4.7 \text{ \AA}^2$. The layers are further connected by the hydrogen bonds between the coordinated water molecules and oxygen atoms on the sulfonyl group. Three different Mg sites are all connected to the same oxygen atoms (O(1) and O(2)). Mg(1) coordinates with two oxygen atoms (O(4) and O(5)) from two carboxylic groups belonging to two SDB ligands, two oxygen atoms (O(1) and O(2)) from the bridging OH groups which connects to Mg(2) and Mg(3) as well, and two oxygen atoms (O(3) and O(6)) from two coordinated water molecules; Mg(2) has four coordinated oxygen atoms (O(7), O(8), O(9) and O(10)) from four different carboxylic groups belonging to four independent SDB ligands and two oxygen atoms (O(1) and O(2)) that shares among three Mg centers; Mg(3) coordinates with two oxygen atoms (O(11) and O(12)) from two carboxylic groups belonging to two SDB ligands, two oxygen atoms (O(1) and O(2)) sharing with Mg(1) and Mg(2), one oxygen atom (O(13)) from coordinated water molecule and one oxygen atom (O(14)) from coordinated ethanol molecule.

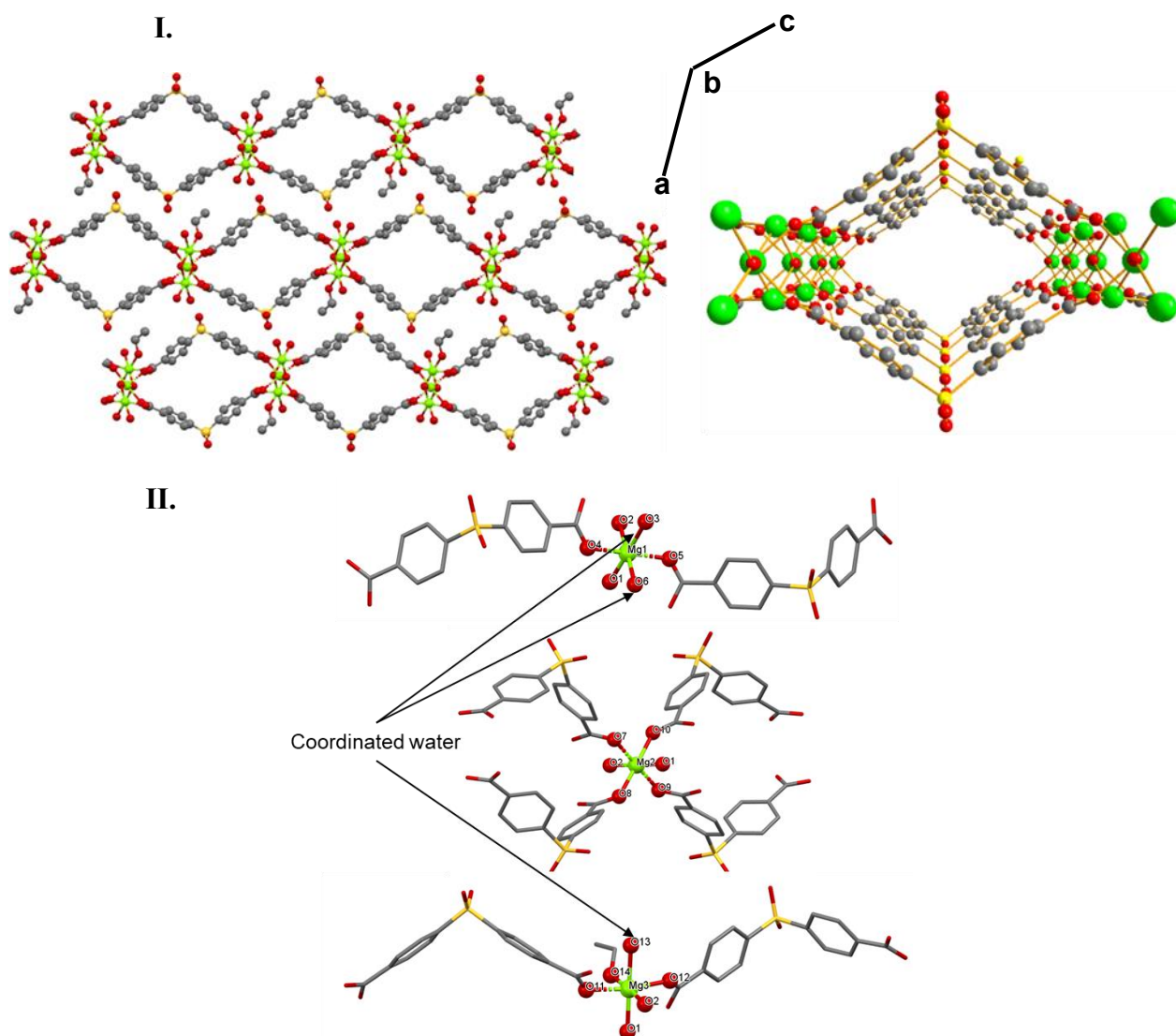


Figure 2-4 (I). 3D framework of $\text{Mg}_3(\text{OH})_2(\text{SDB})_2(\text{EtOH})(\text{H}_2\text{O})_3$. (II). The local coordination geometries of the central Mg(1), Mg(2) and Mg(3) atoms. (All H atoms are omitted for clarity)

$\text{Mg}_3(\text{OH})_2(\text{SDB})_2$ (activated MgSDB)(**Figure 2-5**) is obtained after activation at a high temperature, usually 200 °C. The MOF will transfer into its de-solvated phase with space group of $P2_1/n$. The layer structure is retained with $[\text{Mg}_3(\mu_3\text{-OH})_2]_n$ chains along the a-axis connected by the SDB ligands, and the layers are also connected by the hydrogen bonds between the bridging OH group and oxygen atoms on the sulfonyl group. Mg(1) centers is still 6-coordinated with four oxygen atoms (two O(2) and two O(3)) from four carboxylic groups belonging to four SDB ligands and two oxygen atoms (two O(7)) from two bridging OH groups. While Mg(1) and Mg(3) from $\text{Mg}_3(\text{OH})_2(\text{SDB})_2(\text{EtOH})(\text{H}_2\text{O})_3$ lose coordinated water and

ethanol, resulting in two equivalent Mg ion centers, named as Mg(2) in $\text{Mg}_3(\text{OH})_2(\text{SDB})_2$. Mg(2) is tetrahedrally coordinated with two oxygen atoms (O(1) and O(4)) from two carboxylic groups belonging to two independent SDB ligands and two O(7) atoms from two bridging OH groups. $\text{Mg}_3(\text{OH})_2(\text{SDB})_2$ has larger rhomboidal channels compared with $\text{Mg}_3(\text{OH})_2(\text{SDB})_2(\text{EtOH})(\text{H}_2\text{O})_3$ and can adsorb 1.72/1.13 mmol/g at 273/298 K under 1 atm.

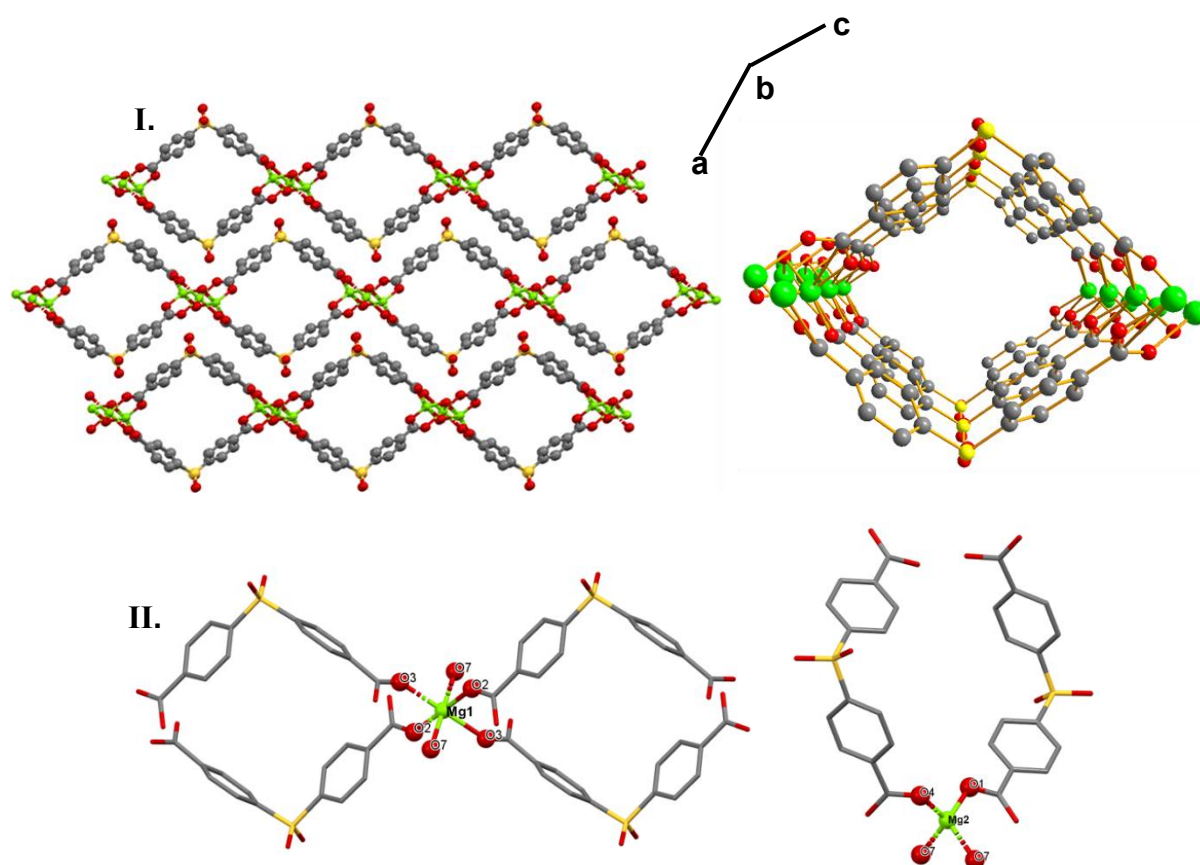


Figure 2-5 (I). 3D framework of $\text{Mg}_3(\text{OH})_2(\text{SDB})_2$. (II). The local coordination geometries of the central Mg(1) and Mg(2) atoms. (All H atoms are omitted for clarity)

CaSDB and SrSDB (**Figure 2-6**) are sharing the same coordination modes and extended 3D frameworks with both space group of $P2_1/n$, including channels with approximately $8.5 \times 8.4 \text{ \AA}^2$ for CaSDB and $8.8 \times 8.7 \text{ \AA}^2$ for SrSDB.⁴ Triangular edge-sharing CaO_7 or SrO_7 trigonal prism form zigzag 1D chains, further connected by μ_6 -SDB ligands. The asymmetric unit contains only one Ca or Sr atom, which is six-coordinated: five oxygen atoms (two O(1), O(2),

O(3) and O(4)) from five carboxylic groups belonging to five independent SDB ligands and one oxygen atom (O(5)) from sulfonyl group belonging to another SDB ligand. The CO₂ adsorption capabilities of CaSDB and SrSDB at 298K under 1 atm are 1.37 and 1.17 mmol/g, respectively.

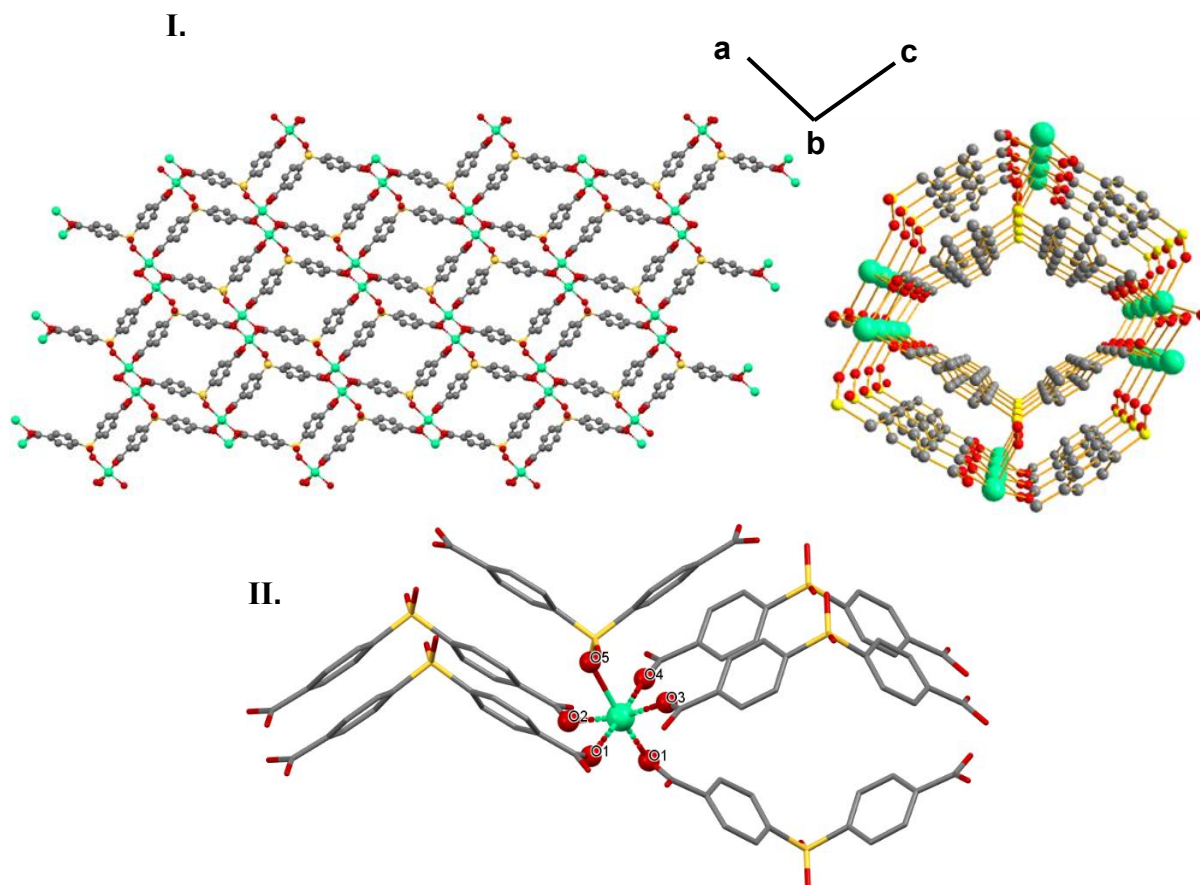


Figure 2-6 (I). 3D framework of MSDB (M=Ca or Sr). (II). The local coordination geometries of the central M (M=Ca or Sr) atom. (All H atoms are omitted for clarity)

2.1.3 Motivation of SSNMR study on s-block MOFs

For the structural characterization of MOFs, it is usually hard to obtain the ideal single crystals for X-ray diffraction, and detailed information cannot be obtained only from the PXRD data. In such case, several methods, like FTIR, EXAFS (Extended X-ray Absorption Fine Structure), XANES (X-ray Absorption Near Edge Structure) and solid-state NMR (SSNMR) were applied to MOFs to explore not only the structure but also the dynamic of guest molecule in the channel. Among those technologies, SSNMR was most used due to the ability to observe

the local structure around the nucleus of interest. ^{13}C and ^2H SSNMR can help identify the presence of organic linkers and the critical functional groups on the linkers. The isotope metal SSNMR can help obtain information about the metal sites within the MOFs.

Among six s-block metal MOFs in this study, ^7Li and ^{23}Na have a small spin quantum number ($3/2$) and rich natural abundance (92.5% for ^7Li and 100% for ^{23}Na), which allows them to be ideally sensitive isotopes. Although ^{25}Mg , with spin quantum number ($5/2$), is low sensitive nucleus and has approximately 10% natural abundance, it is the only NMR active isotope. In this case, ^{25}Mg NMR can still provide some information on the local environment of Mg sites. ^{133}Cs with spin quantum number ($7/2$) is NMR sensitive and has 100% natural abundance. With very low quadrupole moment, ^{133}Cs NMR can be perfectly used to study the Cs sites. Thus, in this study, ^{13}C , ^7Li , ^{23}Na , ^{25}Mg and ^{133}Cs MAS NMR were collected to study the framework structure of six MOFs.

2.2 Experimental

2.2.1 Alkali metal-based MOFs: M_2SDB ($\text{M} = \text{Li}, \text{Na}$ and Cs)

Li_2SDB , Na_2SDB and Cs_2SDB were prepared according to previously-reported research procedures with some modifications.^{1,2} For Li_2SDB , LiNO_3 (0.172 g), H_2SDB (0.067 g) and DMF (7 ml) were mixed in a 25 ml Teflon chamber; For Na_2SDB , NaOH (0.04 g), H_2SDB (0.0612 g), DMF (7 ml), EtOH (2 ml) and H_2O (1 ml) were mixed in a 25 ml Teflon chamber; For Cs_2SDB , CsCl (0.1684 g), H_2SDB (0.186 g), DMF (7 ml), EtOH (2 ml) and H_2O (1 ml) were mixed in a 25 ml Teflon chamber. Teflon chambers were then placed in a Teflon-lined stainless-steel autoclave with stable heating in the oven. 180 °C was applied to Li_2SDB for 2 days, 120 °C to Na_2SDB for 2 days and 90 °C to Cs_2SDB for 2 days as well. After cooling to room temperature, about 10 ml ethanol was used for washing the product and the white solid was obtained by vacuum filtration and dried at room temperature.

2.2.2 Alkali earth metal-based MOFs: MSDB ($\text{M} = \text{Mg}, \text{Ca}$ and Sr)

MgSDB , CaSDB and SrSDB were also prepared according to previously-reported research procedures with some modifications.^{3,4} For MgSDB , H_2SDB (0.1224 g), $\text{Mg}(\text{NO}_3)_2 \cdot \text{H}_2\text{O}$ (0.4100 g), EtOH (5 ml) and H_2O (1 ml) were mixed in a 25 ml Teflon chamber; For CaSDB ,

Ca(NO₃)₂•4H₂O (0.189 g), H₂SDB (0.198 g) and EtOH (10 ml) were placed into a small Teflon chamber; For SrSDB, Sr(NO₃)₂ (0.3384 g), H₂SDB (0.1224 g), EtOH (7 ml) and H₂O (3 ml) were mixed in 25 ml Teflon chamber. After the chamber is inserted into a Teflon-lined stainless-steel autoclave, the autoclaves were then placed into the oven and heated. For MgSDB, the mixture was heated at 150 °C for 1 day; For CaSDB, the autoclave was heated at 180 °C for 4 days; For SrSDB, the mixture was heated at 190 °C for 2 days. After cooling to room temperature, about 10 ml ethanol was used for washing the product and the white solid was obtained by vacuum filtration and dried at room temperature.

2.2.3 Activation scheme of MOFs

Since Li₂SDB has the non-porous framework and Cs₂SDB will decompose at around 100°C because of the coordinated water, four porous MOFs (Na₂SDB, MgSDB, CaSDB and SrSDB) were heated under vacuum for several hours to be activated (emptying the pores occupied by the solvent molecule during the synthesis). The detailed activation schemes are shown below:

- Na₂SDB: heated at 180°C for 24 hours under vacuum.
- MgSDB: heated at 200°C for 24 hours under vacuum.
- CaSDB: heated at 150°C for 24 hours under vacuum.
- SrSDB: heating at 150°C for 24 hours under vacuum.

2.2.4 Powder X-ray diffraction measurements

Powder X-ray Diffraction patterns were obtained with a Rigaku diffractometer using Cu- $\kappa\alpha$ radiation ($\lambda=1.5406 \text{ \AA}$). Samples were scanned in the range $5^\circ \leq 2\theta \leq 45^\circ$ at a rate of 10°/min with a step size of 0.02°.

2.2.5 Thermogravimetric Analysis (TGA)

TGA measurements were conducted by heating the sample from room temperature to 700 °C at a rate of 10 °C/min, which can be used to check if the pore is completely empty. Additionally, TGA can help to determine thermal stability by checking the decomposition temperature.

2.2.6 Solid-state state Nuclear Magnetic Resonance (SSNMR)

^{13}C CPMAS NMR, ^7Li (static and MAS) NMR and ^{23}Na (1D and 2D) MAS NMR spectra were recorded at 9.4 T on a Varian 400 WB spectrometer. ^{25}Mg MAS NMR and ^{133}Cs (static and MAS) NMR were conducted at 21.1 T on a Bruker AvanceII spectrometer at the National Ultrahigh-Field NMR Facility for Solids in Ottawa, Canada. Adamantane was used as a reference for ^{13}C CPMAS NMR, where the high field shift was set at 38.5 ppm. For the ^7Li and ^{23}Na MAS NMR, 1M LiCl solution and 1M NaCl solution were used respectively as the reference at 0.0 ppm. 1M $\text{MgCl}_2/\text{H}_2\text{O}$ and 0.1M $\text{CsCl}/\text{H}_2\text{O}$ were used as reference at 0 ppm for ^{25}Mg and ^{133}Cs MAS NMR, respectively. All experimental parameters including the rotor diameter, spin rate, optimized 90° pulse length, pulse delay and acquisition number are listed in **Table 2-1**. Additionally, the contact time for all ^{13}C CPMAS experiments is 2 ms. MNova was used to process NMR raw data such as Fourier transformation (FT), phase correction, and line broadening. ssNake software was used to simulate the patterns for specific spectra (^{25}Mg MAS NMR, ^{23}Na 1D and 2D MAS NMR), extracting NMR parameters like δ_{iso} , C_Q and η_Q that define NMR line shape.

Table 2-1 The experimental parameters setup of ^{13}C , ^7Li , ^{23}Na , ^{25}Mg and ^{133}Cs SSNMR.

	^{13}C CPMAS	^7Li static	^7Li MAS	^{23}Na 1D MAS
Rotor diameter (mm)	4	3.2	3.2	3.2
Spin rate (kHz)	10	-	10	20
90° pulse length (μs)	3.3	0.7	1.25	1.0
Pulse delay (s)	15	1	1	1
Acquisition number	>4000	3424	3024	1200
	^{23}Na 2D MAS	^{25}Mg MAS	^{133}Cs MAS	^{133}Cs MAS
Rotor diameter (mm)	3.2 mm	7 mm	3.2 mm	3.2 mm
Spin rate (kHz)	20 kHz	8 kHz	5 kHz	20 kHz
90° pulse length (μs)	3.0(1 st); 1.0(2 nd)	12	1	1
Pulse delay (s)	1	5	120	120
Acquisition number	64 x 128	12000	482	128

2.3 Results and discussion

2.3.1 Synthesis and characterization with PXRD

PXRD patterns of all as-made complexes are consistent with the simulated ones from the literature^{1,2,3,4} (**Figure 2-7**), which indicates that Li₂SDB, Na₂SDB, Cs₂SDB, MgSDB, CaSDB and SrSDB were successfully obtained according to the synthesis scheme listed before. Specifically, for porous MOFs (Na₂SDB, MgSDB, CaSDB and SrSDB), the PXRD patterns after activation are plotted as well. The peaks of activated Na₂SDB, CaSDB and SrSDB show agreement with the literature patterns, which suggests the frameworks of Na₂SDB, CaSDB and SrSDB stay unchanged after removing the molecules that are remained in the channel during the synthesis.

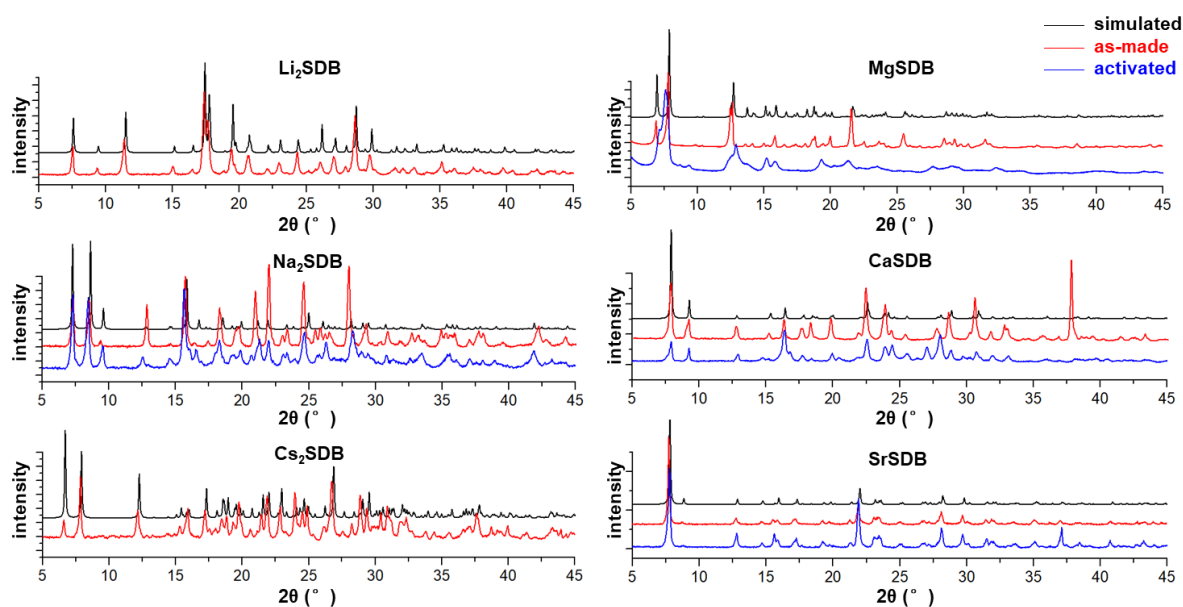


Figure 2-7 Powder x-ray diffraction patterns for MOFs.

From the literature, it is known that the $\text{Mg}_3(\text{OH})_2(\text{SDB})_2(\text{EtOH})(\text{H}_2\text{O})_3$ (as-made MgSDB) will change its structure during activation, forming the de-solvated phase $\text{Mg}_3(\text{OH})_2(\text{SDB})_2$ (activated MgSDB). The typical change in PXRD patterns between as-made and activated MgSDB is that the first two peaks around 2θ value of 6° will transfer into a single peak after activation, as shown in **Figure 2-8** where the MgSDB is activated after temperature reaches 200°C .³ The PXRD patterns for activated MgSDB (blue line) display the combination of the two peaks at the low 2θ range, which indicates the existence of activated MgSDB. However, the broad peaks instead of sharp peaks are found through all 2θ angle range, which

suggests the decomposed or disordered framework is yielded during the activation. Additionally, it is worth mentioning that CaSDB and SrSDB have similar patterns, given the fact that they share the same structure.

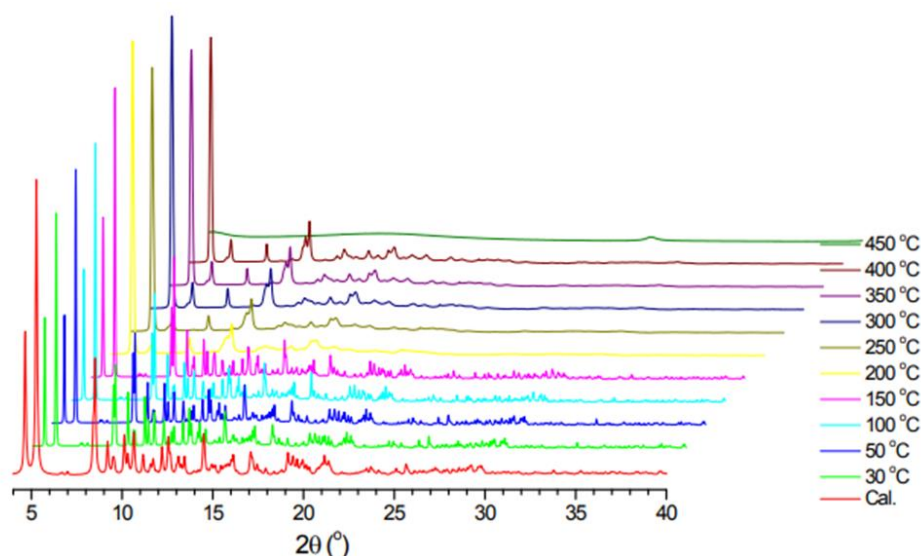


Figure 2-8 Powder x-ray diffraction patterns for MgSDB with elevating temperature.³

For Cs₂SDB, because of the similar temperature for loss of guest water molecule and a coordinated water molecule, it is not implementable to directly activate Cs₂SDB by heating under vacuum. Acetone and ethanol were used to exchange with the guest water molecules in channels, then the temperature needed for the activation will be lowered, which can prevent the coordinated water molecules from being removed. **Figure 2-9** exhibits the PXRD patterns of as-made Cs₂SDB and Cs₂SDB after the solvent exchange in ethanol or acetone. Several peaks at the low angle range are missing, indicating the changed structure of Cs₂SDB after the solvent exchange was found. It can be proved that the new framework of Cs₂SDB after solvent exchange is non-porous structure by the TGA analysis in following section. In such a case, Cs₂SDB will not be properly activated and discussed in this thesis.

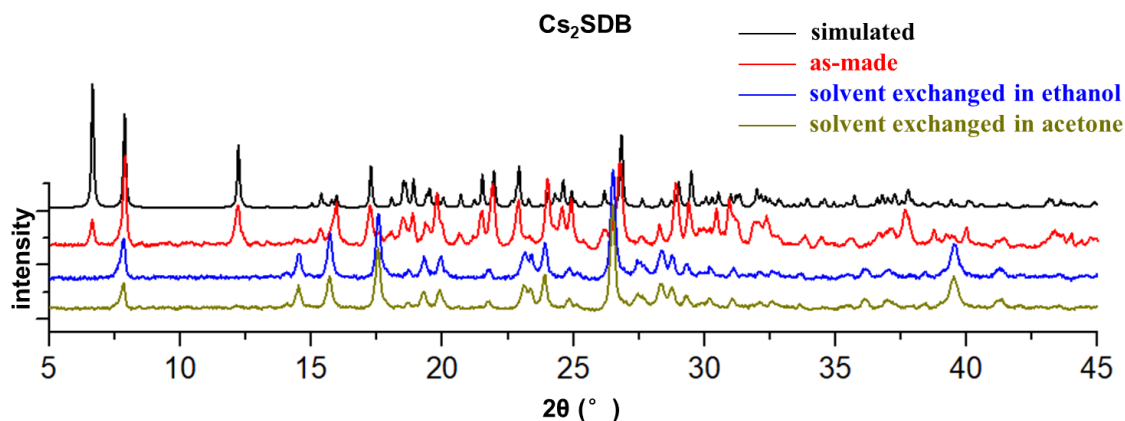


Figure 2-9 Powder x-ray diffraction patterns for Cs₂SDB with solvent exchange in ethanol and acetone.

2.3.2 Thermal stability with TGA

The TGA data for as-made and activated MOFs are plotted in **Figure 2-10**. Five MOFs (except Cs₂SDB) are measured to have the decomposition temperature at around 500 °C. since the crucibles containing either as-made or solvent-exchanged Cs₂SDB underwent vibration around 400 °C, the highest temperature for Cs₂SDB is only set at 350 °C to obtain the clear mass loss curves, especially around 100 °C, which represents loss of water molecules.

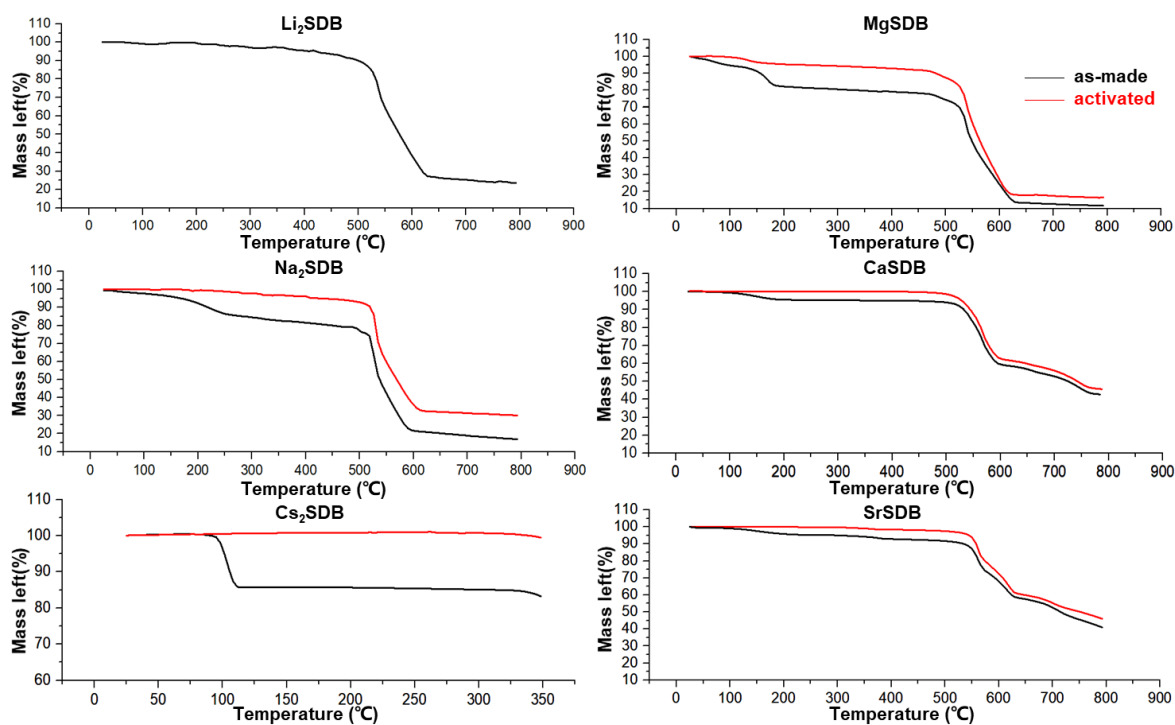


Figure 2-10 TGA curves for MOFs.

For Li₂SDB, only the curve of the as-made complex is shown since Li₂SDB does not have

a porous structure, which is also proved by the flat line before 500 °C. Comparing the mass loss curves in Na₂SDB, MgSDB, CaSDB and SrSDB, they all display the decreased number of molecules inside of the channels after the activation. In Na₂SDB, the TGA curve of the activated sample exhibits a flat line before the temperature reaches around 500 °C, indicating that the pore does not contain any solvent molecule after activation. The as-made thermal curve has a smooth weight loss drop at around 100 °C, which indicates the loss of ethanol and water molecules that remained in the pore during synthesis. Another weight loss drop is found starting at around 170 °C due to DMF molecules lost. By further NMR experiment, it is found that DMF within Na₂SDB cannot be removed totally during the activation, and approximately 1/3 of DMF molecules are remained inside of the porous channels according to the integral ratio of DMF peaks in the ¹³C spectra of as-made and activated Na₂SDB. As proved by PXRD that Cs₂SDB undergoes the structural change during the solvent exchange, its TGA curves can still deliver some information on the framework. The thermal curve of as-made Cs₂SDB displays a huge weight loss drop around 100 °C, which refers to the loss of both coordinated water molecules and guest water molecules. Additionally, the thermal curve of Cs₂SDB after solvent exchange exhibits the flat line before reaching 350 °C, which indicates there is no solvent molecule (either acetone, ethanol or water) adsorbed by the Cs₂SDB anymore. The TGA analysis provides a complement to the PXRD result, where the porous structure of Cs₂SDB does not exist anymore after the solvent exchange.

The decomposition of coordinated ethanol molecules happens at 100 °C and coordinated water molecules happen at 150 °C for MgSDB. Combined with the guest water molecules lost within the pore at around 100 °C, two weight loss drops are shown at 100 °C and 150 °C for the as-made MgSDB. After the activation, a slight weight loss happens at the temperature ranging from 100 °C to 150 °C, which may result from a small amount of inactivated MgSDB. The TGA curves of CaSDB and SrSDB exhibit similar results. The weight loss drops at 70 °C for guest ethanol molecules and 100 °C for guest water molecules within the channel before activation can be easily found, and the flat curves for activated CaSDB or SrSDB demonstrate the empty pore after activation.

2.3.3 Characterization of linker local structure

2.3.3.1 SDB ligands

To identify the carbon signals of SDB linker in the ^{13}C CPMAS NMR spectra of MOFs, the spectrum of the precursor, H_2SDB , was also measured, shown in **Figure 2-11** (asterisk * indicates spinning sidebands). According to the literature, within the structure of H_2SDB , the single peak at 171.3 ppm is corresponding to the C1, the single peak at around 146.0 ppm is for C5 and three peaks at 133.5 ppm, 131.6 ppm and 129.7 ppm are from the carbon atoms in the phenyl group (C2, C3 and C4)⁵. Two C1 atoms and two C5 atoms in the same SDB linker are crystallographically equivalent, corresponding to a single C1 and C5 peak. However, two inequivalent C1 and two inequivalent C5 atoms within one SDB ligand can be observed if the SDB ligand loses mirror plane as its symmetry element, which can result from: (1). the coordination that happens on the carboxyl and sulfonyl groups; (2). The physical interaction between other molecules and SDB ligand. Additionally, two inequivalent SDB ligands within a single unit cell can also result in two inequivalent C1 and C5 atoms from two independent SDB ligands. Any situation that mentioned above will cause the splitting of the single C1 and C5 peak. To obtain an overview of the local structure of SDB ligands in four MOFs without influence from the guest molecule, the spectra of dried non-porous MOF (Li_2SDB), dried Cs_2SDB which cannot be activated and four activated porous MOFs (Na_2SDB , MgSDB , CaSDB and SrSDB) are shown **Figure 2-11** as well.

All carbon atoms in SDB ligands have different sensitivities to the metal coordination. It is worth discussing the C2 and C5 carbon in this case since they are both three atoms away from the coordination site. Compared with the carbon that is connected to the carboxylic group, the carbon bound to the sulfonyl group is more sensitive to the metal coordination. For example, the coordination between metal atom and sulfonyl and carboxyl group will result in an asymmetry of SDB ligand, which causes carbon atoms on the two sides of the SDB ligand inequivalent. Since the carbon bound to the sulfonyl group is more sensitive, a larger difference in the chemical shift of two C5 atoms will be observed than that of two C2 atoms within the single SDB ligand.^{6,7}

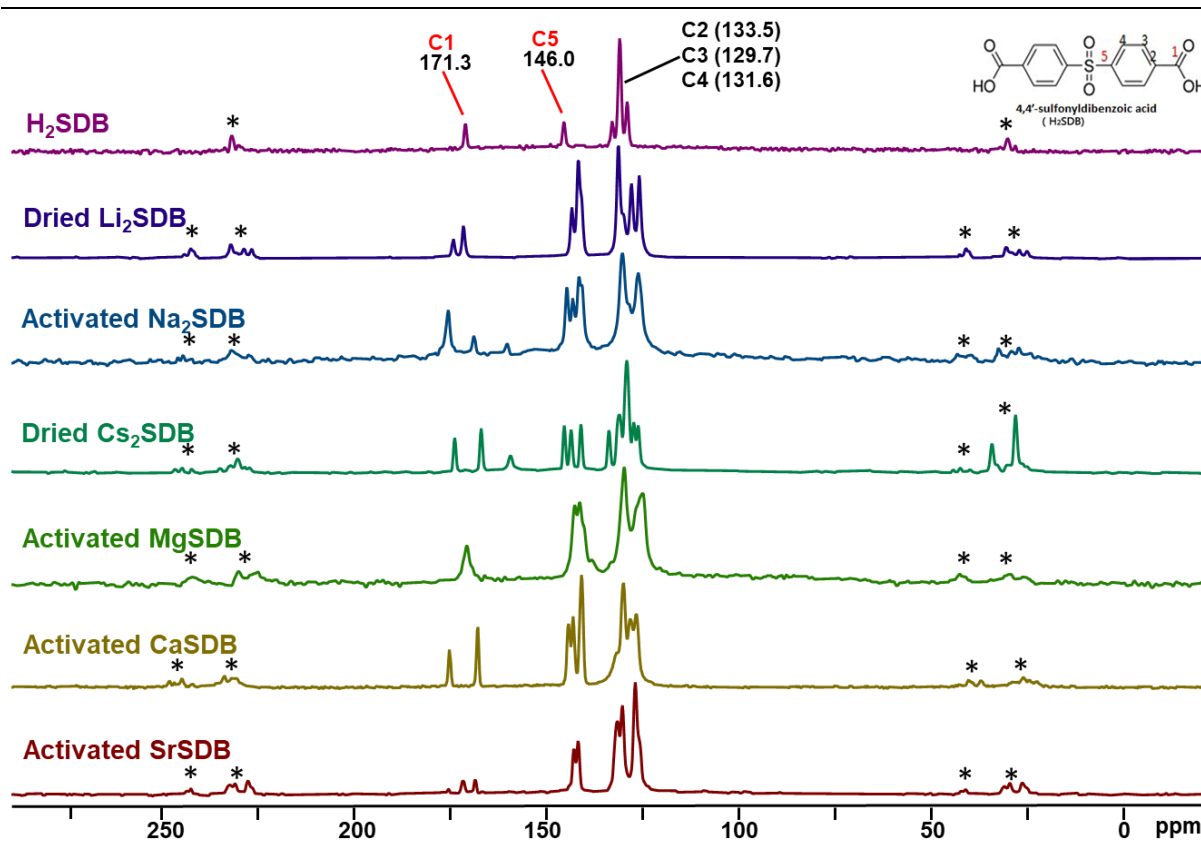


Figure 2-11 The overview of ^{13}C CPMAS NMR spectra for pure H_2SDB (organic linker) and six SDB MOFs based on s-block metals. (* corresponds to spinning side bands)

The number of inequivalent C1 and C5 atoms in each MOF (based on each crystal structure) and the number of inequivalent C1 and C5 that can be observed from the ^{13}C NMR spectra are given in **Table 2-2**. The intensity ratios of the resonances due to C1 or C5 in all spectra are listed in **Table 2-3** (which will be specified with ^{13}C CPMAS NMR spectra for each MOFs in following discussion), and **Table 2-4** exhibits the chemical shift values for each resonance due to C1 or C5 in all spectra. All the data in these tables can reveal the symmetry of each unit cell in all six MOFs and will be discussed in following sections.

Table 2-2 The number of inequivalent C1 and C5 atoms in each MOF (based on each crystal structure) and the number of C1 and C5 that can be observed from the ^{13}C NMR spectra.

	Space group	Inequivalent C1 in structure	Inequivalent C5 in structure	Inequivalent C1 from spectra	Inequivalent C5 from spectra
<i>H₂SDB</i>	-	1	1	1	1
<i>Li₂SDB</i>	P2 ₁ /n	2	2	4	4
<i>Na₂SDB</i>	P-1	2	2	4	4
<i>Cs₂SDB</i>	P-1	2	2	4	4
<i>MgSDB</i>	P2/c	2	2	4	4
<i>CaSDB</i>	P2 ₁ /n	2	2	4	4
<i>SrSDB</i>	P2 ₁ /n	2	2	4	4

Table 2-3 The chemical values of each resonance at C1 and C5 site in all ^{13}C NMR spectra.

(The chemical shift value for shoulder are shown in bracket)

	δ_{iso} of resonance(s) at C1 site	δ_{iso} of resonance(s) at C5 site
<i>Dried Li₂SDB</i>	174.5; 171.9	143.9; 142.3; (141.4)
<i>As-made Na₂SDB</i>	175.6; 168.9	146.1; 143.6; 142.7; 141.2
<i>Activated Na₂SDB</i>	175.8; 169.1	145.3; 143.7; 142.2; 141.4
<i>Dried Cs₂SDB</i>	175.4; 167.3	150.3; 144.2; 139.9
<i>As-made MgSDB</i>	(173.5); 172.6	144.5; 143.4; 142.0
<i>Activated MgSDB</i>	171.0	143.3; 141.8; (140.8)
<i>As-made CaSDB</i>	175.5; 168.1	144.9; 143.5; 141.5
<i>Activated CaSDB</i>	175.5; 168.2	144.8; 142.8; 141.5
<i>As-made SrSDB</i>	175.8; 168.8	144.5; 143.9; 142.2
<i>Activated SrSDB</i>	176.7; 172.8; 168.8	143.4; 142.3

Table 2-4 The integral ratio of each resonance at C1 and C5 site in all ^{13}C NMR spectra.

	Integral ratio of resonances at C1 site	Integral ratio of resonances at C5 site
<i>Dried Li₂SDB</i>	1 : 1.8	1 : 1.8 : 1.1
<i>As-made Na₂SDB</i>	1 : 1.1	1 : 1.1 : 1.1 : 1.2
<i>Activated Na₂SDB</i>	1 : 1.9	1 : 0.8 : 1 : 0.9
<i>Dried Cs₂SDB</i>	1 : 1.5	1 : 1.1 : 1.2
<i>As-made MgSDB</i>	1 : 2.3	1 : 1.4 : 1.6
<i>Activated MgSDB</i>	-	1 : 0.9 : 0.9
<i>As-made CaSDB</i>	1 : 1.5	1 : 1 : 1.9
<i>Activated CaSDB</i>	1 : 1.5	1 : 1.2 : 2.1
<i>As-made SrSDB</i>	1 : 1.3	1 : 1.2 : 1.9
<i>Activated SrSDB</i>	0.3 : 1 : 0.8	1 : 1.3

2.3.3.2 Alkali metal MOFs

Within Li₂SDB, there are two equivalent SDB ligands in the unit cell, which are related by an inversion center according to X-ray structure. However, unlike H₂SDB where two phenyl rings in each SDB are equivalent, two halves of each SDB become inequivalent after the coordination with Li centers in Li₂SDB. Thus, each SDB has two inequivalent C1 and C5 originating from two sides of a single asymmetric SDB ligand. In this case, two distinct resonances should be seen for both C1 and C5 in the ^{13}C CPMAS NMR spectrum.

In the experimental Li₂SDB ^{13}C CPMAS NMR spectrum (**Figure 2-12**), two resonances due to the C1 (174.5 ppm and 171.9 ppm) and three resonances at C5 site (143.9 ppm and 142.3 ppm with a resonance at around 141.0 ppm as shoulder) due to C5 are observed. Besides all resonances associated with the SDB linker (125 - 175 ppm) and corresponding spinning sidebands, there are no extra peaks found, consistent with the absence of DMF used in the synthesis in the non-porous framework.

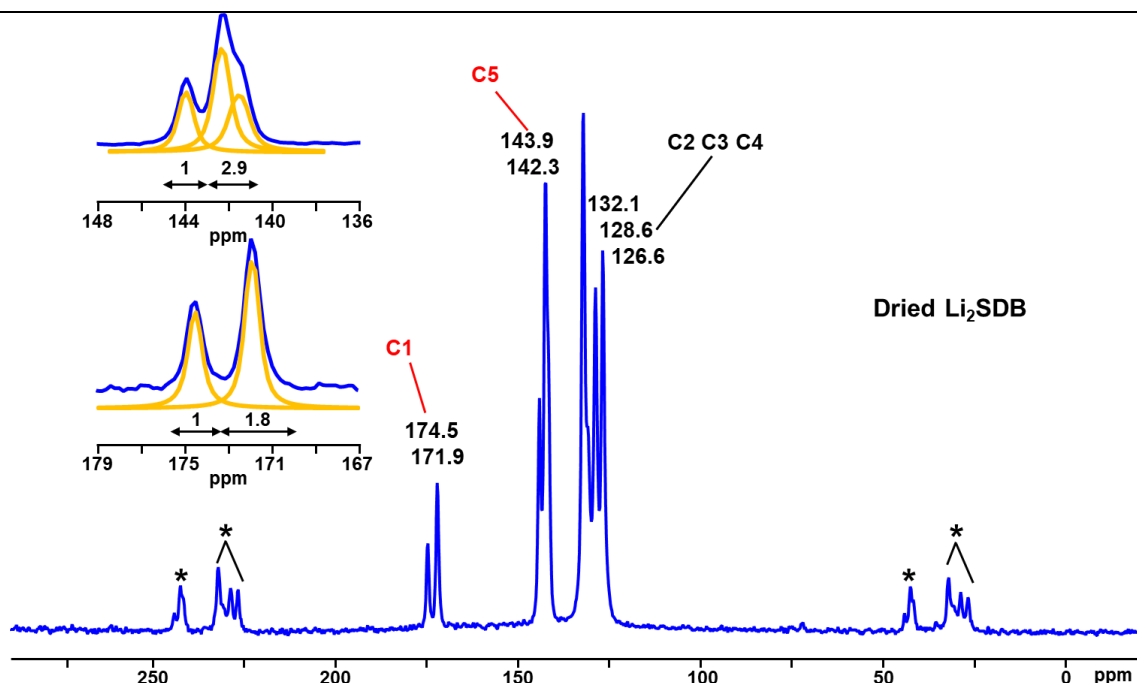


Figure 2-12 ^{13}C CP MAS NMR spectrum of dried Li_2SDB . (* corresponds to spinning side bands) (Experimental patterns are in blue and resolved peaks are labeled in yellow)

The integral ratio of the resonances due to C5 is 1 : 1.8 : 1.1, which infers that four crystallographically distinct C5 atoms exist in Li_2SDB . Existence of four C5 carbons suggests that the inversion center which relates the two SDB linkers in the unit cell does not actually exist as indicated by the X-ray structure. This results in total of four different C5 signal as observed. In the carboxylate region, the relative intensity ratio between the two resonances due to C1 atoms at 174.5 and 171.9 ppm is 1 : 1.8, clearly indicating that the number of inequivalent C1 carbons is greater than two as predicted by the X-ray structure. Since the CP intensity depends on the distance between hydrogen atoms and the carbon of interest, the CP method is not quantitative. At this point, it is difficult to explain why the 2 peaks due to inequivalent C1 atoms only give a 1:1.8 ratio. Obviously, one of the peaks is less enhanced by CP. More work is needed to understand the CP intensity.

In short, the ^{13}C CPMAS data clearly show that the actual crystal structure of Li_2SDB is different from that obtained from X-ray diffraction. It is very likely that the inversion center in original structure is absent.

Within Na_2SDB , there are also two equivalent SDB ligands in the unit cell, related by an inversion center. Like Li_2SDB , two phenyl rings in each SDB ligand are inequivalent as well.

In this case, two sides of a single asymmetric SDB ligand will lead to a total of two inequivalent C1 and C5 atoms. Two distinct resonances should be seen for both C1 and C5 in the ^{13}C CPMAS NMR spectra.

Figure 2-13 shows the ^{13}C CPMAS NMR spectra of as-made and activated Na_2SDB . Two resonances due to C1 (175.6 ppm and 168.9 ppm in as-made Na_2SDB ; 175.8 ppm and 169.1 ppm in activated Na_2SDB) and four distinct peaks due to C5 are observed in the spectra of both as-made and activated Na_2SDB . Besides the spinning sidebands, three solvent-associated (DMF) resonances are located at 160.5 ppm, 34.5 ppm and 29.6 ppm in the spectrum of as-made Na_2SDB . The intensities of the DMF peaks decrease significantly in the spectrum of activated Na_2SDB , suggesting most of the DMF was removed during activation. Additionally, all peaks become broader after activation, which indicates the slightly decreased crystallinity.

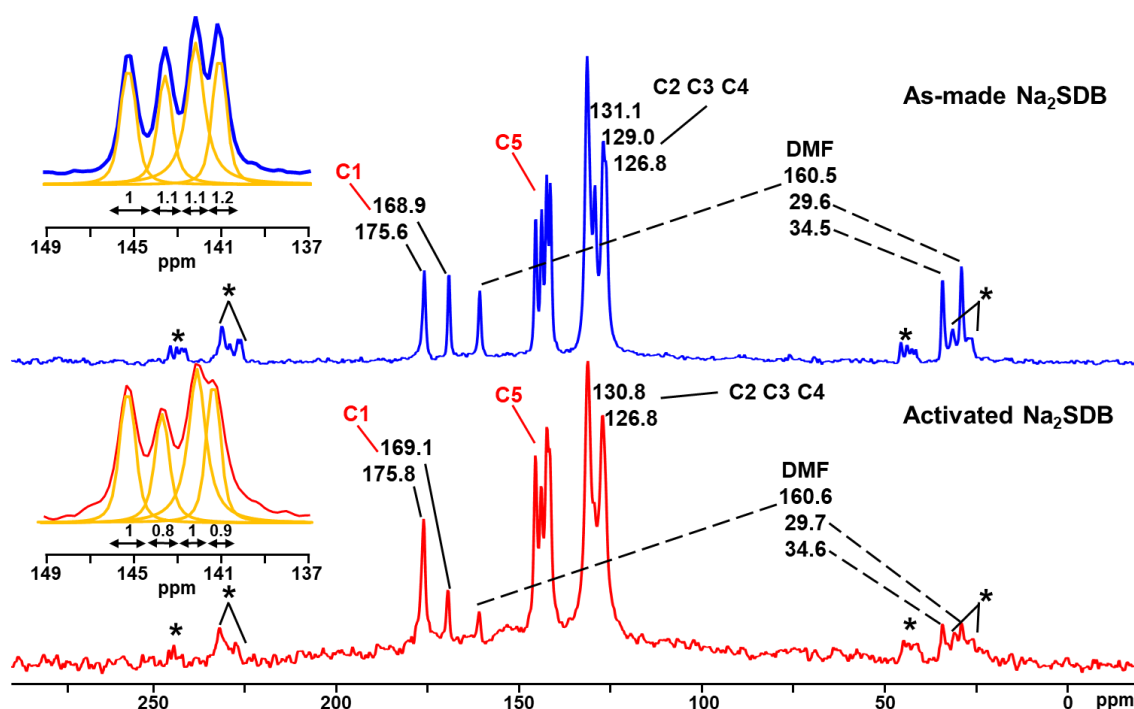


Figure 2-13 ^{13}C CP MAS NMR spectra of as-made and activated Na_2SDB . (* corresponds to spinning side bands) (Experimental patterns are in blue or red, and resolved peaks are labeled in yellow)

Four distinct resonances due to C5 have approximately same integral values (specified in **Figure 2-13**), which clearly indicates four crystallographically distinct C5 atoms existing in both as-made and activated Na_2SDB . This observation hints the absence of an inversion center

in the unit cell. The integral ratio of the resonances at 169.1 and 175.8 ppm is 1 : 1 in as-made Na₂SDB, which suggests four C1 carbons appears as two groups of peaks with equal intensity. However, the ratio is 1 : 1.9 for activated Na₂SDB, which also confirms the lack of inversion center relating the two SDBs in the unit cell. As is the case for Li₂SDB, one of the four peaks of the activated sample is less enhanced by CP, which results in the ratio of 1 : 1.9. Existence of four C1 carbons and four C5 carbons suggests the inversion center which relates to two SDB ligands in the unit cell does not actually exist as indicated by the X-ray structure.

Additionally, Na ions have larger orbitals and electron density than Li ions, resulting in greater shielding interaction, which results in a greater difference in chemical shift between two resonances at the C1 site (175.8 – 169.1 ppm for Na₂SDB and 174.5 – 171.9 ppm for Li₂SDB) (**Table 2-4**). Overall, the ¹³C CPMAS data clearly indicates that the actual crystal structure of Na₂SDB is different from that obtained from X-ray diffraction, likely due to the absence of inversion center in original structure.

Like two alkali metal MOFs mentioned above, Cs₂SDB also has two equivalent SDB ligands in its unit cell, related by an inversion center. Two phenyl rings in each SDB ligand are inequivalent as well, resulting in a total of two inequivalent C1 and C5. Two distinct resonances should be seen for both C1 and C5 in the ¹³C CPMAS NMR spectra.

The ¹³C CPMAS NMR spectrum of dried Cs₂SDB is shown in **Figure 2-14**. Two distinct sharp peaks are observed at 175.4 ppm and 167.3 ppm due to C1 and three resonances due to C5 are observed at 150.3 ppm 144.2 ppm and 139.9 ppm. DMF associated resonances can also be found at 161.1 ppm, 35.6 ppm and 30.7 ppm since DMF molecules, as solvent in synthesis, are remained within the porous channels. Because the Cs₂SDB cannot be successfully activated via heating or solvent exchanging, the spectrum for activated Cs₂SDB was not acquired, which requires more works in future to explore the structure of Cs₂SDB without solvent molecules adsorbed.

Three distinct resonances due to C5 with approximately same integral values (specified in **Figure 2-14**) suggest the number of inequivalent C5 carbons is greater than two as predicted by the X-ray structure, which hints the absence of an inversion center in the unit cell. Since there are two C1 or C5 atoms in each SDB ligand, the number of crystallographically distinct

C1 or C5 can either be 2 or 4. In this case, four inequivalent C5 atoms are likely included, two of which give the signals with similar chemical shift values. Because one peak is less enhanced by CP, three resonances with same intensities are resulted. Two distinct C1 resonances have the integral ratio of 1 : 1.5, which likely correspond to two groups of C1 atoms. Each group contains two distinct C1 atoms that give similar chemical shift values. This observation also confirmed the inversion center that relates to two SDB ligands does not exist in the unit cell as indicated by the X-ray structure.

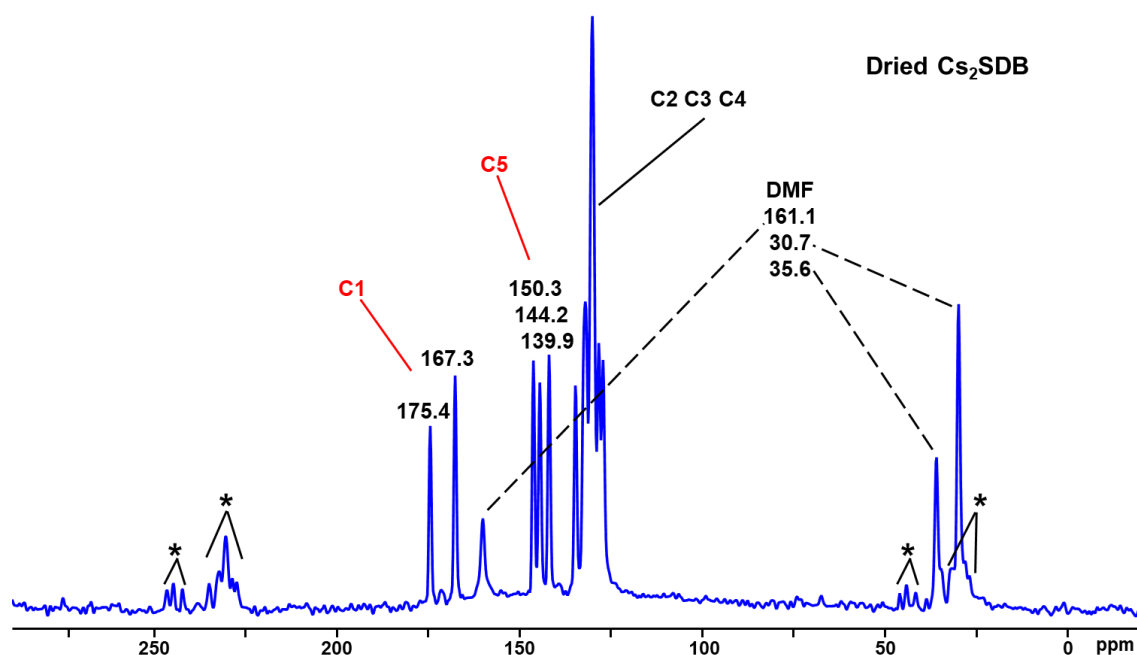


Figure 2-14 ¹³C CP MAS NMR spectra of dried Cs₂SDB. (* corresponds to spinning side bands)

The difference in chemical shift values between two C1 peaks (175.4 - 167.3 ppm) is larger than that in both Li₂SDB and Na₂SDB, which proves the explanation discussed above that the larger orbital and electron density of the metal ions strengthen the shielding interaction. In short, the ¹³C CPMAS data clearly show that the actual crystal structure of Cs₂SDB is different from that obtained from X-ray diffraction. It is very likely that the inversion center in original structure is absent.

2.3.3.3 Alkali earth metal MOFs

Within as-made MgSDB, there are four SDB ligands included in a single unit cell. Relating by the inversion center, four SDB ligands can be divided into two equivalent groups. In each

group, two inequivalent SDB ligands are involved. Two phenyl rings in each SDB ligand are inequivalent as well. In such case, a total of four inequivalent C1 and C5 atoms emerged, which leads to four distinct resonances for both C1 and C5 in the ^{13}C CPMAS NMR spectra. After the removal of the coordinated water and ethanol molecules, the activated MgSDB still contains four SDB ligands in each unit cell. However, all of them are equivalent, related by an inversion center and C2 rotation axis. A total of two inequivalent C1 and C5 atoms originates from two sides of a single asymmetric SDB ligand. In this case, two distinct resonances should be seen for both C1 and C5 in the ^{13}C CPMAS NMR spectrum.

Figure 2-15 shows the ^{13}C CPMAS NMR spectra of as-made MgSDB and activated MgSDB. In as-made MgSDB spectrum, two distinct resonances due to C1 (173.5 ppm as the shoulder and 172.6 ppm) and three distinct resonances due to C5 (144.5, 143.4 and 142.0 ppm) are observed. After activation, one broad peak due to C1 (171.0 ppm) and three distinct resonances due to C5 (143.3, 141.8 and 140.8 ppm) are observed in the spectrum of activated MgSDB. Besides the spinning sidebands, two extra peaks (59.2 ppm and 15.3 ppm) are found in the spectrum of as-made MgSDB, associated with coordinated and adsorbed ethanol that was used as solvent in synthesis. Two ethanol resonances are no longer seen after activation, which indicates all ethanol molecules are removed. Additionally, all peaks become broader after activation, which indicates the slightly decreased crystallinity.

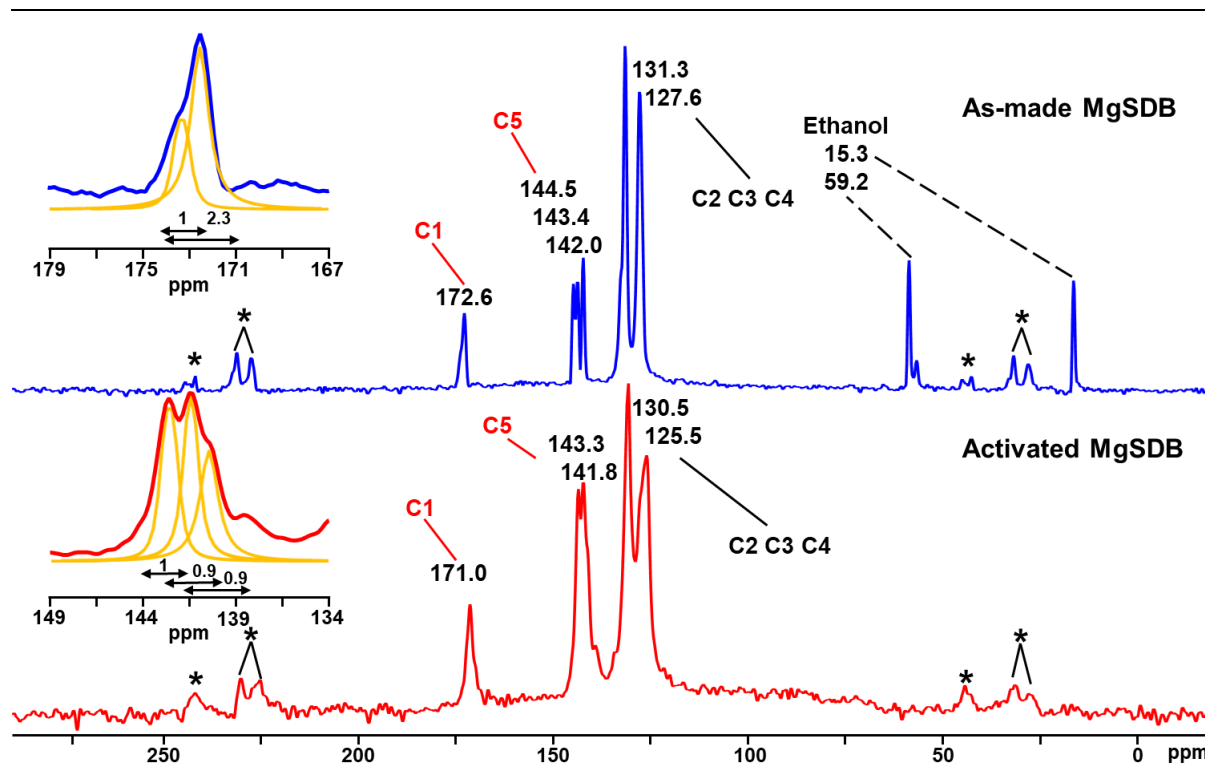


Figure 2-15 ^{13}C CP MAS NMR spectra of as-made and activated MgSDB. (* corresponds to spinning side bands) (Experimental patterns are in blue or red, and resolved peaks are labeled in yellow)

Three distinct resonances due to C5 in as-made MgSDB spectrum have integral ratio of 1 : 1.4 : 1.6, which suggests four crystallographically distinct C5 atoms existing in as-made MgSDB if taking account of the different enhancement on each peak from CP. While two C1 peaks give the intensity ratio of 1 : 2.3, further confirming the existence of four C1 atoms within a single unit cell. This observation supports the X-ray structure. In activated MgSDB spectrum, the one broad resonance due to C1 represents overlapping of several peaks with similar chemical shift value. Three resonances due to C5 have intensity ratio of 1 : 0.9 : 0.9, which hints at least three crystallographically independent C5 atoms within a single unit cell. Since MgSDB has a restructured framework after activation, the absence of inversion center relating to four SDB ligands will result in the ratio of 1 : 0.9 : 0.9.

Overall, it can be concluded that the ^{13}C CPMAS NMR spectrum of as-made MgSDB shows the structure consistent with that obtained from X-ray diffraction. However, activated MgSDB loses its crystallinity, and the structure is different from X-ray structure due to the absence of inversion center.

Within both CaSDB and SrSDB, there are four SDB ligands within each unit cell as they have the same structure. Similar to activated MgSDB, an inversion center and C2 rotation axis are relating to all four SDB ligands, resulting in all SDB ligands equivalent within a single unit cell. Two phenyl rings in each SDB ligand are inequivalent, leading a total of two inequivalent C1 and C5. Two distinct resonances should be seen for both C1 and C5 in the ^{13}C CPMAS NMR spectra.

^{13}C CPMAS NMR spectra of as-made and activated CaSDB are exhibited in **Figure 2-16**, all peaks due to C1 and C5 show high consistency before and after activation. Three resonances due to C5 (144.8, 143.5 and 141.5 ppm) and two distinct resonances due to C1 (175.5 and 168.1 ppm) are observed in both spectra of as-made and activated CaSDB. Ethanol associated resonances (55.9 and 15 ppm) are observed only in the spectrum of as-made CaSDB, which indicates adsorbed ethanol are all removed after activation.

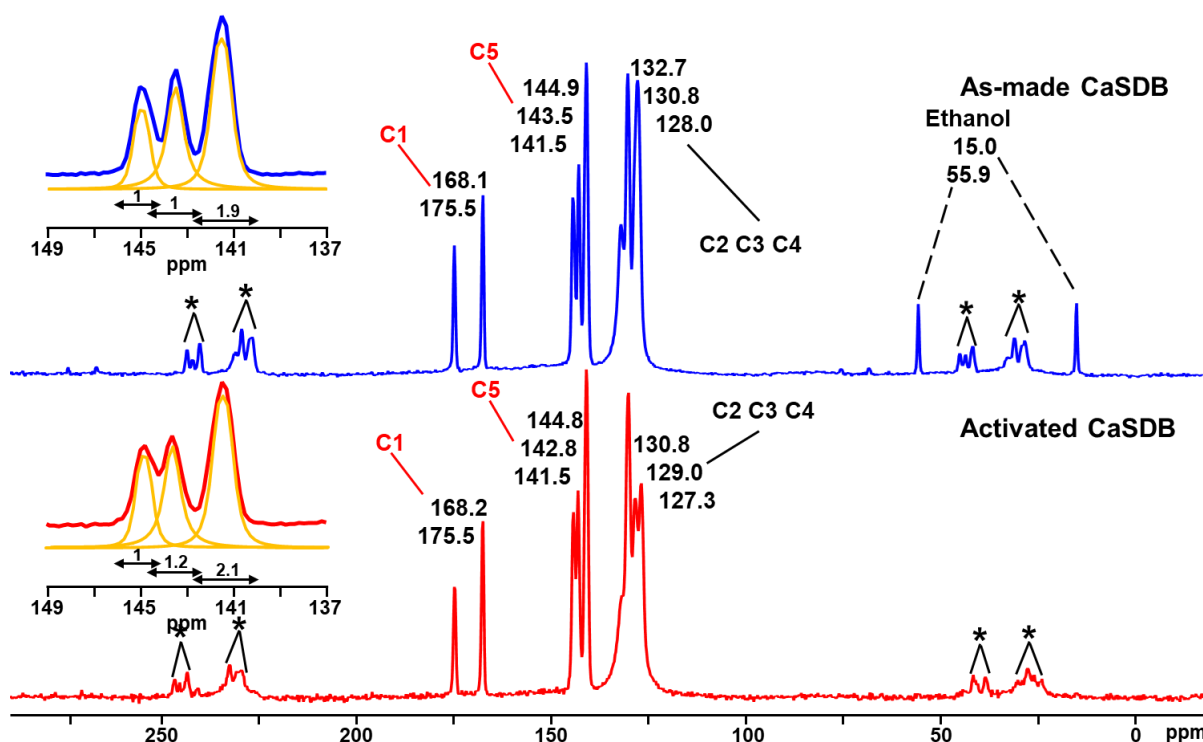


Figure 2-16 ^{13}C CP MAS NMR spectra of as-made and activated CaSDB. (* corresponds to spinning side bands) (Experimental patterns are in blue or red, and resolved peaks are labeled in yellow)

Three distinct resonances due to C5 have the intensity ratio of approximately 1 : 1 : 2 in spectra of both as-made and activated CaSDB, hinting four crystallographically distinct C5

atoms exist in CaSDB. This observation suggests the absence of either inversion center or the C2 rotation axis in the unit cell. The integral ratio of the resonances due to C1 is 1 : 1.5 in the spectra of both as-made and activated CaSDB, which suggests four C1 carbons may appear as two groups of peaks. Since one peak is less enhanced by CP, the ratio of 1 : 1.5 is obtained. Existence of four C1 carbons and four C5 carbons suggests either the inversion center or C2 rotation axis which relates to four SDB ligands in the unit cell does not actually exist as indicated by the X-ray structure.

Figure 2-17 shows the ^{13}C CPMAS NMR spectra of as-made and activated SrSDB. Two resonances due to C1 (175.8 and 168.8 ppm) and three distinct resonances due to C5 (144.5, 143.9 and 142.2 ppm) are observed in the spectrum of as-made SrSDB. While three distinct resonances due to C1 (176.7, 172.8 and 168.8 ppm) and two distinct resonances (143.4 and 142.3 ppm) are observed in the spectrum of activated SrSDB. Besides the spinning sidebands, two ethanol associated resonances (58.5 and 15.5 ppm) are only found in the spectrum of as-made SrSDB, indicating the adsorbed ethanol is totally removed. The changed number of resonances due to C1 and C5 between the spectra of as-made and activated SrSDB suggests the local environment of SDB ligands varies after activation.

Three distinct resonances due to C5 in the spectrum of as-made SrSDB has the integral ratio of 1 : 1.2 : 1.9, which clearly indicates four crystallographically distinct C5 atoms existing in as-made SrSDB, suggesting the absence of either inversion center or C2 rotation axis relating to four SDB ligands in a single unit cell. An intensity ratio of 1 : 1.3 is given by two resonances due to C1, which results from two groups of peaks with equal intensity. In the spectrum of activated SrSDB, the new resonance appears at 172.8 ppm, leading a total of three resonances due to C1 with the integral ratio of 0.3 : 1 : 0.8. The resonance at 144.5 ppm is no longer seen, resulting two resonances with intensity ratio of 1 : 1.3 due to C5. This observation hints there is a change on the structure of SrSDB when being activated. The crystallinity is maintained due to the sharp peaks shown in the spectrum of activated SrSDB, but the number of inequivalent C1 and C5 carbons is greater than two as predicted by the X-ray structure.

In short, the ^{13}C CPMAS data clearly show that the actual crystal structure of CaSDB and SrSDB is different from that obtained from X-ray diffraction due to the absence of inversion center or C_2 rotation axis. Additionally, the structure of SrSDB is changed after activation, which is different from the result obtained from X-ray diffraction. More work is required to understand the structure change of SrSDB during the activation.

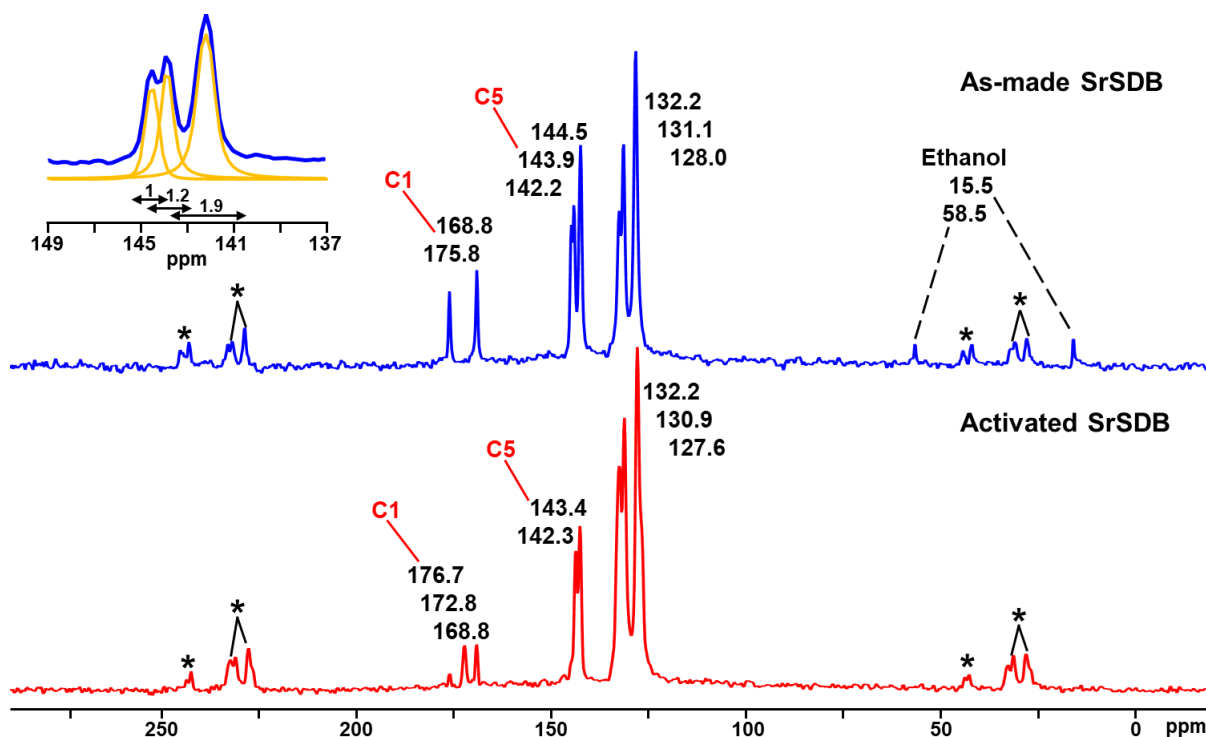


Figure 2-17 ^{13}C CP MAS NMR spectra of as-made and activated SrSDB. (* corresponds to spinning side bands) (Experimental patterns are in blue and resolved peaks are labeled in yellow)

2.3.4 Characterization of metal local structure

The environments of metal ions also play a significant role in the topology of MOFs and their applications. To obtain detailed information on the local structure for those SDB MOFs, ^7Li , ^{23}Na , ^{133}Cs and ^{25}Mg NMR were used. ^7Li MAS and static spectra of dried Li_2SDB are shown in **Figure 2-18**. Within Li_2SDB , there are two crystallographically distinct Li sites in its unit cell, which should lead to two distinct resonances in ^7Li MAS NMR spectrum. However, in the ^7Li MAS NMR spectrum, only one sharp resonance is observed at 0.7(1) ppm, with six corresponding spinning sidebands. The static spectrum gives the patterns with a broader lineshape. However, it is hard to tell from either spectrum if the resonance results from two Li

sites due to the overlapping of the resonances with similar chemical shifts. Li(1) is tetrahedrally coordinated with four carboxylate groups and Li(2) is tetrahedrally coordinated with three carboxylate groups and one sulfonyl group. In such case, two Li associated resonances will have very similar C_Q and η_Q , resulting in the difficulty in observing the distinct resonances. In short, the ^7Li NMR spectra cannot confirm the exact same structure reported in the published paper.¹

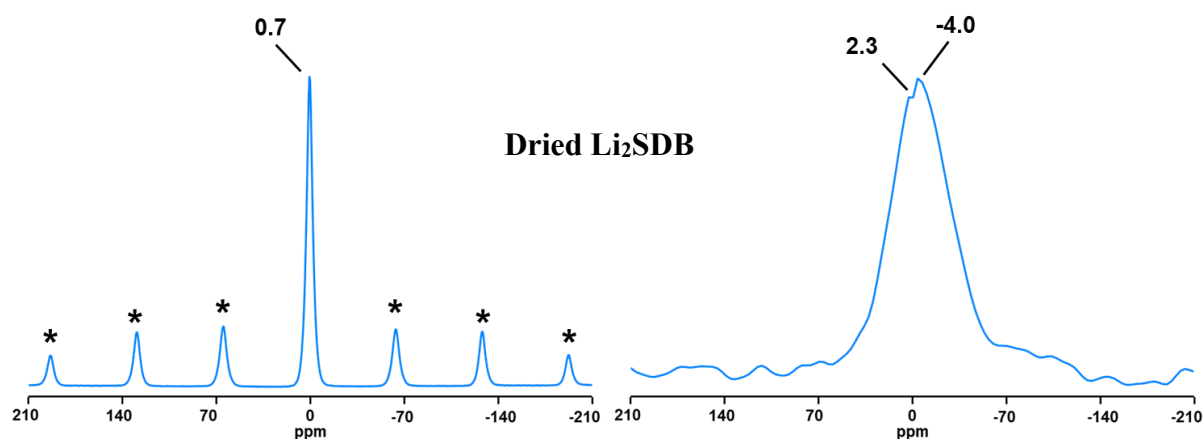


Figure 2-18 ^7Li MAS and static NMR spectra of Li_2SDB (* indicates spinning sidebands)

Figure 2-19 gives the ^{23}Na MAS NMR spectra of as-made and activated Na_2SDB . Within Na_2SDB , two crystallographically distinct Na sites are included in each unit cell. In this case, the resonances belong to at least two Na sites in ^{23}Na MAS NMR spectrum. Although three distinct resonances can be observed in the ^{23}Na MAS NMR spectrum of as-made Na_2SDB and two distinct resonances can be observed in the ^{23}Na MAS NMR spectrum of activated Na_2SDB , it is hard to assign separated resonances because of the typical second-order quadrupolar powder patterns. ^{23}Na 2D 3Q MAS was performed to obtain higher-resolution spectra (**Figure 2-20**).

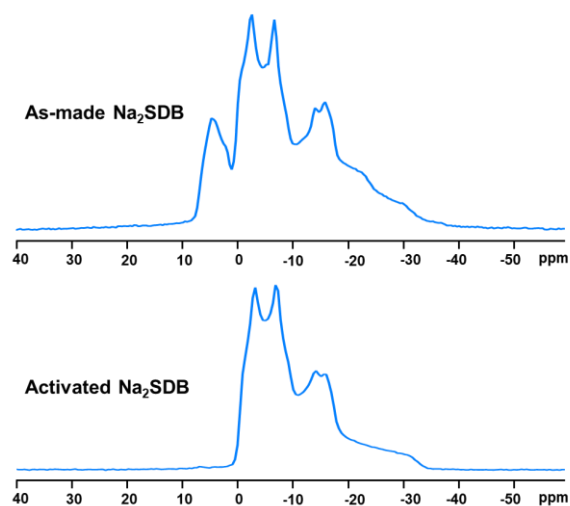


Figure 2-20 Experimental ^{23}Na MAS NMR spectra of as-made and activated Na_2SDB .

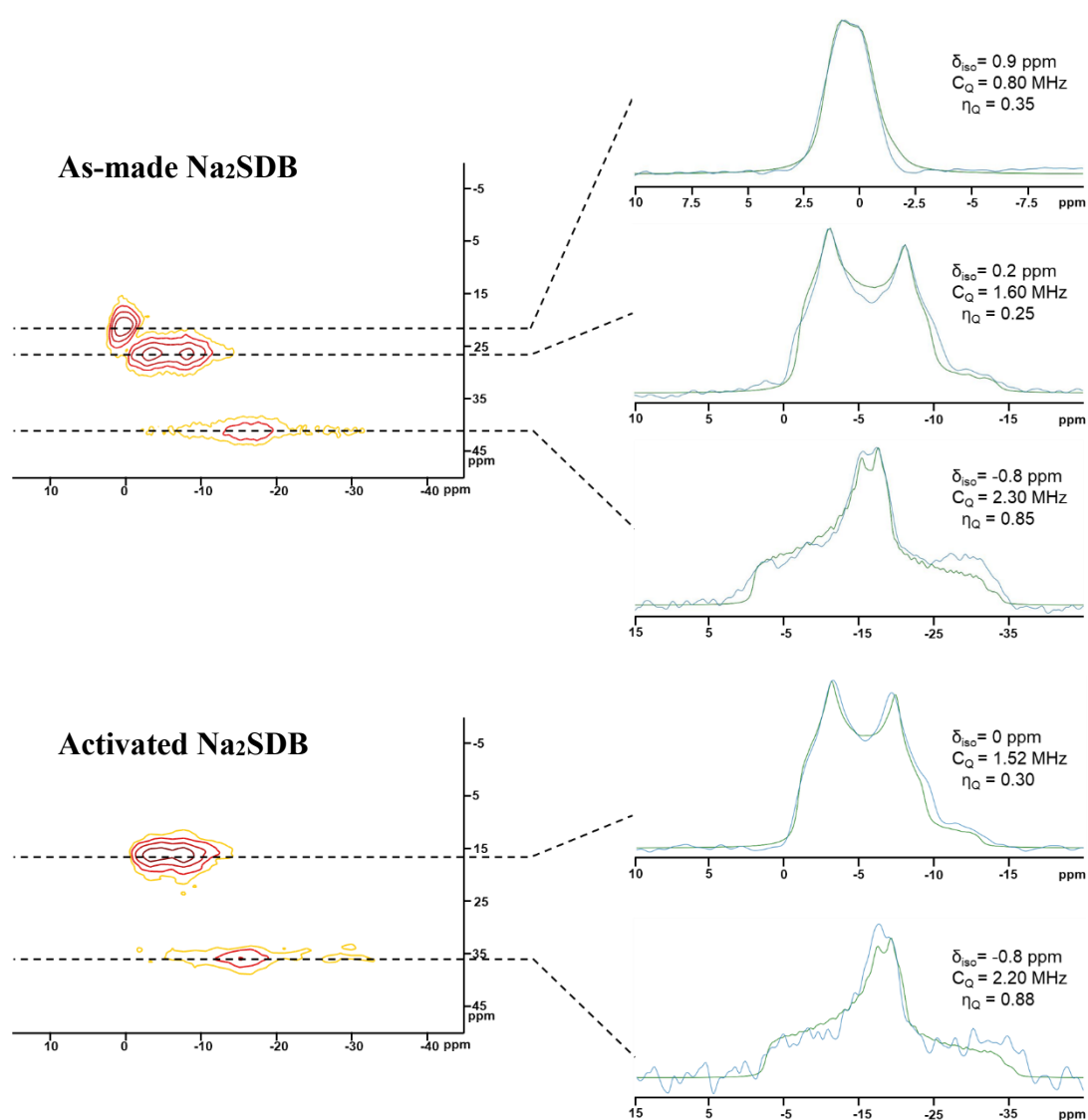


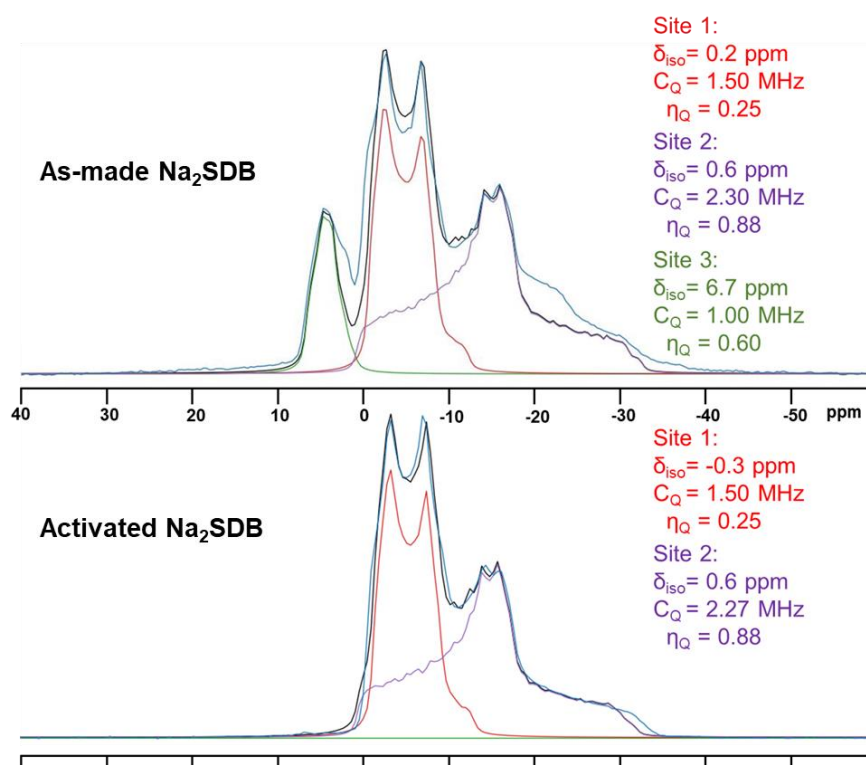
Figure 2-19 ^{23}Na 2D 3Q MAS NMR spectra of as-made and activated Na_2SDB .

With the help of 2D 3Q MAS, the second-order quadrupolar interaction can be eliminated and the isotropic peaks for individual sites can be clearly resolved. Additionally, every ^{23}Na 1D MAS pattern for each distinct Na site can be extracted from ^{23}Na 2D 3Q MAS spectra. According to the simulation of the ^{23}Na 2D 3Q MAS spectra, the normal MAS spectra can be easily simulated.

The simulated ^{23}Na MAS NMR spectra of as-made and activated Na_2SDB are exhibited in **Figure 2-21**, and the ^{23}Na MAS NMR parameters are listed in **Table 2-5**. In the ^{23}Na MAS NMR spectrum of as-made Na_2SDB , three resonances are observed at 0.2(1) ppm, 0.6(1) ppm and 6.7(1) ppm. The resonances with chemical shift at 0.2(1) ppm (site 1) and 0.6(1) ppm (site 2) are belonging to two independent Na sites that are originally in Na_2SDB , since these two resonances are still observed in the spectrum of activated Na_2SDB with similar chemical shift, C_Q and η_Q . According to the C_Q values of site 1 and site 2 (1.50(5) MHz and 2.30(5) MHz), it can be concluded that Na site corresponding to site 2 is much more geometrically asymmetric than the other one. In such case, the resonance with C_Q value of 2.30(5) MHz is likely associated with Na(2), where Na(2) is five-coordinated with four oxygen atoms from four different SDB ligands and one oxygen atom from sulfonyl groups. There will be an available position that allows the interaction between Na(2) sites and the guest molecules, which can explain the existence of the extra resonance at 6.7(1) ppm (site 3) in the spectrum of as-made Na_2SDB , which disappears after activation. The resonance with C_Q value of 1.50(5) MHz is then associated with the Na(I) which is octahedrally coordinated. Additionally, in the spectrum of as-made Na_2SDB , the integrals ratio of these three resonances is approximately 1.00 : 0.75 : 0.25. It proves that Na(1) and Na(2) are equally populated within the pure structure, but with the interactions between the solvent molecules (water, ethanol or DMF) and a small number of Na(2) sites, an extra resonance is resulted. After the removal of the guest molecules, site 1 and site 2 back to equal in their intensities in in the spectrum of activated Na_2SDB .

Table 2-5 Simulated ^{23}Na MAS NMR parameters for as-made and activated Na_2SDB .

MOFs	site	δ_{iso} (ppm)	C_Q (MHz)	η_Q	intensity ratio
as-made Na_2SDB	site 1	7.0(1)	1.50(5)	0.50(1)	1.0
	site 2	1.0(1)	1.55(5)	0.40(1)	1.0
	site 3	-2.0(1)	1.80(5)	0.70(1)	0.9

**Figure 2-21** Simulated ^{23}Na MAS NMR spectra of as-made and activated Na_2SDB .

^{133}Cs and ^{25}Mg MAS NMR spectra of dried Cs_2SDB and as-made MgSDB are exhibited in **Figure 2-22**. All simulated ^{25}Mg MAS NMR parameters are listed in **Table 2-6**. A single peak (34.1 ppm) is found in the ^{133}Cs MAS NMR spectrum with 5 kHz spinning rate and a single peak (31.8 ppm) is found in the ^{133}Cs MAS NMR spectrum with 20 kHz. Several spinning sidebands are observed in both ^{133}Cs MAS NMR spectra. This result is consistent with the structure where only one independent Cs site is included in Cs_2SDB . For as-made MgSDB , the peaks in the ^{25}Mg MAS NMR spectrum give detailed information. Three separated

resonances with chemical shift of 7.0(1) ppm 1.0(1) ppm and -2.0(1) ppm represent three independent Mg sites within as-made MgSDB, which is consistent with the structure obtained from X-ray diffraction.³ For all three sites, C_Q values are close (1.50(5) MHz for site 1, 1.55(5) MHz for site 2 and 1.80(5) MHz for site 3), which suggests the similar local geometry of those three sites. The Mg-O bonds between Mg sites and carboxylate groups are approximately 2.09(1) Å; the Mg-O bonds between Mg sites and bridging OH groups are around 2.05(1) Å; the Mg-O bonds between Mg sites and coordinated water molecules are around 2.12(1) Å; and the Mg-O bonds between Mg sites and coordinated ethanol molecules are around 2.12(1) Å as well. In this case, the peak with C_Q value of 1.50(5) is likely associated with the Mg(2) which is six coordinated with four carboxylate groups and two bridging OH groups, since it has relatively highest symmetry among the three sites. Due to Mg(1) and Mg(3) being relatively lower symmetric with coordinated water and ethanol molecules, they result in peaks with C_Q values of 1.55(5) and 1.80(5), respectively. However, all three peaks assigned in the ^{25}Mg MAS NMR spectrum are not accurate enough. With the help of ^{25}Mg 2D 3Q NMR for both as-made and activated MgSDB in future, a better characterization on MgSDB can be achieved.

Table 2-6 Simulated ^{25}Mg MAS NMR parameters for as-made MgSDB.

Site	δ_{iso} (ppm)	C_Q (MHz)	η_Q	Intensity ratio
Site 1	7.0(1)	1.50(5)	0.50(1)	1.0
Site 2	1.0(1)	1.55(5)	0.40(1)	1.0
Site 3	-2.0(1)	1.80(5)	0.70(1)	0.9

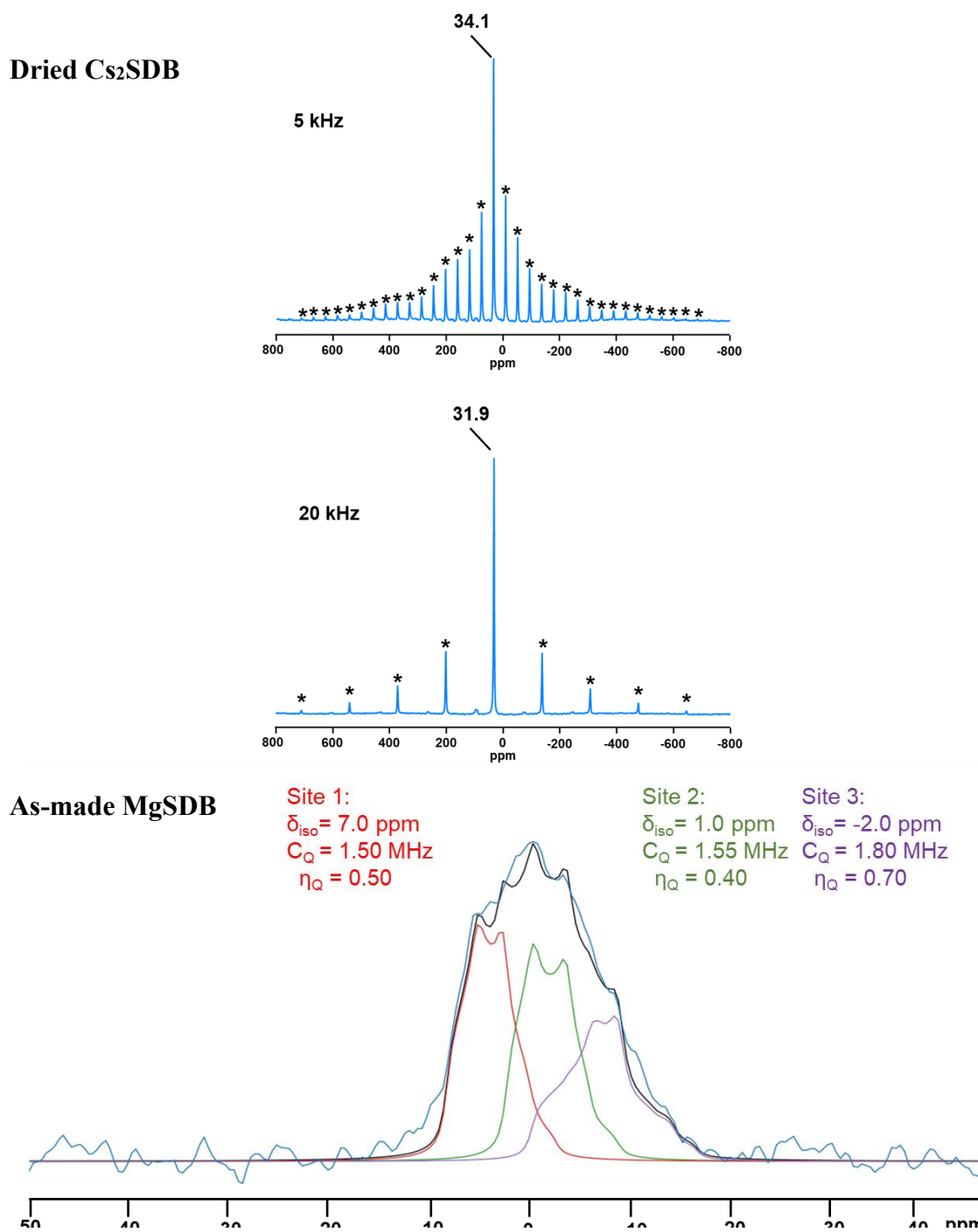


Figure 2-22 ^{133}Cs MAS NMR spectra of dried Cs₂SDB with spinning rate 5 kHz and 20 kHz (top) (* indicates spinning sidebands) and ^{25}Mg MAS NMR spectrum of as-made MgSDB.

2.4 Conclusion

PXRD patterns and TGA graph provided a rough characterization of all six MOFs, confirming all six s-block metal MOFs based on SDB were successfully synthesized.

Compared with PXRD patterns, ^{13}C CPMAS NMR spectra provide more detailed information on the ligands. Whether the porous channel is completely empty was much easier to be analyzed with ^{13}C MAS CPNMR spectra compared with TGA. The multiple peaks of C1 and C5 are caused by the multiple crystallographically distinct C1 and C5 atoms within one unit cell. Asymmetric SDB ligand or inequivalent SDB ligands in one unit cell can both lead to multiple C1 and C5 atoms. The structures of all the s-block MOFs except as-made MgSDB are different from those obtained from X-ray diffraction, where the inversion center symmetry elements are absent. The structures of Na₂SDB before and after activation are unchanged but a small amount of DMF remains in the rigid channels. The structure transforms with decreased crystallinity during activation were proved in MgSDB. No major changes were observed between ^{13}C CPMAS NMR spectra of as-made and activated CaSDB. The ^{13}C CPMAS NMR spectra of SrSDB exhibit a signal shift on the C1 site after activation. With the help of ^7Li , ^{23}Na , ^{133}Cs and ^{25}Mg NMR, the structure of Li₂SDB, Na₂SDB, Cs₂SDB and MgSDB were further characterized, and the local environments of metal centers were studied. Within Na₂SDB, the coordination mode of Na site is proved that Na(1) is six-coordinated, and Na(2) is five-coordinated. The ^{25}Mg MAS NMR spectrum of as-made MgSDB exhibits that the structure is consistent with the one obtained from the X-ray diffraction. For both Li₂SDB and Cs₂SDB, it is hard to tell if the same structure as that discussed in the published paper is observed.

2.5 Reference

1. D. Banerjee, L. Borkowski, S. Kim & J. Parise. Synthesis and Structural Characterization of Lithium-Based Metal-Organic Frameworks. *Crystal Growth & Design*, 2009, **9(11)**, 4922-4926.
2. D. Raja, J. Luo, C. Wu, Y. Cheng, C. Yeh, Y. Chen, S. Lo, Y. Lai & C. Lin. Solvothermal Synthesis, Structural Diversity, and Properties of Alkali Metal–Organic Frameworks Based on V-shaped Ligand. *Cryst. Growth Des.* 2013, **13**, 3785–3793.
3. C. Wu, D. Raja, C. Yang, C. Yeh, Y. Chen, C. Li, B. Ko & C. Lin. Evaluation of structural transformation in 2D metal-organic frameworks based on a 4,4'-sulfonyldibenzoate linker: microwave-assisted solvothermal synthesis, characterization and applications.

CrystEngComm, 2014, **16**, 9308.

4. T. Kundu, S. Sahoo & R. Banerjee. Alkali earth metal (Ca, Sr, Ba) based thermostable metal-organic frameworks (MOFs) for proton conduction. *Chem. Commun.*, 2012, **48**, 4998–5000.
5. D. Dawson, L. Jamieson, M. Mohideen, A. Mckinlay, I. Smellie, R. Cadouo, N. Keddie, R. Morris & S. Ashbrook. High-resolution solid-state ^{13}C NMR spectroscopy of the paramagnetic metal–organic frameworks, STAM-1 and HKUST-1. *Phys. Chem. Chem. Phys.*, 2013, **15(3)**, 919-929.
6. D. Evans, M. Huang, M. Seganish, J. Fettinger & T. Williams. Synthesis, Structures, and Solution Behavior of Bis(sulfoxide)-Pincer Complexes of Palladium(II). *Organometallics*, 2002, **21(5)**, 893–900.
7. B. Ye, X. Li, I. Williams & X. Chen. Synthesis and Structural Characterization of Di- and Tetranuclear Zinc Complexes with Phenolate and Carboxylate Bridges. Correlations between ^{13}C NMR Chemical Shifts and Carboxylate Binding Modes. *Inorg. Chem.* 2002, **41(24)**, 6426–6431.
8. S. Chen, B. E. G. Lucier, M. Chen, V. V. Terskikh & Y. Huang. Probing Calcium-Based Metal-Organic Frameworks via Natural Abundance ^{43}Ca Solid-State NMR Spectroscopy. *Chem. Eur.J.* 2018, **24**, 8732–8736.

Chapter 3

3. Exploring the dynamics and adsorption of $^{13}\text{CO}_2$ in four porous SDB MOFs using VT ^{13}C static SSNMR

3.1 Introduction

3.1.1 Climate change

“Climate change” refers to the change of weather patterns within a long-term period in one region, which includes the wind pattern shift, increasing or decreasing average temperature and the change in the amount of precipitation. The causes of climate change is divided into two parts, natural cause, and human causes. In the past, the earth’s climate is mainly controlled by natural causes, while in recent decades, human causes had risen to dominate climate change. The rising temperatures, also known as “global warming”,^{1,2} is induced by the huge increase of greenhouse gases. The climbing temperature has a significant impact on humans’ daily life, such as the extreme weather on higher frequency and intensity, as well as geological changes, such as the rising of sea levels, ice sheets melting and noticeable ocean acidification.³

Greenhouse gases can adsorb and maintain the infrared radiation from the sun and the reflected radiation from the ground, which is the reason why the earth can keep itself warm. However, excessive greenhouse gases are the reason for causing “global warming”. Normally, water vapor (H_2O), carbon dioxide (CO_2), methane (CH_4), nitrous oxide (N_2O) and ozone (O_3) are considered as the “greenhouse gases”.⁴

3.1.2 CO_2 emission

Carbon dioxide (CO_2), one of the greenhouse gases, is the largest contributor to global warming. To meet the daily demands of humans, the remarkable CO_2 emission is induced from several perspectives. For instance, Transportation contributes approximately 29% of CO_2 emissions, electricity generation makes up nearly 27.5% and followed by industry operation with 22%.⁵ The dramatically increased number of factories have been built to meet the need for fast society development, but the old fashion energy sources, such as carbon-based fossil fuels, are still being utilized by most factories, such as power plants, which results in

uncontrollable CO₂ emission. Before the industrial revolution, around the late 19th century, the global mean CO₂ concentration was approximately 280 ppm; however, it hit 417 ppm on the latest measurement on April 2022 according to National Oceanic and Atmospheric Administration (NOAA) (**Figure 3-1**).⁶ Additionally, it was found that CO₂ emission has a significant influence on food production, economic growth and energy utilization as well.⁷

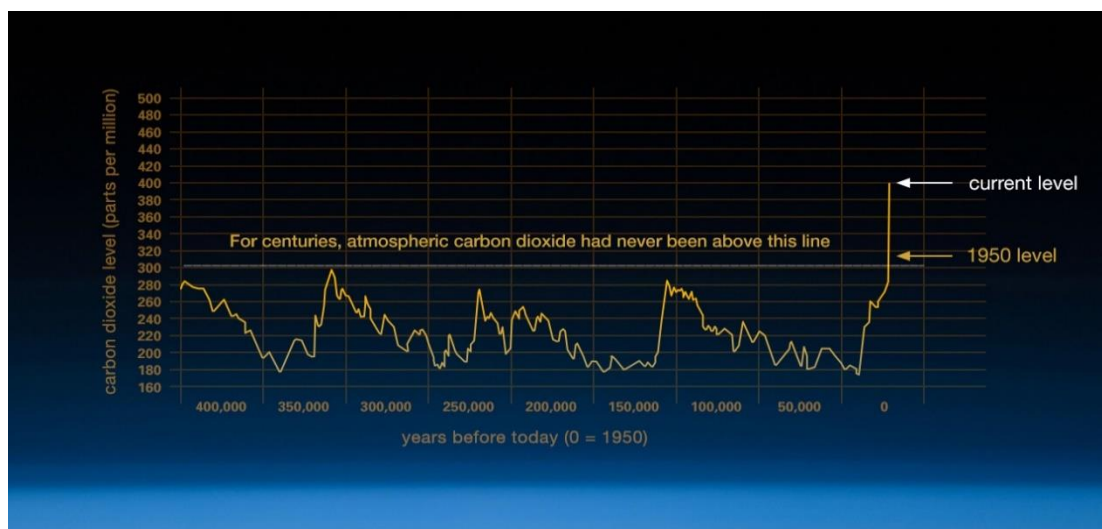


Figure 3-1 Global atmospheric CO₂ level.⁶

3.1.3 Carbon capture and storage (CCS)

Carbon capture and storage (CCS) is then escalating to become a significant social problem that needs to be solved world-wide collaboratively. The methods applied should be economical, efficient, and effective.⁸ The traditional CO₂ adsorbents, using Aqueous alkanolamine solutions, have been applied for decades. Generally, monoethanolamide (MEA) and triethanolamine (TEA) are used, which interact with CO₂, composing carbamate or bicarbonate species (**Figure 3-2**).⁸ the adsorption performance of this method is considered as the standard, where 30 wt% MEA solution can adsorb nearly 2.1-5.5 wt% CO₂ while TEA has better performance. However, it is worth mentioning that the maximum loading capacity for CO₂ is significantly influenced by the stoichiometry of the reactions since the primary secondary and tertiary amine have different interaction ratios with CO₂ (2:1 for primary amine and 1:1 for secondary and tertiary amine). Despite the high adsorption capacity of CO₂ within aqueous alkanolamine solutions, there are also several drawbacks that cannot be avoided. Firstly, the energy required to desorb CO₂ is noticeably high since the tight interaction. Additionally, the aqueous alkanolamine

solutions are corrosive and unstable under heat. With the decomposition over time, the lifespan is dramatically shortened, especially in industry.⁹

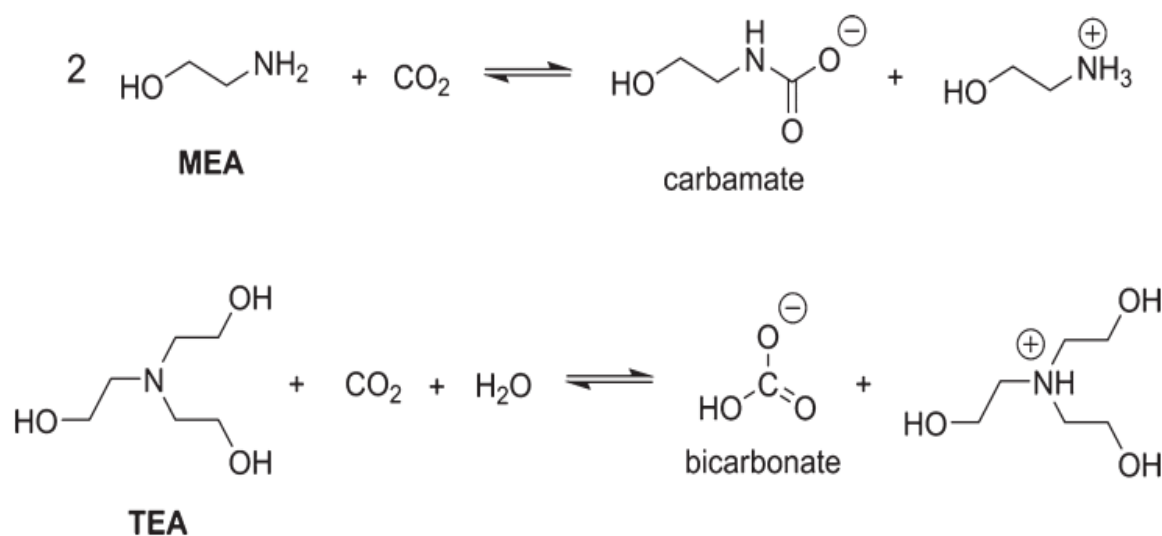


Figure 3-2 The scheme of CO₂ capture in Aqueous alkanolamine solutions.

3.1.4 CO₂ adsorption in MOFs

For this reason, metal-organic frameworks (MOFs) are considered as new materials that capture the CO₂ before emitting it into the atmosphere, because of their reusability and wide applications with low energy cost. Moreover, most MOFs are not corrosive and have remarkable CO₂ adsorption capacity. For instance, the well-known MOF, MIL-53(Al), has a CO₂ capacity of 10.4 mol/kg at 30 bar and 304 K;⁹ MIL-101 (Cr) shows a CO₂ capacity of about 18 mol/kg at 50 bar and 304 K and it shows even higher capacity when activated with ethanol and NH₄F, which increased to 40 mol/kg under the same condition.¹⁰ Additionally, gas selection can also be performed by MOFs giving the reason for the specific pore size.

3.2 Experimental

3.2.1 MOFs synthesis and activation

All four SDB MOFs (Na₂SDB, MgSDB, CaSDB and SrSDB) were synthesized and activated according to the same scheme as listed in chapter 3.

3.2.2 ^{13}C loading

Since ^{13}C natural abundance is only 0.96%, to observe ^{13}C resonances specifically from $^{13}\text{CO}_2$ rather than the framework, 99% isotopically labeled $^{13}\text{CO}_2$ gas was used. To empty the pore of MOFs for CO_2 loading, about 120 mg samples are prepared on the horizontal bottom of an L-shaped glass tube. A small amount of glass wool was used to make sure the sample was tightly packed. After activation (using the activation scheme above), a certain amount of pure ^{13}C enriched $^{13}\text{CO}_2$ in a round bottom flask was introduced into the vacuum line with the vacuum line isolated from either vacuum or air. Then using liquid nitrogen surround the L-shape glass tube to condense and trap $^{13}\text{CO}_2$, followed by the flame-sealing under vacuum. Approximately 0.2 moles of $^{13}\text{CO}_2$ per mole of metal in MOFs was used in this experiment.

3.2.3 ^{13}C static SSNMR

For static ^{13}C SSNMR, a Varian Infinity Plus 400 spectrometer that operated with an Oxford 9.4 T magnet and a Varian/Chemagnetics 5mm HX static probe were used. The CO_2 adsorption behavior can be probed by a variable-temperature study from 133 K to 373 K using a Varian VT temperature control unit calibrated by ^{207}Pb chemical shift of solid $\text{Pb}(\text{NO}_3)_2$. Ethanol was used as the reference for chemical shift ^{13}C , where the methylene carbon of ethanol was set at 56.83 ppm from tetramethylsilane (TMS).

Depth-echo sequences without decoupling were applied to acquire all ^{13}C spectra. 90° pulse length (pw90) was set at around $3.3\mu\text{s}$ (optimized each time), pulse delay was set at 3s and $40\mu\text{s}$ for τ_1 while $20\mu\text{s}$ for τ_2 . Every spectrum has approximately 1000 scans except the one under room temperature (293K), which is nearly 10000 scans.

3.3 Results and discussion

To obtain more information on the dynamics of CO_2 adsorbed within four porous SDB MOFs, *in situ* ^{13}C VT SSNMR experiments at temperatures ranging from 373 to 173 K were performed.

3.3.1 *in situ* ^{13}C VT SSNMR of Na_2SDB with $^{13}\text{CO}_2$

In **Figure 3-3**, the resulting experimental and analytically simulated spectra are exhibited.

Two distinct sites are featured from the experimental ^{13}C VT SSNMR spectra obtained at temperatures from 173 to 373 K (**Figure 3-3a**), as proved by the analytical simulations (**Figure 3-3b**). The sharp and intense resonance (site 1) can be clearly found around 124 ppm, which is induced from mobile CO_2 in the gas or liquid phase outside of the frameworks; while the underlying ^{13}C powder pattern is broadened by a considerable amount of chemical shift anisotropy (CSA) because of the slowed motion of CO_2 . The second simulated powder pattern

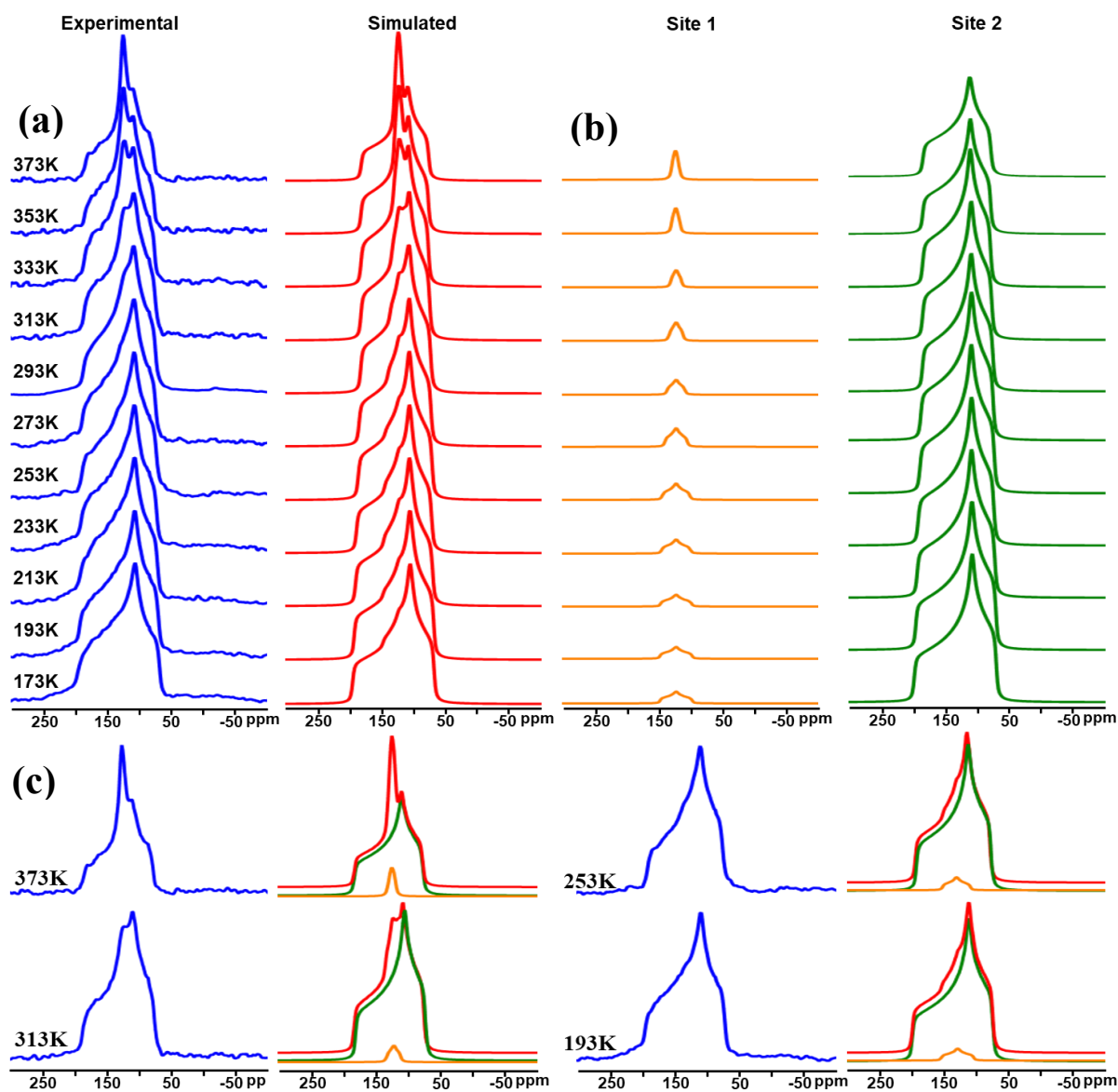


Figure 3-3 (a). The experimental (blue) and simulated (red) static ^{13}C VT SSNMR spectra of Na_2SDB loaded with 0.2 mole $^{13}\text{CO}_2$ per mole of Na. (b). The specific patterns for free (orange) and adsorbed (green) $^{13}\text{CO}_2$. (c). Comparison of experimental and stacked simulated patterns.

(site 2) corresponds to $^{13}\text{CO}_2$ adsorbed within MOFs, which is largely influenced by temperature.

As known that CO_2 is changing to the solid phase when the temperature decreases to 195K at 1 atm, it is not clear if there are still central resonances for free CO_2 in spectra obtained under 173 K and 193 K since the intensities of these patterns are extremely small. As temperature decreases, the increasing intensity of the broad powder pattern suggests the majority of CO_2 is adsorbed within Na_2SDB , and the broadening width demonstrates the reduced CO_2 mobility, confirming the interaction among CO_2 and Na_2SDB .

The NMR parameters of the resonances associated with adsorbed $^{13}\text{CO}_2$ in Na_2SDB are listed in **Table 3-1**. The span value of the resonance associated with adsorbed CO_2 within Na_2SDB steadily broadens from 106(1) ppm at 373 K to 128(2) ppm at 173 K, which is largely less than the span value of the pattern related to static CO_2 (335 ppm)¹². This observation suggests that the CO_2 within Na_2SDB is neither static nor totally mobile, and CO_2 undergoes a reduced motion as temperature decreases. Additionally, the skew values of the adsorbed CO_2 associated resonances remain consistent with slight fluctuations under various temperatures.

To obtain deeper information on CO_2 motion, the EXPRESS software package was used to simulate the spectra as well. The CO_2 motional data obtained from the EXPRESS simulation are listed in **Table 3-1** and they fit experimental spectra well (**Figure 3-4a**). According to the motional data, CO_2 undergoes two types of motion within Na_2SDB framework, localized rotation upon adsorption sites (threefold (C_3) wobbling) and twofold (C_2) non-localized hopping between two equivalent adsorption sites. The angle between the CO_2 molecule and the C_3 wobbling axis is defined as α , and the β denotes the equivalent rotation angle for C_2 hopping, as shown in **Figure 3-4b**. It is worth mentioning that all wobbling rotations with more than 3 folds will result in the same powder pattern.

The CO_2 motional rates at all temperatures are in a fast motion regime. With the temperature increasing, the α value slightly increases from 23(1) $^\circ$ to 33(1) $^\circ$, which indicates that CO_2 is wobbling with a larger angle and occupying a larger volume of space within the channels when more thermal energy is given to compete with CO_2 -framework interaction. The similar CO_2 wobbling angle changes within Na_2SDB were observed compared with that within

either MIL-53 or MOF-74,^{13,14} Additionally, the hopping angle stays unchanged with increased temperature, which confirms the orientation of CO₂ and the interaction type between CO₂ and the framework of Na₂SDB are not altered significantly under various temperatures.

Table 3-1 The static ¹³C SSNMR parameters of adsorbed ¹³CO₂ associated resonance and the CO₂ motional data of adsorbed ¹³CO₂ in Na₂SDB at various temperature. All motion rates are $\geq 10^7$ Hz

Temperature (K)	Intensity(%)	δ_{iso} (ppm)	Ω (ppm)	κ
373	82	123.0(5)	106(1)	-0.38(1)
353	86	123.0(5)	106(1)	-0.40(1)
333	89	123.0(5)	106(1)	-0.40(1)
313	91	122.0(5)	108(1)	-0.40(1)
293	92	121.5(5)	110(1)	-0.38(1)
273	92	122.0(5)	113(1)	-0.40(1)
253	94	122.0(5)	116(1)	-0.38(1)
233	92	123.0(5)	118(2)	-0.41(1)
213	91	123.0(5)	121(2)	-0.40(1)
193	94	123.0(5)	125(2)	-0.40(1)
173	94	123.5(5)	128(2)	-0.41(1)

Temperature (K)	α (C ₃ wobbling angle, °)	β (C ₂ hopping angle, °)
373	33(1)	40(1)
353	33(1)	40(1)
333	32(1)	40(1)
313	31(1)	40(1)
293	30(1)	40(1)
273	29(1)	40(1)
253	28(1)	40(1)
233	27(1)	40(1)

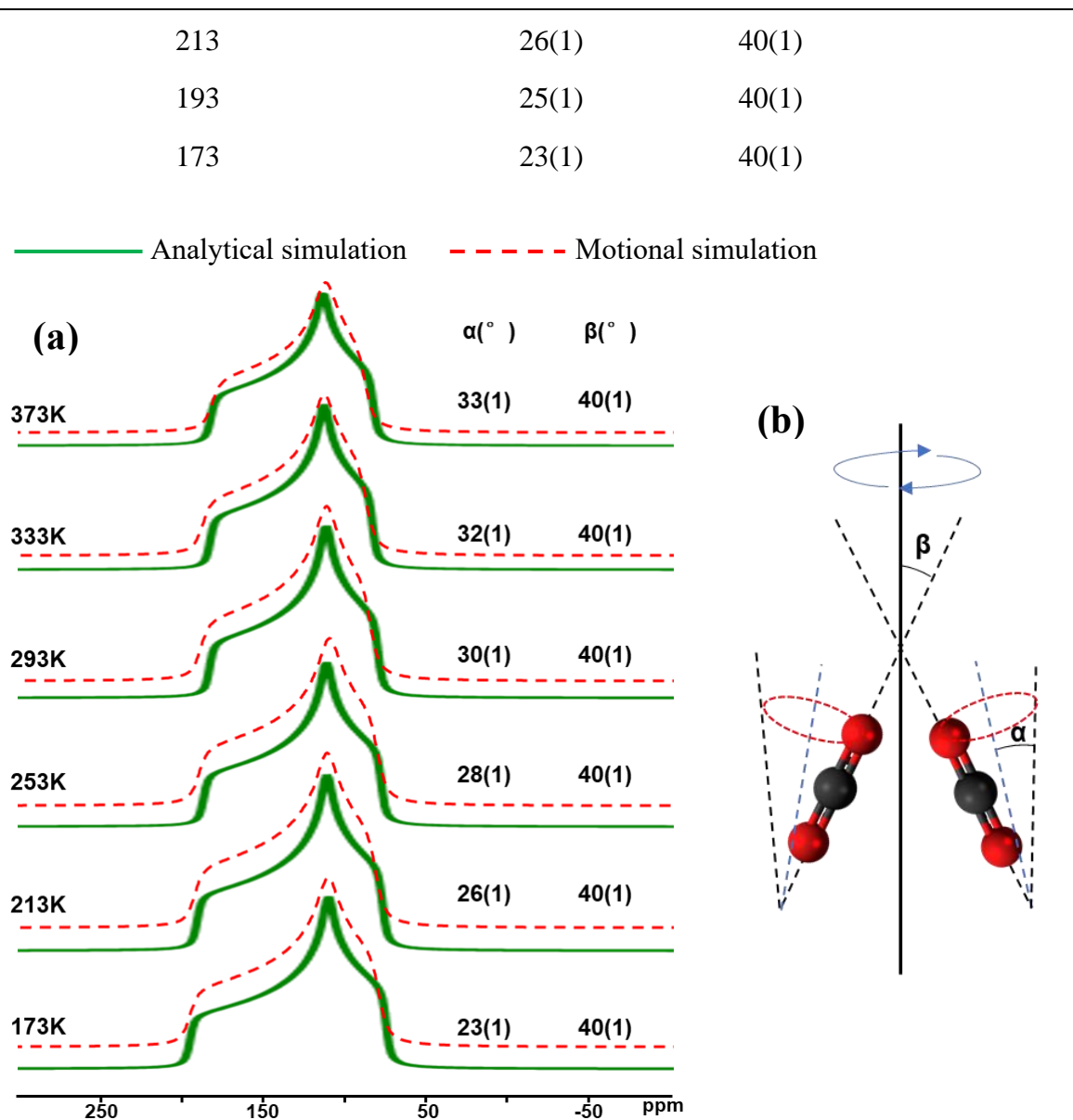


Figure 3-4 (a). Analytical simulated and motional simulated static ^{13}C SSNMR spectra of $^{13}\text{CO}_2$ loaded Na₂SDB, including both threefold wobbling angles (α) and twofold hopping angles (β) at different temperature. (b). The model of CO₂ dynamics in Na₂SDB with both wobbling and hopping.

3.3.2 *in situ* ^{13}C VT SSNMR of MgSDB with $^{13}\text{CO}_2$

Like Na₂SDB, MgSDB contains one adsorption site and there is no open metal site. **Figure 3-5** reveals the experimental and analytically simulated static ^{13}C SSNMR spectra. The

analytical simulation proves the single adsorption site and exhibits a broad powder pattern, corresponding to adsorbed CO_2 . The sharp ^{13}C resonance refers to the mobile, non-adsorbed CO_2 .

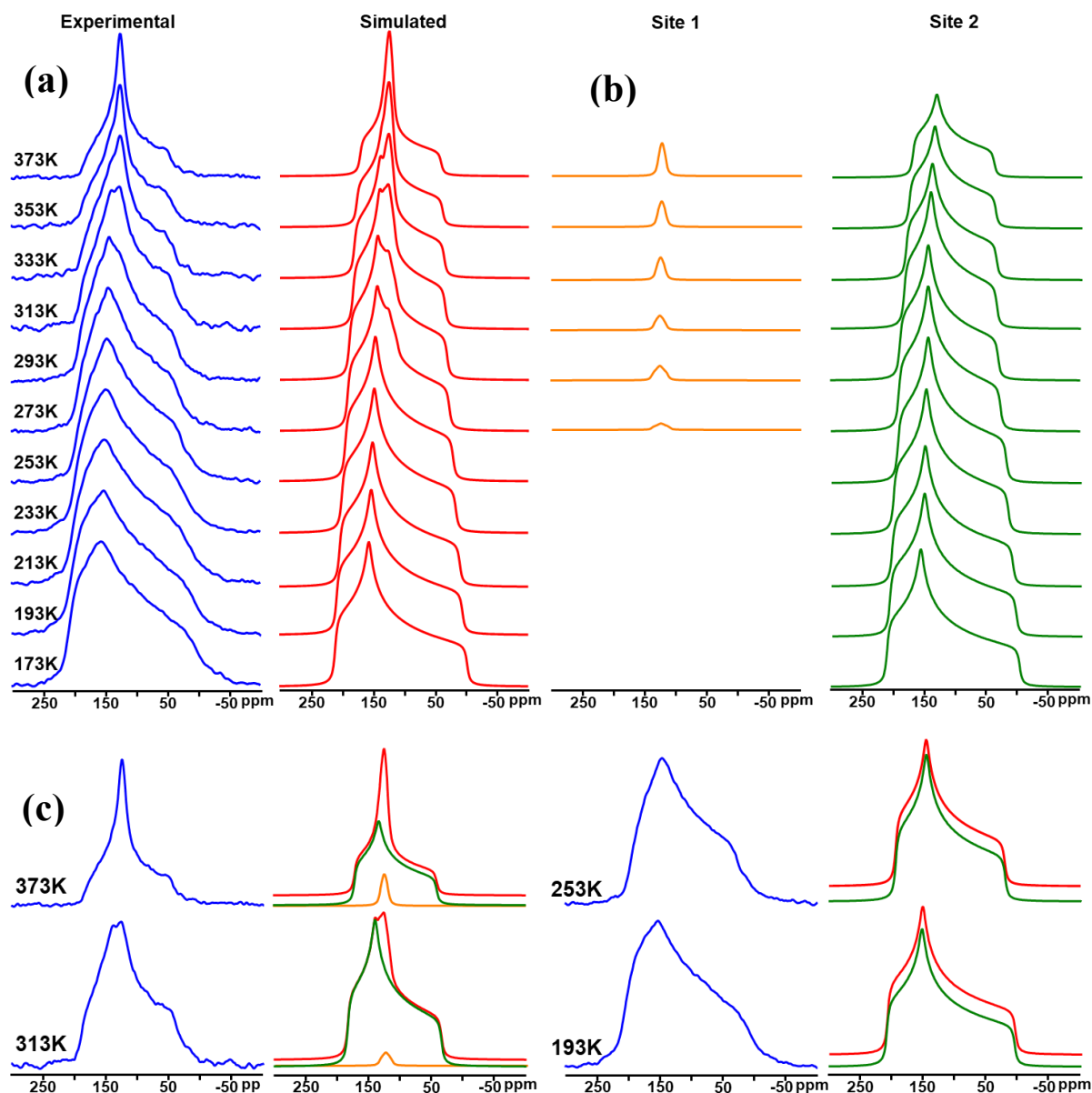


Figure 3-5 (a). The experimental (blue) and simulated (red) static ^{13}C VT SSNMR spectra of MgSDB loaded with 0.2 mole $^{13}\text{CO}_2$ per mole of Mg. (b). The specific patterns for free (orange) and adsorbed (green) $^{13}\text{CO}_2$. (c). Comparison of experimental and stacked simulated patterns.

The static ^{13}C SSNMR parameters are listed in **Table 3-2**. The chemical shift value of adsorbed CO_2 associated resonance clearly moves from 121.5(5) to 115.0(5) and the skew value shifts from 0.49(2) to 0.41(1) at the temperature ranging from 173K to 373K. Meanwhile,

the span values largely increase from 130(1) ppm at 373 K to 212(2) ppm at 173 K, which hints CO₂ is under a tighter interaction with the adsorption site in MgSDB when the temperature decreases. Additionally, the overall span values are much larger than the span values in Na₂SDB (106 ppm – 128 ppm), which can be explained by the significantly restricted motion due to the larger CO₂-framework interaction in MgSDB.

Table 3-2 The static ¹³C SSNMR parameters of adsorbed ¹³CO₂ associated resonance and the CO₂ motional data of adsorbed ¹³CO₂ in MgSDB at various temperature. All motion rates are $\geq 10^7$ Hz.

Temperature (K)	Intensity (%)	δ_{iso} (ppm)	Ω (ppm)	κ
373	80	115.0(5)	130(1)	0.41(1)
353	84	117.0(5)	138(1)	0.41(1)
333	89	119.0(5)	144(1)	0.42(1)
313	91	119.0(5)	148(1)	0.42(1)
293	93	121.0(5)	157(2)	0.42(1)
273	96	121.0(5)	163(2)	0.42(2)
253	100	120.0(5)	173(2)	0.44(1)
233	100	121.0(5)	183(2)	0.43(1)
213	100	121.0(5)	193(1)	0.45(2)
193	100	122.0(5)	202(2)	0.45(2)
173	100	121.5(5)	212(2)	0.49(2)

Temperature (K)	α (C ₃ wobbling angle, °)	β (C ₂ hopping angle, °)
373	36(1)	28(1)
353	35(1)	28(1)
333	34(1)	28(7)
313	33(1)	27(1)
293	32(1)	27(1)
273	31(1)	27(1)

253	30(1)	27(1)
233	29(1)	27.(1)
213	28(1)	27(1)
193	25(1)	26(1)
173	23(1)	26(1)

As simulated by the EXPRESS package, the CO₂ motional data are listed (**Table 3-2**) with the comparison of spectra of analytical simulation and motional simulation (**Figure 3-6**). Similar to the CO₂ dynamic behaviors in Na₂SDB, wobbling angle of CO₂ clearly increases with elevating temperature. More space is occupied by CO₂ wobbling in high temperature,

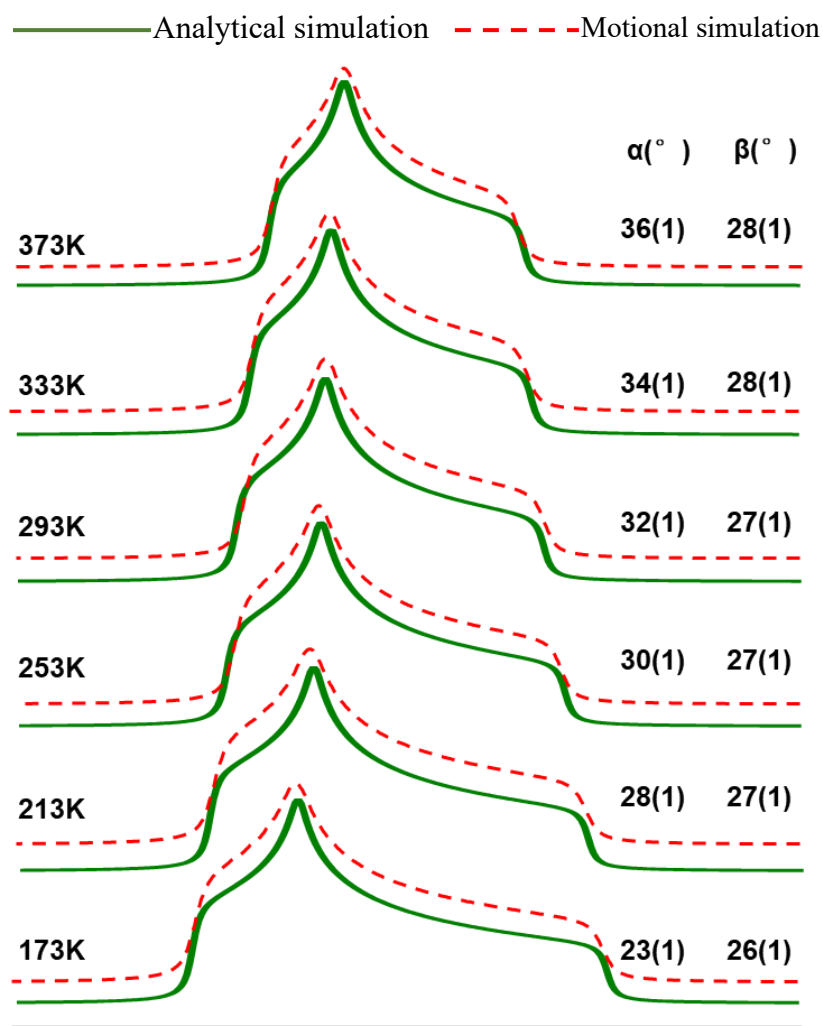


Figure 3-6 Analytical simulated and motional simulated static ¹³C SSNMR spectra of ¹³CO₂ loaded MgSDB, including both threefold wobbling angles (α) and twofold hopping angles (β) at different temperature.

which hints more thermal energy is available to compete with the adsorption interaction among CO₂ molecules and MgSDB framework at the higher temperature. The hopping angle of CO₂ does not have significant change, which decreases from 28(1)° at 373 K to 26(1)° at 173 K, which likely results from the stronger CO₂-framework interaction at lower temperature. As the constant hopping angle value of 40° determined in Na₂SDB, a smaller hopping angle is exhibited in MgSDB, which further proves that MgSDB has smaller porous channels than Na₂SDB and the stronger CO₂-framework interaction exists within MgSDB.

3.3.3 *In situ* ¹³C VT SSNMR of CaSDB and SrSDB with ¹³CO₂

Given the fact that CaSDB and SrSDB have the same structure, the static ¹³C SSNMR spectra of both MOFs are analyzed and exhibited together for a better comparison. The sharp ¹³C resonance (site 1) is observed as well in both static ¹³C SSNMR spectra, corresponding to mobile, non-adsorbed CO₂. However, unlike Na₂SDB or MgSDB, two distinct broad powder pattern (site 2 and site 3) are observed in static ¹³C SSNMR spectra of both CaSDB and SrSDB (**Figure 3-7** and **Figure 3-8**). As confirmed by the analytical simulation, two CO₂ adsorption sites are observed in both CaSDB and SrSDB. Adsorption site 1 and adsorption site 2 are believed to have distinct local geometry and CO₂ binding affinity since their static ¹³C SSNMR parameters differ from each other, as shown in **Table 3-3**.

The parameters of all powder patterns show clear changes as temperature decrease, indicating that adsorbed CO₂ molecules at both sites undergo motional restrictions with altered strength at different temperatures. The changes in skew values for all powder patterns hint the varied adsorption interactions between CO₂ and frameworks as temperature decreases. In the ¹³C SSNMR spectra of CaSDB, the CO₂ molecules have a relatively stronger binding interaction with adsorption site 2 due to its larger span values. However, the adsorption site 1 is more populated than adsorption site 2 under all temperatures measured, since the intensity of the resonance corresponding to adsorption site 1 is larger than that corresponding to adsorption site 2. The observation can be explained by the higher accessibility of adsorption site 1 compared to adsorption site 2. However, the adsorption site 1 and 2 in SrSDB are similar populated, which originates from the similar interaction strength and similar CO₂ accessibility at both adsorption sites within SrSDB.

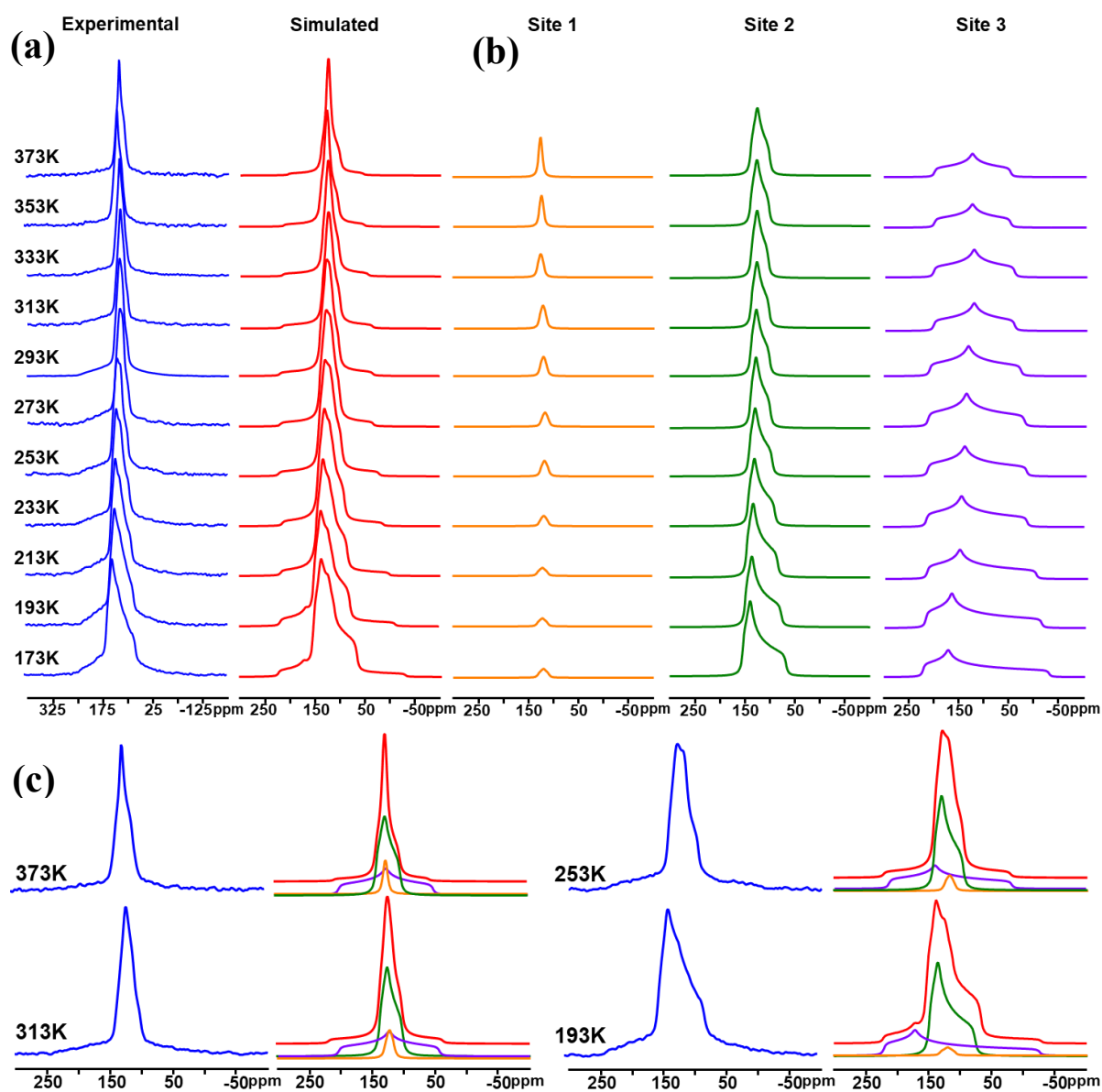


Figure 3-7 (a). The experimental (blue) and simulated (red) static ^{13}C VT SSNMR spectra of CaSDB loaded with 0.2 mole $^{13}\text{CO}_2$ per mole of Ca. (b). The specific patterns for free (orange) and adsorbed (green and purple) $^{13}\text{CO}_2$ at different sites. (c). Comparison of experimental and stacked simulated patterns.

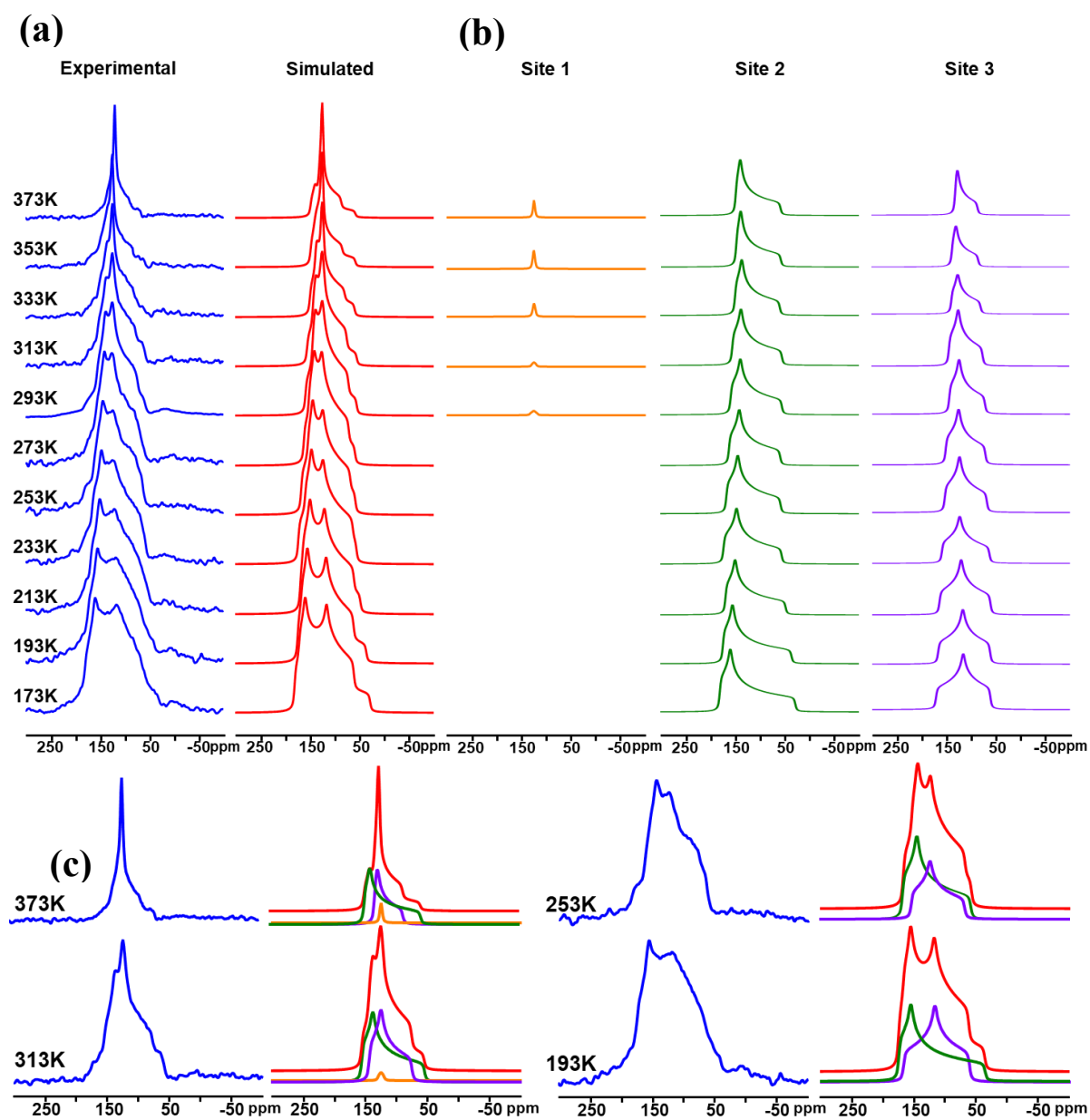


Figure 3-8 (a). The experimental (blue) and simulated (red) static ^{13}C VT SSNMR spectra of SrSDB loaded with 0.2 mole $^{13}\text{CO}_2$ per mole of Sr. (b). The specific patterns for free (orange) and adsorbed (green and purple) $^{13}\text{CO}_2$ at different sites. (c). Comparison of experimental and stacked simulated patterns.

Table 3-3 The static ^{13}C SSNMR parameters of adsorbed $^{13}\text{CO}_2$ associated resonances in CaSDB and SrSDB at various temperature.

MOF	site	Temperature (K)	Intensity (%)	δ_{iso} (ppm)	Ω (ppm)	κ
CaSDB	1	373	53	123.0(5)	33(1)	0.25(1)
		353	55	123.0(5)	34(1)	0.28(1)
		333	56	123.0(5)	35(1)	0.30(1)
		313	56	121.5(5)	36(1)	0.36(1)
		293	58	122.0(5)	38(1)	0.41(1)
		273	63	122.0(5)	40(1)	0.45(1)
		253	65	122.0(5)	48(1)	0.52(1)
		233	65	122.0(5)	53(1)	0.55(1)
		213	66	122.0(5)	62(1)	0.59(1)
		193	66	122.0(5)	72(2)	0.63(1)
	173	70	120.0(5)	86(2)	0.66(1)	
	2	373	19	125.0(5)	140(2)	-0.00(1)
		353	20	125.0(5)	150(2)	-0.00(1)
		333	21	124.0(5)	160(2)	-0.00(1)
		313	25	124.0(5)	170(2)	-0.00(1)
		293	25	124.0(5)	180(2)	-0.10(1)
		273	21	124.0(5)	190(2)	-0.20(1)
		253	23	124.0(5)	195(3)	0.25(1)
		233	23	124.0(5)	200(3)	0.30(1)
		213	23	124.0(5)	215(3)	0.40(1)
193		25	124.0(5)	230(3)	0.55(1)	
173	21	123.0(5)	250(3)	0.60(1)		
SrSDB	1	373	45	115.0(5)	90(1)	0.80(1)

	353	50	115.0(5)	90(1)	0.80(1)
	333	56	115.0(5)	90(1)	0.70(1)
	313	47	116.0(5)	100(1)	0.65(1)
	293	51	117.5(5)	103(1)	0.62(1)
	273	52	120.5(5)	103(1)	0.60(1)
	253	59	123.0(5)	109(1)	0.58(1)
	233	58	125.0(5)	117(1)	0.55(1)
	213	52	122.0(5)	121(1)	0.68(1)
	193	53	121.5(5)	138(2)	0.72(1)
	173	53	122.5(5)	152(2)	0.72(1)
2	373	40	115.0(5)	45(1)	0.80(1)
	353	35	117.0(5)	53(1)	0.70(1)
	333	35	114.5(5)	59(1)	0.56(1)
	313	49	114.5(5)	68(1)	0.45(1)
	293	48	113.5(5)	72(1)	0.45(1)
	273	48	116.0(5)	80(1)	0.35(1)
	253	41	115.0(5)	85(1)	0.30(1)
	233	42	115.0(5)	96(1)	0.25(1)
	213	48	115.0(5)	103(1)	0.15(1)
	193	47	115.0(5)	105(1)	0.05(1)
	173	47	116.0(5)	110(2)	0.00(1)

Table 3-4 The CO₂ motional data of adsorbed ¹³CO₂ in CaSDB and SrSDB at various temperature. All motion rates are $\geq 10^7$ Hz.

MOF	site	Temperature (K)	α (C ₃ wobbling angle, °)	β (C ₂ hopping angle, °)
CaSDB	1	373	48(1)	32(1)
		353	48(1)	32(1)

	333	48(1)	32(1)
	313	48(1)	32(1)
	293	48(1)	32(1)
	273	47(1)	31(1)
	253	47(1)	30(1)
	233	46(1)	28(1)
	213	45(1)	27(1)
	193	44(1)	26(1)
	173	42(1)	25(1)
2	373	29(1)	35(1)
	353	28(1)	35(1)
	333	27(1)	35(1)
	313	26(1)	34(1)
	293	24(1)	33(1)
	273	22(1)	32(1)
	253	21(1)	32(1)
	233	20(1)	31(1)
	213	19(1)	29(1)
	193	16(1)	27(1)
	173	14(1)	25(1)
SrSDB	1	373	43(1)
		353	43(1)
		333	43(1)
		313	42(1)
		293	41(1)
		273	41(1)
		253	40(1)
		233	40(1)
		213	39(1)

	193	37(1)	20(1)
	173	35(1)	20(1)
2	373	48(1)	21(1)
	353	47(1)	23(1)
	333	46(1)	26(1)
	313	45(1)	27(1)
	293	44(1)	28(1)
	273	43(1)	29(1)
	253	42(1)	30(1)
	233	40(1)	31(1)
	213	39(1)	33(1)
	193	38(1)	34(1)
	173	37(1)	35(1)

The ^{13}C VT SSNMR spectra of $^{13}\text{CO}_2$ loaded CaSDB and SrSDB were then simulated using the EXPRESS package to obtain detailed CO_2 motional information (**Figure 3-9, 3-10**). All the motional rates sit in a fast regime. The wobbling angles of CO_2 at two adsorption sites in both CaSDB and SrSDB steadily increase as the temperature ranges from 173 K to 373 K, like the results observed in Na_2SDB and MgSDB . A larger volume is occupied by CO_2 wobbling when more thermal energy is given.

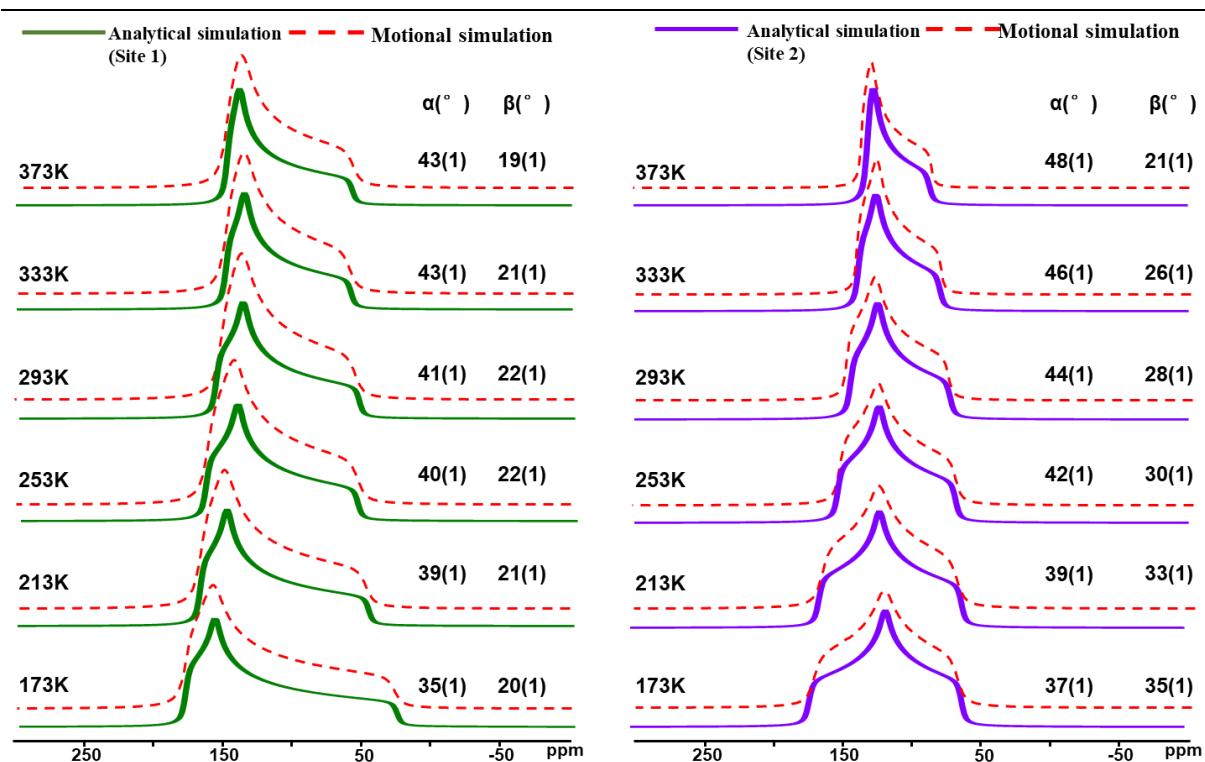


Figure 3-9 Analytical simulated and motional simulated static ^{13}C SSNMR spectra of $^{13}\text{CO}_2$ loaded SrSDB, including both threefold wobbling angles (α) and twofold hopping angles (β) at different temperature.

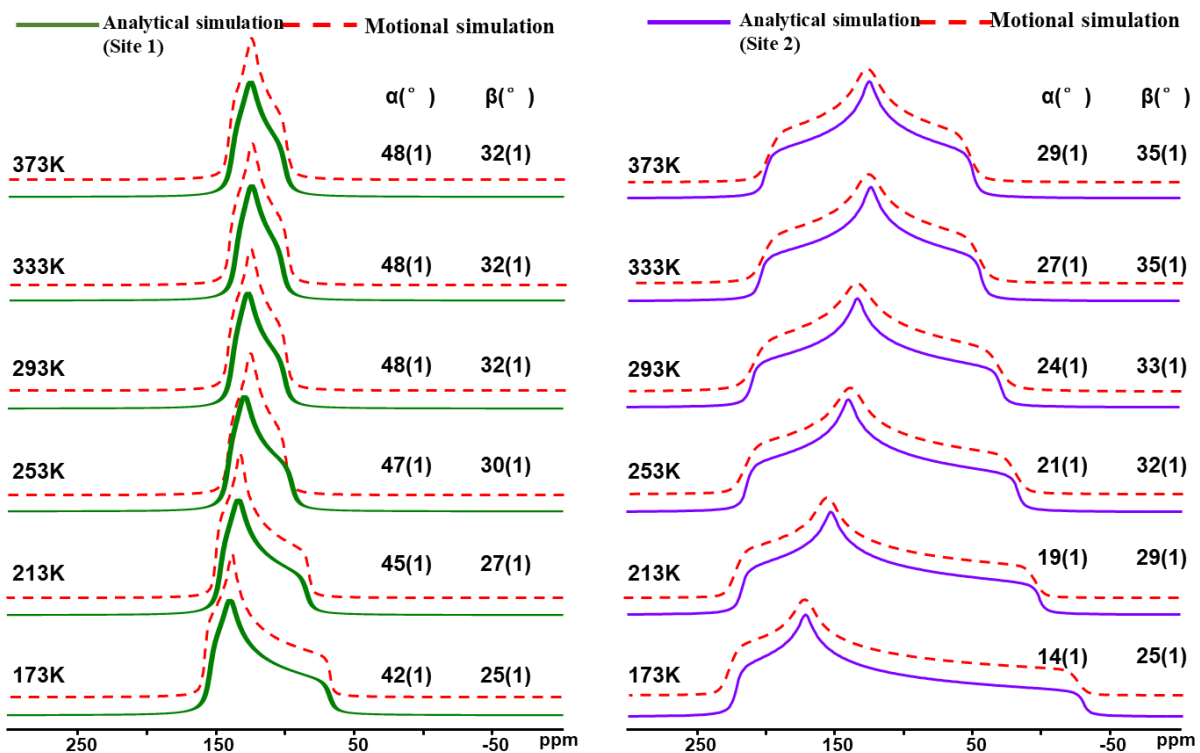


Figure 3-10 Analytical simulated and motional simulated static ^{13}C SSNMR spectra of $^{13}\text{CO}_2$ loaded CaSDB, including both threefold wobbling angles (α) and twofold hopping angles (β) at different temperature.

In CaSDB, the C_2 hopping angles of CO_2 rise from $25(1)^\circ$ at 173 K to $32(1)^\circ$ at 373 K at adsorption site 1, from $25(1)^\circ$ at 173 K to $35(1)^\circ$ at 373 K at adsorption site 2, which is due to the change in the orientation of CO_2 . The similar reduction in hopping angles with increased temperature was observed for guests in the MIL-53 and MOF-74 frameworks.^{13,14} Meanwhile, the hopping angles of CO_2 at adsorption site 1 in SrSDB remain consistent with slight fluctuations at various temperature, which hints the orientation of CO_2 and the interaction type between CO_2 and the adsorption site 1 in SrSDB are not altered significantly under various temperatures. However, the hopping angles of CO_2 at adsorption site 2 in SrSDB show the opposite tendency, which requires more works in future to study the origins for the opposite changing of hopping angles. Specific local adsorption site geometry and MOF topology always influences the CO_2 hopping angles under different conditions.

In shorts, as observed in ^{13}C SSNMR spectra, both CaSDB and SrSDB exhibit two distinct adsorption sites for CO_2 . Although CaSDB and SrSDB have the same structure, they display distinct behaviors on CO_2 adsorption, likely due to the huge impact from the distinct metal centers. Since Ca has much smaller atom radius, the channels within CaSDB will be more crowded than those within SrSDB when CO_2 is loaded.

3.3.4 Comparison of *in situ* ^{13}C VT SSNMR of four SDB MOFs

As all four metals were chosen from s-block, their structures have a common property that there is no open metal site within the porous channel that directly interacts with CO_2 . In such case, the CO_2 adsorption within these four MOFs is mainly physical adsorption. According to the CO_2 adsorption sites within PbSDB and CdSDB that were discussed by Chen,¹⁵ the π -pocket of the SDB linker is presumably the common location for CO_2 adsorption that all four s-block metals-based MOFs shares as well (**Figure 3-11**). The π -interactions between phenyl rings and CO_2 double bonds play the dominant role in CO_2 adsorption in these s-block MOFs based on SDB ligands. It is believed that the common local geometry is found at the adsorption site in Na_2SDB , $MgSDB$, $CaSDB$ (adsorption site 1) and $SrSDB$ (adsorption site 1), given the fact that they exhibit similar wobbling and hopping angle changes. However, due to the distinct electron density and atomic radius of metal center, the frameworks of these MOFs have different degree of crowdedness, which further affect the CO_2 -framework interaction.

As for two alkali earth MOFs (CaSDB and SrSDB), the spans of the powder patterns associated with the π -pocket exhibit a decreasing trend with the larger metal atom. The span value for adsorption site 1 in CaSDB increases from 33(1) ppm at 373 K to 86(1) ppm at 173 K; while the span value for adsorption site 1 in SrSDB starts from 90(1) ppm at 373 K and reaches 152(2) ppm at 173K, which confirms that the larger metal atom in MOFs with the same linker creates the larger porous channel for molecule adsorption, and the smaller channel usually shows the stronger adsorption interaction between CO₂ and MOFs frameworks.

Relying only on ¹³C SSNMR, it is not sufficient to imply where exactly CO₂ is located, especially for CaSDB and SrSDB. However, comparing two adsorption sites in CaSDB and SrSDB, it is obvious that CO₂ molecules adsorbed at site 1 in CaSDB and site 2 in SrSDB have weaker interaction and are less motional restricted, which can be confirmed by the much broader ¹³C powder patterns.

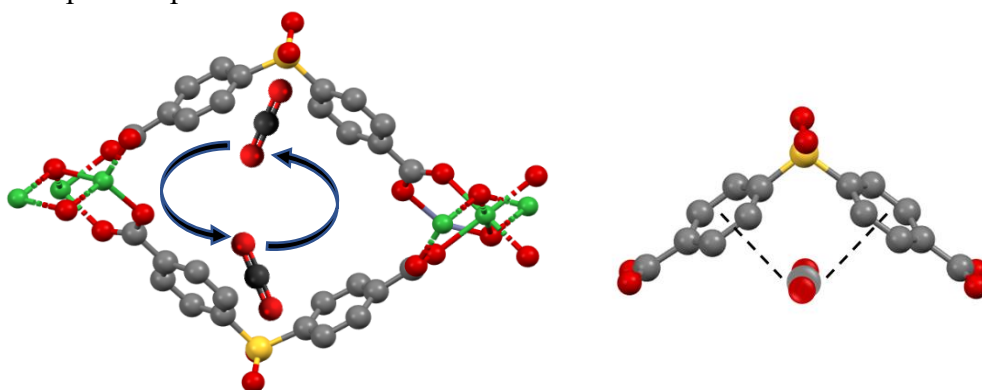


Figure 3-11 The model of CO₂ C₂ hopping within MgSDB as an example (left) and the location of π -pocket (right). (CO₂ molecules are zoomed out for the clearer view of four sites)

3.4 Conclusion

A series of SSNMR experiments have been applied to explore the CO₂ adsorption and dynamics in four SDB MOFs, which do not feature open metal sites or functional groups. The number of adsorption sites and the detailed CO₂ motional data were successfully revealed by the VT ¹³C SSNMR and simulation using Wsolid and EXPRESS. CO₂ was found to undergo a combination of a localized rotation (*C*₃ wobbling) and a non-localized motion (*C*₂ hopping between symmetry-equivalent adsorption sites) in all four SDB linker-based MOFs. Although the detailed information about the locations of the adsorption sites in PbSDB and CdSDB

(transition metals) was already discussed by Chen¹⁵, the specific location of adsorption sites in these four s-block MOFs with SDB linkers still needs future investigation, such as the single crystal x-ray diffraction (SCXRD), since the different properties of the metal atoms.

3.5 Reference

1. M. Leroux. Global warming. *myth or reality*. 2014, **2**.
2. Medhaug, M. Stolpe, E. Fischer & R. Knutti. Reconciling controversies about the ‘global warming hiatuses’. *Nature*, 2017, **545**, 41-47.
3. S. C. Doney, V. J. Fabry, R. A. Feely & J. A. Kleypas. Ocean Acidification: The Other CO₂ Problem. *Annu. Rev. Mar. Sci.* 2009. **1**, 169–92
4. C. Oertel, J. Matschullat, K. Zurba, F. Zimmermann & S. Erasmi. Greenhouse gas emissions from soils— A review. *Chemie der Erde*, 2016, **76**, 327–352.
5. Sources of Greenhouse Gas Emissions. United States Environmental Protection Agency. <https://www.epa.gov/ghgemissions/sourcesgreenhouse-gas-emissions>
6. L. J. Schmidt. Satellite data confirm annual carbon dioxide minimum above 400 ppm. *NASA’s Jet Propulsion Laboratory*, 2017.
7. Rehman, H. Ma, I. Ozturk & R. Ulucak. Sustainable development and pollution: the effects of CO₂ emission on population growth, food production, economic development, and energy consumption in Pakistan. *Environ Sci Pollut Res*, 2022, **29**, 17319–17330.
8. K. Sumida, D. L. Rogow, J. A. Mason, T. M. McDonald, E. D. Bloch, Z. R. Herm & J. R. Long. Carbon dioxide capture in metal-organic frameworks. *Chemical Reviews*, **2012**, *112*, 724–781.
9. K. Sumida, D. L. Rogow, J. A. Mason, T. M. McDonald, E. D. Bloch, Z. R. Herm, T. Bae & J. R. Long. Carbon Dioxide Capture in Metal-Organic Frameworks. *Chem. Rev.* 2012, **112**, *2*, 724–781
10. S. Bourrelly, P. L. Llewellyn, C. Serre, F. Millange, T. Loiseau & G. Férey, Different Adsorption Behaviors of Methane and Carbon Dioxide in the Isotypic Nanoporous Metal Terephthalates MIL-53 and MIL-47. *J. Am. Chem. Soc.*, 2005, **127**, 13519–13521
11. P. L. Llewellyn, S. Bourrelly, C. Serre, A. Vimont, M. Daturi, L. Hamon, G. Weireld, J.

-
- Chang, D. Hong, Y. Hwang, S. Jhung & G. Ferey. High Uptakes of CO₂ and CH₄ in Mesoporous Metal—Organic Frameworks MIL-100 and MIL-101. *Langmuir*, 2008, **24**, 7245–7250.
12. A. J. Beeler, A. M. Orendt, D. M. Grant, P. W. Cutts, J. Michl, K. W. Zilm, J. W. Downing, J. C. Facelli, M. S. Schindler & W. Kutzelnigg, Low-temperature carbon-13 magnetic resonance in solids. 3. Linear and pseudolinear molecules. *J. Am. Chem. Soc.*, 1984, **106**, 7672-7676.
13. Y. Zhang, B. E. Lucier & Y. Huang. Sizable dynamics in small pores: CO₂ location and motion in the α -Mg formate metal–organic framework. *Phys. Chem. Chem. Phys.*, 2015, **8**.
14. W. D. Wang, B. E. Lucier, V. V. Terskikh, W. Wang & Y. Huang. Wobbling and Hopping: Studying Dynamics of CO₂ Adsorbed in Metal–Organic Frameworks via ¹⁷O Solid-State NMR. *J. Phys. Chem. Lett.*, 2014, **5**, 3360-3365.
15. S. Chen, B. E. Lucier, P. D. Boyle & Y. Huang. Understanding The Fascinating Origins of CO₂ Adsorption and Dynamics in MOFs. *Chem. Mater.* 2016, **28(16)**, 5829–5846.

Chapter 4

4. Investigating the dynamics and adsorption of small molecules in MOFs with squarate linker (C₄O₄)

4.1 Introduction

4.1.1 Small molecule storage in MOFs

MOFs have risen to be a promising sorbent for gas adsorption and separation giving the reason of their high surface area and chemically tunable structure. Besides the carbon capture and storage, as one of the effective ways to deal with global warming,¹ acetylene (C₂H₂) storage is also a suitable application which can be implemented by MOFs.

Traditional gas field is still a vital source of energy for daily life and chemical industry. Acetylene (C₂H₂) is widely used due to its high flame temperature, nearly 3000 °C.⁶ However, on the other hand, C₂H₂ is not stable and high risky of explosion, which results the challenge on storage and transportation. For high purity C₂H₂, it can only be compressed under 2 atm since it is possible to explode when above 2 atm. Nowadays, the standard method of C₂H₂ storage is to dissolve it in acetone and save in steel tanks filled with specific porous material, such as diatomaceous earth and firebrick.⁷ In such case, it is worth putting effort on developing the materials that have high capacity for C₂H₂. MOFs is one of the most suitable materials in this field. Cu₂(pzdc)₂(pyz) (pzdc = pyrazine-2,3-dicarboxylate, pyz = pyrazine) is the first MOF tested for C₂H₂ adsorption. With unsaturated carboxyl oxygen atoms in pore surface, it adsorbs 42 cm³/g C₂H₂ at STP, which started the development of MOFs on C₂H₂ adsorption.⁸ Cu₂(DTPD) (ZJU-12, H4DTPD = 5,5'-(2,6-dimethoxynaphthalene-1,5-diyl)diisophthalic acid) was reported, which shows 244 cm³/g C₂H₂ adsorption capacity under 298K and 1 bar. Such high C₂H₂ adsorption capacity is attributed to the open metal sites and optimized pore size.⁹

5.1.1 Gas separation in MOFs

Metal–organic frameworks (MOFs) have also been explored for gas separation and purification. During the CO₂ capture, there is always other gas molecules competing, such as

N₂, O₂ and H₂O. It is not avoidable and dramatically reduces CO₂ adsorption capacity industrially, as the fact that the post-combustion flue gas composition for a coal-fired power plant includes 75% N₂, 6% H₂O and only 15% CO₂.¹ In such case, it is required to implement the MOFs that have high selectively adsorption of CO₂ (kinetic diameter 3.30 Å) over N₂ (kinetic diameter 3.64 Å) even with humid environments. By tuning the pore size and adjusting the interaction between framework and CO₂ quadrupolar moment, many MOFs have demonstrated a high selectivity for CO₂/N₂. CaSDB adsorbs 4.5 wt% CO₂ and only 0.3 wt% N₂ over 1 atm and room temperature;¹⁰ rht-type MOF, [Cu₃(BTB⁶⁻)]_n, shows the 157 wt% CO₂ uptake capacity while only 13% for CH₄ and 11 wt% for N₂ at 273K and 20 bar;¹¹ Qc-5-Cu-sql-β even shows a higher CO₂/N₂ selectivity value (40000) at 293K.¹² However, a high accuracy of pore size control is required to achieve molecular size sieving, especially for CO₂ and CH₄ whose molecular size difference is only 0.046 nm. Moreover, CO₂ and CH₄ are always existing together industrially. Among various well-performing MOFs for CO₂ capture, only a few examples were found to separate CO₂/CH₄ efficiently, considering the flexible nature of MOFs that will facilitate the pore size to be changed under higher pressure.¹³

4.1.2 Ca-MOF and Zn-MOF based on squarate ligand (C₄O₄)

Ca(C₄O₄)(H₂O): Ca(C₄O₄)(H₂O) (UTSA-280) is a 3D MOF that involves s-block metal (Ca) and rigid organic linker (C₄O₄). (Figure 4-1)¹⁵ 1D motif chain is found along a-axis. With C₄O₄ ligands coordinated along b- and c-axis, two one-dimension cylindrical channels are observed in UTSA-280 along a-axis with 3.2 x 4.5 Å² and 3.8 x 3.8 Å². Both channels display similar cross-sectional areas of 14.4 Å², which is larger than the minimum cross-sectional area of C₂H₄ (13.7 Å²) and CO₂ (10.7 Å²) and smaller than C₂H₆ (15.5 Å²) and CH₄ (15.1 Å²). Combined with constrained C₄O₄ ligands, UTSA-280 shows a high separation performance of CO₂ from CH₄ and C₂H₄ from C₂H₆ under ambient condition. Lin *et al.*^{13,14} reported the uptake of C₂H₄ by UTSA-280 is 2.5 mmol g⁻¹ at 298K and 1 bar, while under the same condition, the uptake of C₂H₆ is only 0.098 mmol g⁻¹; the CO₂ uptake capacity is reported as 3.0 mmol g⁻¹ under 298K and 1 bar, while it shows negligible adsorption for CH₄. It is worth to mention that the coordinated water is essential for the structure to let UTSA-280 exhibit a high sieving effect. Only one seven-coordinated Ca site can be found in UTSA-280, which coordinate with six

oxygen atoms from five C_4O_4 linkers and one oxygen atom from water molecule. As for organic linker, each C_4O_4 linker coordinates with five Ca ion centers.

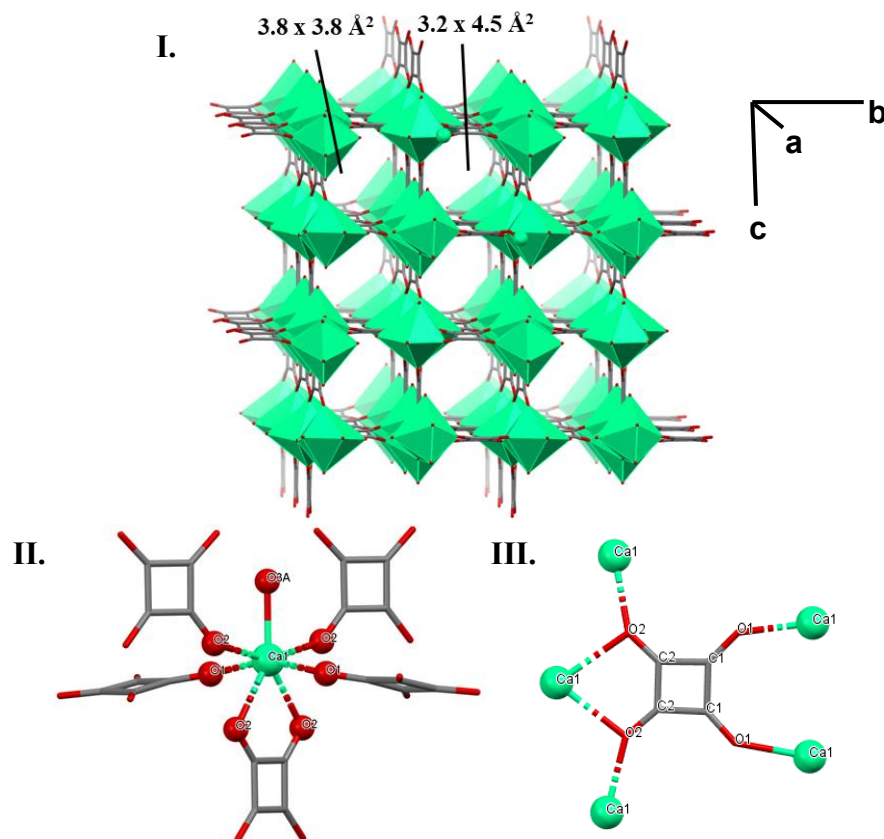


Figure 4-1 (I). 3D framework of UTSA-280, (II). the local coordination geometries of the central Ca atoms, (III). the local coordination geometries of C_4O_4 linker (all H atoms are omitted for clarity)

$Zn(bipy)(C_4O_4)(H_2O)_2$ (bipy = 4,4-bipyridine,): It is a 3D porous MOF that contains Zn and two ligands, bipyridine and C_4O_4 ligand (**Figure 4-2**)¹⁶. Each Zn(II) is monodentate coordinated with two C_4O_4 ligands, forming the zigzag chain along a-axis. Further connected by two bipyridine ligands with bis-monodentate coordination mode, the 3D microporous network is constructed. Asymmetry unit of $Zn(bipy)(C_4O_4)(H_2O)_2$ only contains one Zn atom which is octahedrally coordinated with two oxygen atoms (two O(1)) from two C_4O_4 ligands, two nitrogen atoms (N(1) and N(2)) from two bipyridine ligands and two oxygen atoms (two O(3)) from coordinated water molecules. The quadrilateral grids porous channel has approximately 7.94 x 11.11 Å² cross section area. It is worth mentioning in $Zn(bipy)(C_4O_4)(H_2O)_2$, the hydrogen bond interaction among coordinated water molecule and uncoordinated guest water molecule slightly changes the channel structure. When there is guest

water within the porous channels, the pore size of quadrilateral grids is nearly $8.04 \times 11.49 \text{ \AA}^2$. Additionally, $\text{Zn}(\text{bipy})(\text{C}_4\text{O}_4)(\text{H}_2\text{O})_2$ displays good de/rehydration processes with guest water molecules.

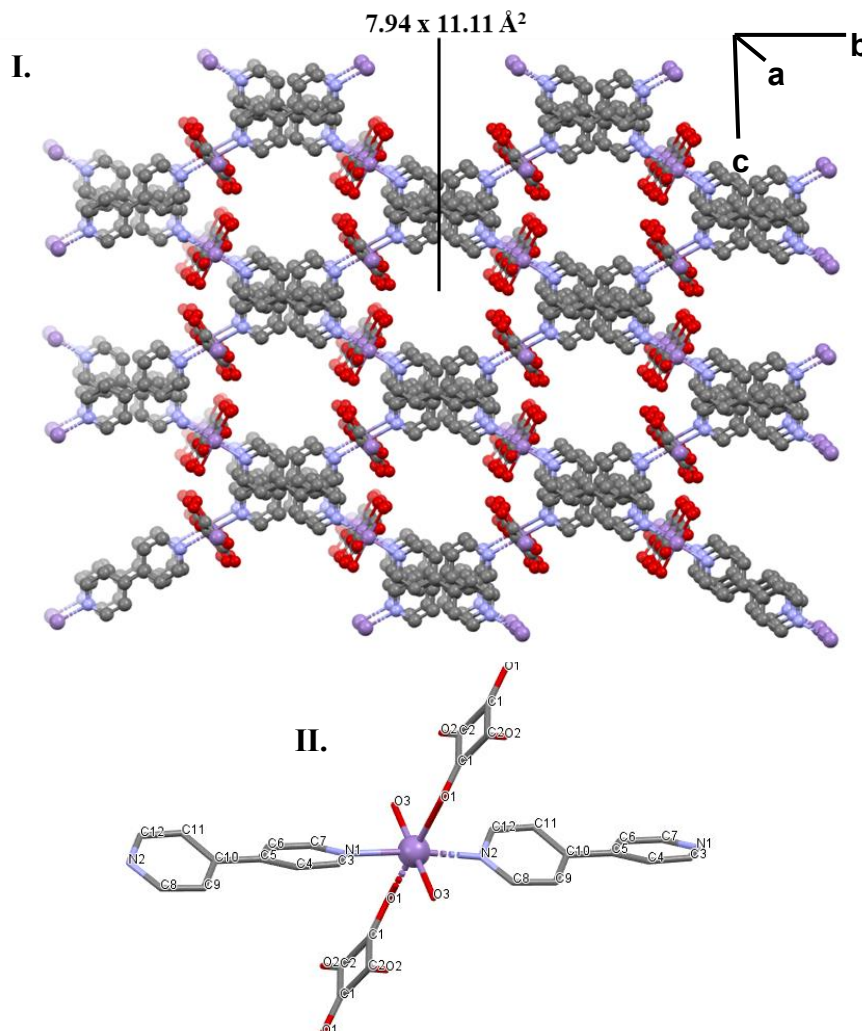


Figure 4-2 (I). 3D framework of $\text{Zn}(\text{bipy})(\text{C}_4\text{O}_4)(\text{H}_2\text{O})_2$, (II). the local coordination geometries of the central Zn atom. (In model, all terminal O atoms and N atoms are connected to Zn atoms, and all H atoms are omitted for clarity)

4.2 Experimental

4.2.1 Synthesis

UTSA-280: UTSA-280 was prepared according to the procedure from previously reported research with some modifications.¹⁵ A solution (16 ml water) of 0.182 g squaric acid and 0.128 g NaOH was slowly layered on top of a solution (40 ml water) of 1.888 g $\text{Ca}(\text{NO}_3)_2 \cdot \text{H}_2\text{O}$, 2.75

mL CH₃COOH and 1.280 g NaOH. After three days in room temperature, water was used for washing the product and the colorless single crystal was obtained by vacuum filtration and dried at room temperature.

Zn(bipy)(C₄O₄)(H₂O)₂: Zn(bipy)(C₄O₄)(H₂O)₂ was prepared according to the procedure from previously reported research with some modifications.¹⁶ A solution (20 ml water) of 0.057 g squaric acid was added into a solution (70 ml water) of 0.156 g 4,4'-bipyridine and 0.068 g ZnCl₂. Allowing to stand for one week, water was used for washing the product and colorless single crystal was obtained by vacuum filtration and dried at room temperature.

4.2.2 Activation scheme

UTSA-280: Due to the coordinated water molecule will be removed easily with high temperature, a mild activation condition was used to empty the adsorbed water after synthesis. According to the scheme from Lin's lab¹⁴, the as-made MOF was activated using 100 °C under vacuum for 1 day followed 110 °C under vacuum for 2 days after modification. Same condition was applied for the reactivation after CO₂ adsorbed.

Zn(bipy)(C₄O₄)(H₂O)₂: The fresh as-made MOF was activated under 70°C under vacuum for 6 hours.

4.2.3 Powder X-ray diffraction measurements

Powder X-ray Diffraction patterns were obtained with a Rigaku diffractometer using Cu- $\kappa\alpha$ radiation ($\lambda=1.5406 \text{ \AA}$). Samples were scanned in the range $5^\circ \leq 2\theta \leq 45^\circ$ at a rate of $10^\circ/\text{min}$ with a step-size of 0.02° .

4.2.4 Thermogravimetric Analysis (TGA)

TGA measurement were conducted by heating the sample from room temperature to 700 °C at a rate of 10 °C/min, which can be used to check if the pore is completely empty. Additionally, TGA helps to determine the thermal stability by checking the decomposition temperature.

4.2.5 Brunauer–Emmett–Teller (BET) - CO₂ adsorption measurement

The CO₂ single-component adsorption isotherm was measured on Micromeritics ASAP 2020. The adsorption measurement was performed at 273K with ice-water bath from 0.01

relative pressure to 0.3 relative pressure at increasing rate 0.01 relative pressure. About 100 mg activated sample was prepared for each adsorption measurement.

4.2.6 Gas loading

To empty the pore of MOFs for CO₂ loading, about 100 mg sample are prepared on the horizontal bottom of a L-shaped glass tube. A small amount of glass wool was used to make sure the sample was tightly packed. After activation (using the activation scheme above), certain amount of pure ¹³C enriched ¹³CO₂ or D labeled C₂H₂ in a round bottom flask was introduced into the vacuum line with the vacuum line isolated from either vacuum or air. Then using liquid nitrogen surround the L-shape glass tube to condense and trap loaded gas, followed by the flame-sealing under vacuum. Approximately 0.1 mole of ¹³CO₂ (or 0.1 mole of C₂D₂) per mole of metal in MOFs was used in this experiment.

4.2.7 D₂O exchange

100 mg UTSA-280 and Zn(bipy)(C₄O₄)(H₂O)₂ were sunk in 10 ml D₂O solvent for three days. The sample was then placed in the oven under 60 °C for 12 hours. The dried sample was put in the 5 mm glass tube with the cap, which is then ready for the ²H SSNMR experiment. For UTSA-280, the D₂O exchanged sample was activated as well.

4.2.8 ²H and ¹³C static SSNMR

For both static ²H and ¹³C SSNMR, a Varian Infinity Plus 400 spectrometer that operated with an Oxford 9.4 T magnet and a Varian/Chemagnetics 5mm HX static probe were used. The CO₂ and C₂H₂ adsorption behaviors can be probed by variable-temperature study from 133 K to 373 K using a Varian VT temperature control unit calibrated by ²⁰⁷Pb chemical shift of solid Pb(NO₃)₂. Additionally, the exchange of D₂O from the solvent and coordinated H₂O on the structure can be observed by the ²H SSNMR under room temperature. Ethanol was used as the reference for chemical shift ¹³C, where the methylene carbon of ethanol was set at 56.83 ppm from tetramethylsilane (TMS). While D₂O was used as the reference for chemical shift ²H, the sharp single peak for hydrogen was set at 4.8 ppm from TMS.

DEPTH-echo sequences without decoupling were applied to acquire ¹³C spectra and

quadrupolar-echo sequences were used in ^2H spectra. For ^{13}C NMR, the 90° pulse length (pw90) was set at $3.6\ \mu\text{s}$, pulse delay was set at 3 s and $40\ \mu\text{s}$ for τ_1 while $20\ \mu\text{s}$ for τ_2 . For ^2H NMR, the 90° pulse length (pw90) was set at $3.2\ \mu\text{s}$ for C_2D_2 and $3.6\ \mu\text{s}$ for D_2O , pulse delay was set at 2 s and $50\ \mu\text{s}$ for τ_1 while $45\ \mu\text{s}$ for τ_2 . To obtain the spectra with high resolution, all spectra for gas loaded sample under various temperature have approximately 1000 scans except the ^{13}C static NMR under room temperature (293K), which is nearly 10000 scans. Three ^2H spectra for D_2O exchanged MOFs have around 30000 scans.

4.3 Results and discussion

4.3.4 Synthesis and characterization with PXRD

PXRD patterns of all as-made complexes are highly consistent with the simulated ones from the literature (**Figure 4-3**), which indicates that both UTSA-280 and $\text{Zn}(\text{bipy})(\text{C}_4\text{O}_4)(\text{H}_2\text{O})_2$ were successfully synthesized according to the listed synthesis scheme in section 5.2.1. The peaks of activated UTSA-280 and $\text{Zn}(\text{bipy})(\text{C}_4\text{O}_4)(\text{H}_2\text{O})_2$ show high agreement with the simulated patterns as well, suggesting the frameworks of both MOFs are maintained after the removal of guest molecule that was left within the porous channels during the synthesis. Additionally, the PXRD patterns for reactivated UTSA-280 is also plotted. Due to the high consistency of the peaks between the reactivated patterns and the simulated patterns, it is believed that the framework is unchanged during the reactivation.

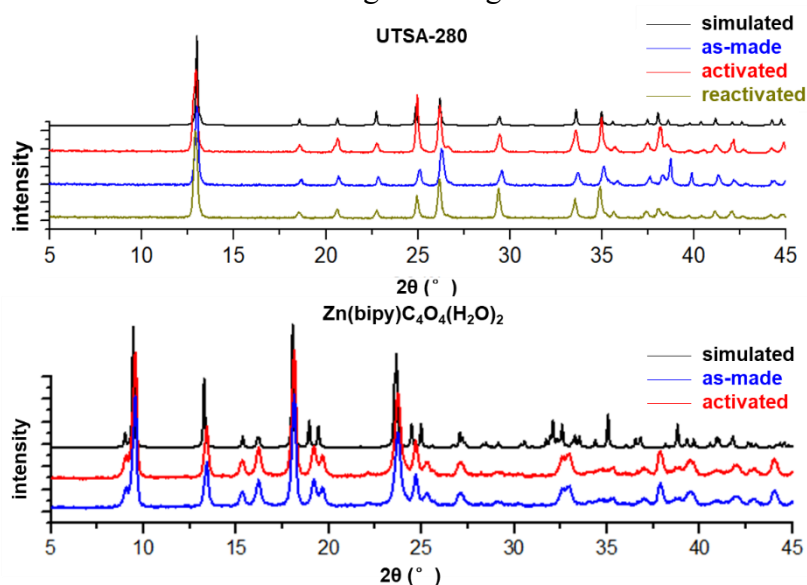


Figure 4-3 PXRD patterns for UTSA-280 and $\text{Zn}(\text{bipy})\text{C}_4\text{O}_4(\text{H}_2\text{O})_2$.

4.3.5 Thermal stability with TGA

Figure 4-4 shows the TGA curves for both as-made and activated UTSA-280 and $\text{Zn}(\text{bipy})\text{C}_4\text{O}_4(\text{H}_2\text{O})_2$, where both MOFs exhibit great capacities for water adsorption. The decomposition temperatures for these two MOFs are around 800 °C and 450 °C, respectively. For UTSA-280, the TGA curve of as-made sample exhibits the first weight loss around 100 °C, associated with the loss of both guest water molecules and the coordinated water molecules. The porous framework cannot be maintained at this temperature as well according to the published paper.¹⁵ Followed by a flat line until the temperature reaches around 300 °C, the C_4O_4 linkers start decomposing. $\text{Ca}(\text{OH})_2$ is likely the remain when temperature approaches 800 °C. After the activation, a slight weight loss can be found around 100 °C, which corresponds to the removal of coordinated water molecules. Comparing the percent of weight loss around 100 °C for both as-made and activated UTSA-280, it can be concluded that all the guest water molecules are removed, and a small amount of coordinated water molecules are likely removed as well during activation. After 100 °C, the TGA curve of as-made UTSA-280 shows high consistency with that of activated UTSA-280, which demonstrates the same behaviors with elevating temperature.

Similar to UTSA-280 which is synthesized in water, an obvious weight loss can be found started from around 70 °C in the TGA curves of $\text{Zn}(\text{bipy})\text{C}_4\text{O}_4(\text{H}_2\text{O})_2$ where guest water molecules are removed and ended at around 120 °C where coordinated water molecules are removed as well. The large porous channels of $\text{Zn}(\text{bipy})\text{C}_4\text{O}_4(\text{H}_2\text{O})_2$ allow the lower temperature for removal of guest water molecules. Followed by a weight loss around 180 °C, bipyridine ligands are decomposed. ZnO is believed to be the remain after the huge weight loss starting from 380 °C which includes the decomposition of C_4O_4 linkers as well. After activation, a mild loss on sample weight from 100 °C to 200 °C was observed instead of the obvious drop at 100 °C, which is associated with the removal of coordinated water molecules. Also proved by the PXRD results that framework is unchanged after activation, the coordinated water molecules is much harder to be removed than the guest water molecules when the temperature is around 100 °C. Two weight loss drops at 250 °C and 380 °C are then belonging to the removal of bipyridine and C_4O_4 linkers, respectively.

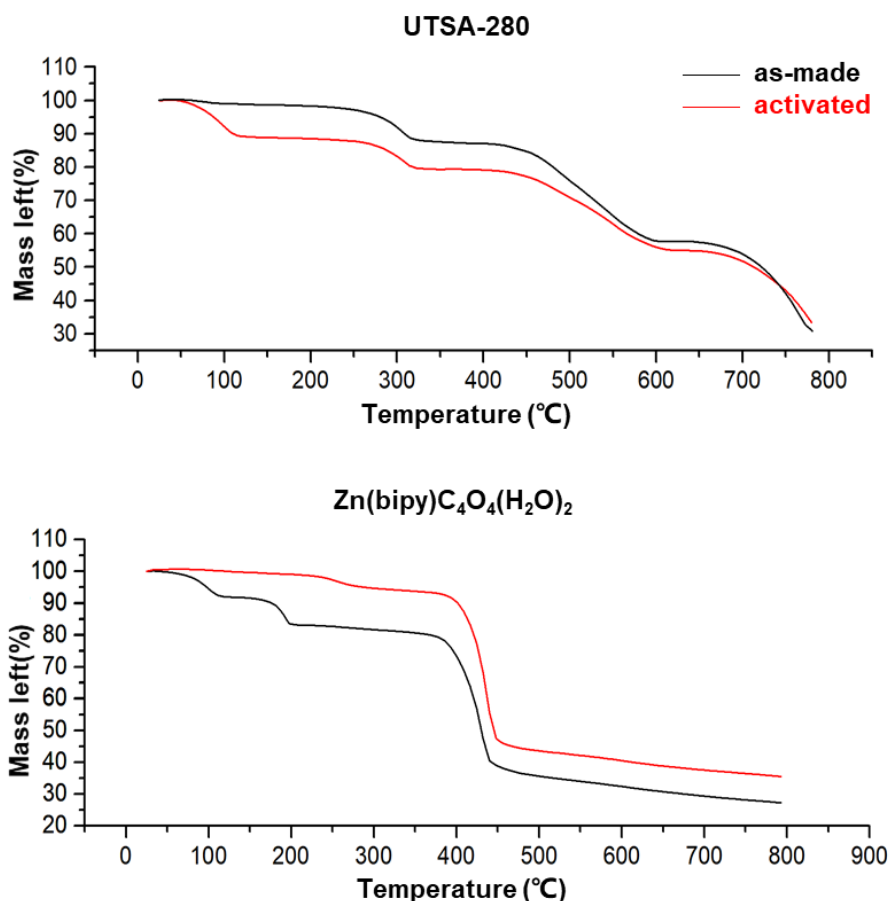


Figure 4-4 TGA curves for UTSA-280 and Zn(bipy)C₄O₄(H₂O)₂.

4.3.6 CO₂ adsorption measurement with BET

The CO₂ adsorption curves of both activated and reactivated UTSA-280 are plotted in **Figure 4-5**. For the activated sample, the CO₂ adsorption capacity increases obviously with the elevating temperature. However, after reactivation where the sample with CO₂ loaded is activated again, the great difference of CO₂ adsorption capacities between the activated and reactivated UTSA-280 is found. Due to the similar cross section area of CO₂ and porous channels of UTSA-280, CO₂ likely has strong interaction with the frameworks of UTSA-280, which can be further proved by the NMR experiment for the ¹³CO₂ loaded UTSA-280. The mild activation scheme cannot provide enough energy to compete with those interaction. In this case, CO₂ is probably still trapped within the channels that prevents more CO₂ to be adsorbed.

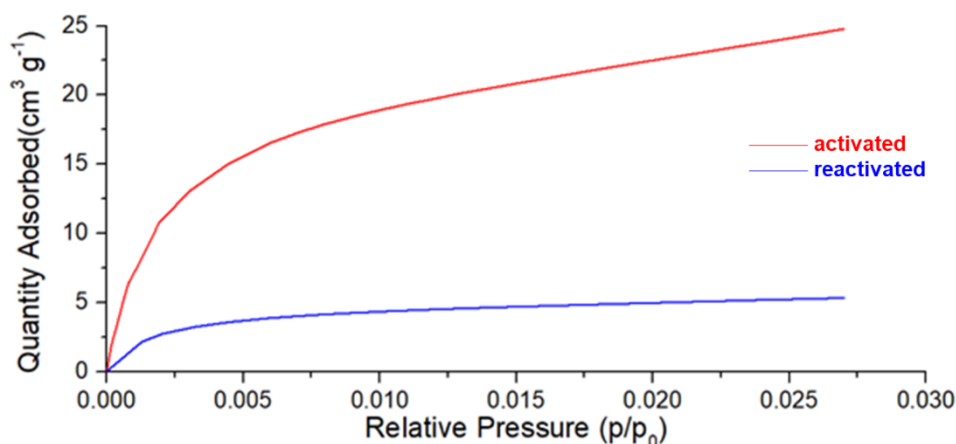


Figure 4-5 CO₂ sorption isotherm of UTSA-280 at 273K.

4.3.7 ²H SSNMR of MOFs with D₂O exchange

To obtain the information on the coordinated water molecules on the MOFs framework, ²H static SSNMR experiments were performed on with the MOFs that were sunk in D₂O solvent for three days. Experimental and WSolids simulated ²H spectra of D₂O exchanged UTSA-280 (before and after activation) and Zn(bipy)C₄O₄(H₂O)₂ are exhibited in **Figure 4-6** and **4-7**, respectively. The C_Q and η_Q values extracted from WSolids simulations are listed in **Table 4-1**. Since the ²H natural abundance is 0.0156% and 99% isotopically labeled D₂O solvent was used, all ²H resonances observed in spectra originate from the adsorbed D₂O and the exchanged coordinated D₂O on the framework.

Within UTSA-280, there is only one coordinated H₂O site within one unit cell, related by a 2₁ screw axis along any principle axis of the crystal structure. However, for each site of the coordinated H₂O, two possible positions are included, which leads to two crystallographically independent coordinated H₂O in UTSA-280. As two hydrogen atoms on a single H₂O are equivalent, a total of two inequivalent hydrogen atoms are resulted. In this case, two distinct patterns should be observed in the ²H SSNMR spectrum of activated UTSA-280 if they are with distinct C_Q or η_Q.

Three distinct resonances are simulated from the ²H SSNMR spectrum of D₂O exchanged UTSA-280 before activation. The resonance at site 1 (purple) is likely associated with the D₂O molecules that are adsorbed within UTSA-280 as the high affinity and the small C_Q value of 56(1) kHz compared with those of other two sites. The C_Q value is not zero but much lower

than that of static D₂O (225 kHz)¹⁷, indicating the D₂O molecules within porous channels are not static and with restricted mobility. The resonances at site 2 and site 3 have relatively higher C_Q value but much less intensity. It likely results from a small amount of D₂O that already exchanged with coordinated water molecules on the framework, whose motion is further restricted due to the coordination with the framework. Two distinct resonances hint two crystallographically inequivalent hydrogen atoms within a single unit cell, which is consistent with the structure that obtained from the X-ray diffraction. After activation, the adsorbed D₂O associated resonance is no longer seen, indicating the water molecules within channels are fully removed during the activation and meanwhile the framework is still maintained as the coordinated D₂O can still be observed. Additionally, the C_Q value is slightly decreases at both sites after removal of the adsorbed D₂O, which probably results from the loss of hydrogen bonding interaction.

In short, a small amount of solvent water molecules successfully exchange with the coordinated water molecule, and it is also proved that two distinct positions of coordinated water molecules are found in UTSA-280.

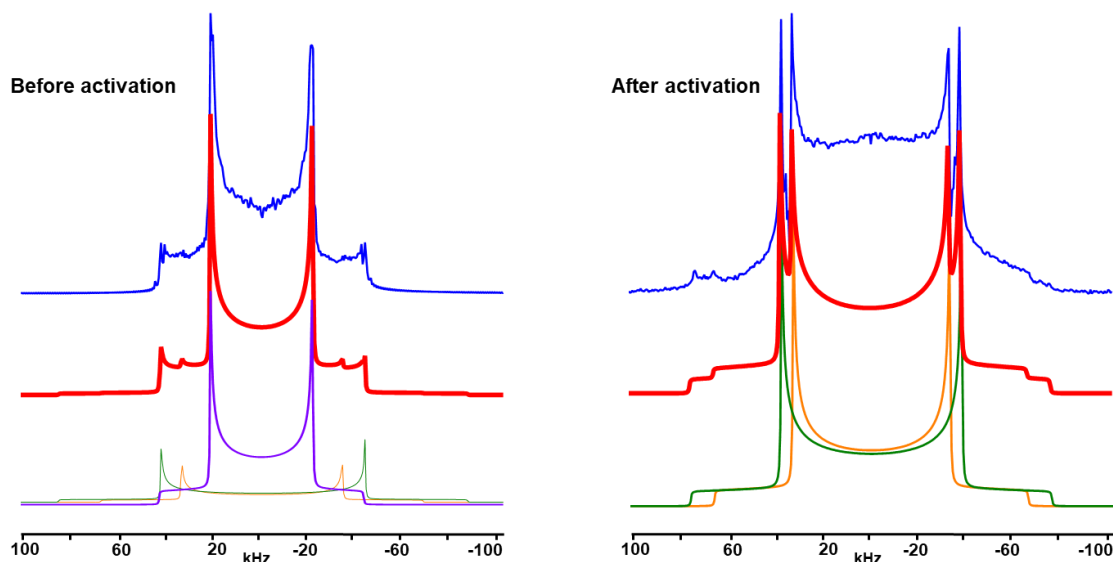


Figure 4-6 Experimental (top) and simulated (middle) static ²H SSNMR spectra of D₂O exchanged UTSA-280 before and after activation with stacked resonances of each site (bottom).

Within Zn(bipy)C₄O₄(H₂O)₂, there is only one crystallographically independent H₂O molecule in one unit cell. In such case, a single resonance should be observed in the ²H SSNMR

spectrum of activated $\text{Zn}(\text{bipy})\text{C}_4\text{O}_4(\text{H}_2\text{O})_2$.

The ^2H SSNMR experiment of D_2O exchanged $\text{Zn}(\text{bipy})\text{C}_4\text{O}_4(\text{H}_2\text{O})_2$ was repeated twice with different preparation conditions. The first sample was exposed to the air for several days after drying, whose ^2H SSNMR spectrum was shown in the **Figure 4-7** (left). The ^2H SSNMR experiment was immediately performed after drying for second sample, whose ^2H SSNMR spectrum was exhibited in the **Figure 4-7** (right).

For the first sample, not a standard Pake doublet is observed in the ^2H SSNMR spectrum of D_2O exchanged $\text{Zn}(\text{bipy})\text{C}_4\text{O}_4(\text{H}_2\text{O})_2$. Instead, a doublet with a huge broad shoulder was observed. By WSolid simulation, multiple sites can be extracted. Only three adsorbed D_2O associated resonances are shown in **Figure 4-7**, as they can reveal a general lineshape of the experimental patterns. However, more resonances are included within the experimental patterns with different C_Q and η_Q values. As listed in **Table 4-1**, all three resonances exhibit various C_Q and η_Q values, which likely results from the hydrogen bonding interaction with different strengths. This assumption supports that $\text{Zn}(\text{bipy})\text{C}_4\text{O}_4(\text{H}_2\text{O})_2$ is featured with the large porous channels and the large amount of hydrogen bonds when there is guest water molecules.

For the second sample, a totally different lineshape was obtained. Two resonances are simulated with larger C_Q values, which are likely associated with the coordinated D_2O molecules. The middle part of this ^2H SSNMR spectrum is likely associated with the adsorbed D_2O molecules, which can be simulated by more than three resonances, like shown in the ^2H SSNMR spectrum of the first $\text{Zn}(\text{bipy})\text{C}_4\text{O}_4(\text{H}_2\text{O})_2$ sample.

In short, for $\text{Zn}(\text{bipy})\text{C}_4\text{O}_4(\text{H}_2\text{O})_2$, the observations from two ^2H SSNMR experiments are not consistent. In such case, although the large channels were proved by the various resonances associated with the adsorbed D_2O molecules, there is no other result that can be confirmed so far. More work is needed to study the detailed information on the structure of $\text{Zn}(\text{bipy})\text{C}_4\text{O}_4(\text{H}_2\text{O})_2$ in future.

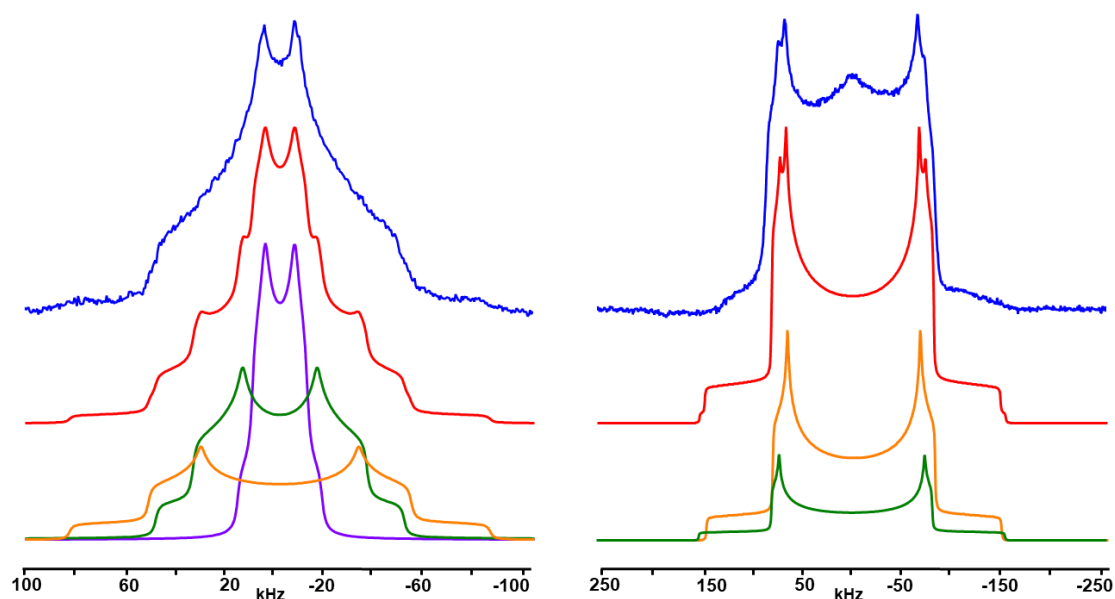


Figure 4-7 Experimental (top) and simulated (middle) static ^2H SSNMR spectra of D_2O exchanged $\text{Zn}(\text{bipy})\text{C}_4\text{O}_4(\text{H}_2\text{O})_2$ before activation. (Left: the ^2H SSNMR experiment was performed after the sample was exposed to air for several days. Right: the ^2H SSNMR experiment was immediately performed after the sample was dried)

Table 4-1 The ^2H SSNMR parameters of D_2O exchanged UTSA-280 and $\text{Zn}(\text{bipy})\text{C}_4\text{O}_4(\text{H}_2\text{O})_2$.

	Site	Intensity (%)	C_Q (kHz)	η_Q
UTSA-280 (Before activation)	1	80	56(1)	0
	2	4	89(1)	0
	3	12	110(1)	0
UTSA-280 (After activation)	1	-	-	-
	2	38	87(1)	0
	3	62	100(1)	0
$\text{Zn}(\text{bipy})\text{C}_4\text{O}_4(\text{H}_2\text{O})_2$ (1)	1	29	22(1)	0.30(1)
	2	26	110(1)	0.25(1)
	3	45	65(1)	0.40(1)
$\text{Zn}(\text{bipy})\text{C}_4\text{O}_4(\text{H}_2\text{O})_2$ (2)	1	71	193(1)	0.10(1)
	2	29	200(1)	0.05(1)

4.3.8 *In situ* ^2H VT SSNMR of UTSA-280 with C_2D_2

Figure 4-8 shows the experimental and WSolids simulated ^2H spectra of C_2D_2 loaded UTSA-280 from 173 K to 333 K. Since the ^2H natural abundance is 0.0156% and 99% isotopically labeled C_2D_2 gas was used, all ^2H resonances observed in spectra originate solely from the loaded C_2D_2 rather than the framework.

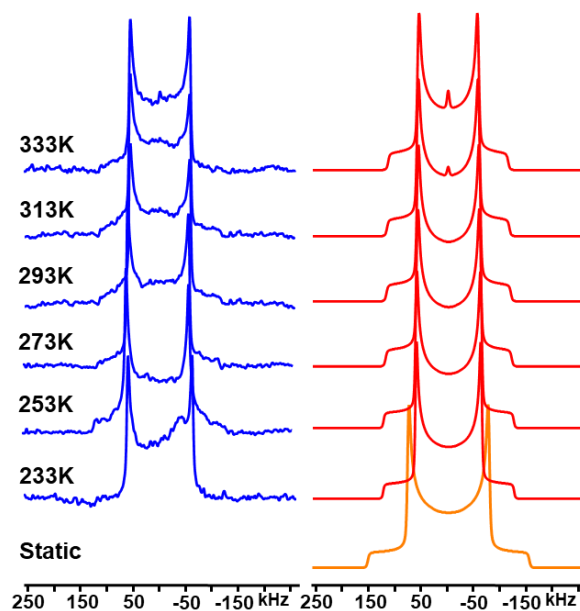


Figure 4-8 Experimental (blue) and simulated (red) static ^2H VT SSNMR spectra of C_2D_2 loaded UTSA-280. (0.1 mole C_2D_2 was loaded per mole of Ca)

Two distinct resonances are featured in ^2H SSNMR spectra at temperature of 333 K and 313 K, as confirmed by the analytical simulations with WSolid package. A sharp resonance with low intensity located at 0 kHz results from the gaseous, mobile C_2D_2 . A typical temperature-dependent Pake doublet is found from 333 K to 173 K, which is C_2D_2 associated, indicating both deuterium in C_2D_2 are interacting with an equivalent chemical environment. Additionally, an uncommon resonance starts shown at 253 K, which is left shifting with the decreasing temperature. Since it is independent to the patterns associated with C_2D_2 , the C_2D_2 associated Pake doublet can still be simulated. The origin for this uncommon resonance then needs further investigation as future work.

As the temperature decreases (when below 293 K), the gaseous C_2D_2 associated sharp resonance disappears, indicating the C_2D_2 is totally adsorbed within the UTSA-280 and higher C_2D_2 adsorption capacity at lower temperature is revealed. The C_Q and η_Q values extracted from

WSolids simulations are listed in **Table 4-2**. Due to the decreased C_2D_2 mobility, the patterns are broadened under lower temperature. The C_Q values increases from 148(1) kHz at 333 K to 167(1) kHz at 173 K. All those values are non-zero but slightly lower than that of static C_2D_2 (198 kHz)¹⁸, which indicates the adsorbed C_2D_2 is not static but highly restricted on its mobility. The large C_Q values can be explained by the dramatically large C_2D_2 -MOF interaction due to the limited cross-section area of the porous channels in UTSA-280 that is close to the cross-section area of C_2D_2 . The η_Q values are zero under all temperatures as the value for the static C_2D_2 ,¹⁸ suggesting the axial symmetry in the electric field gradient around the deuterons at the adsorption sites.

Table 4-2 The 2H SSNMR parameters and motional data of adsorbed C_2D_2 in UTSA-280 at various temperature. (All motion rates are $\geq 10^7$ Hz)

Temperature (K)	C_Q (kHz)	η_Q	α (C_3 wobbling angle, $^\circ$)	β (C_4 hopping angle, $^\circ$)
333	148(1)	0	23(1)	10(1)
313	151(1)	0	22(1)	10(1)
293	153(1)	0	21(1)	10(1)
273	155(1)	0	20(1)	10(1)
253	160(1)	0	19(1)	10(1)
233	161(1)	0	18(1)	10(1)
223	161(1)	0	18(1)	10(1)
213	161(1)	0	18(1)	10(1)
193	163(1)	0	18(1)	10(1)
173	167(1)	0	17(1)	10(1)

To obtain deeper information on C_2D_2 motion, the EXPRESS software package was used to simulate the C_2D_2 associated resonance. The C_2D_2 motional data extracted from the EXPRESS simulation are listed in **Table 4-2** and they fit analytical simulated spectra well (**Figure 4-9a**). According to the motional data, C_2D_2 undergoes two types of motion in UTSA-

280, localized rotation upon adsorption site (threefold (C_3) wobbling) and fourfold (C_4) non-localized hopping symmetry-equivalent adsorption sites. The angle between the C_2D_2 molecule and the C_3 wobbling axis is defined as α , while the β denotes the equivalent rotation angle for C_4 hopping. The C_4 hopping sites are exhibited in **Figure 4-9b**. It is worth mentioning that all wobbling rotations with more than 3 folds will result in the same powder pattern.

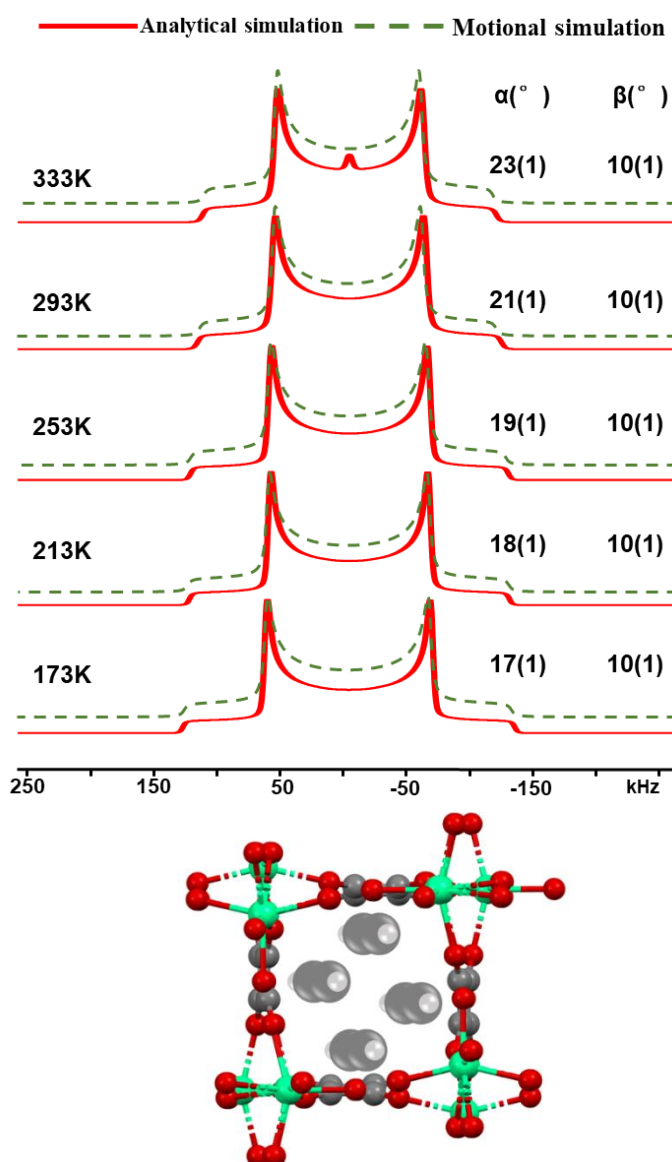


Figure 4-9 (a). Analytical simulated and motional simulated static 2H SSNMR spectra of C_2D_2 loaded UTSA-280, including both threefold wobbling angles (α) and fourfold hopping angles (β) at different temperatures. (b). The model of C_2D_2 C_4 hopping within UTSA-280.

(C_2D_2 molecules are zoomed out for the clearer view of four sites)

The motional rate of C_2D_2 sits in the fast motion regime ($\geq 10^7$ Hz) at all temperatures that

were performed in this experiment. With the temperature increases from 173K to 333K, the wobbling angle value (α) slightly increases from 17(1) $^\circ$ to 23(1) $^\circ$, which indicates that C_2D_2 wobbles with a larger angle. In this case, a larger volume of space is occupied by C_2D_2 wobbling within the channel as more thermal energy is given, which is available to compete with the adsorptive interaction. As for the fourfold hopping angle value (β), with the various temperature, it is always determined as 10(1) $^\circ$. The unchanged orientation of C_2D_2 molecules with respect to C_4 rotational axis can also be explained by the limited space of channels within UTSA-280 and the extremely close cross-section area of channels and C_2D_2 molecules.

4.3.9 *In situ* ^{13}C VT SSNMR of UTSA-280 with $^{13}CO_2$

To obtain the detailed information on dynamics of CO_2 adsorbed within UTSA-280, *in situ* ^{13}C VT SSNMR experiments at temperatures ranging from 373 to 173 K were performed. All experimental and analytically simulated spectra are illustrated in **Figure 4-10a**. Since the 99% isotopically labeled $^{13}CO_2$ gas was used, all ^{13}C resonances observed in spectra originate solely from the loaded $^{13}CO_2$ rather than the framework.

Three distinct resonances are featured in ^{13}C SSNMR spectra at temperature from 373 K to 313 K, as confirmed by the analytical simulations with WSolid package (**Figure 4-10b**). The sharp resonance (yellow) located at around 124 ppm results from the gaseous, mobile CO_2 . The broad, temperature-dependent powder patterns correspond to $^{13}CO_2$ adsorbed within the UTSA-280. Due to the decreased CO_2 mobility, the patterns are broadened under lower temperature with certain amount of chemical shift anisotropy (CSA). Similar changes on broad ^{13}C SSNMR powder patterns with temperature are also observed for CO_2 adsorbed SDB-MOF in section 4 and other MOFs.^{19,20}

When temperature decreases below 293K, the gaseous CO_2 associated sharp ^{13}C resonance is no longer seen, which indicates that all loaded $^{13}CO_2$ is adsorbed within UTSA-280. It can also be concluded that higher CO_2 adsorption capacity is achieved in UTSA-280 at lower temperature. Other two broad powder patterns both slightly decreases in width as temperature decreases, which means the CO_2 mobility is further restricted. ^{13}C chemical shift parameters of resonances for adsorbed $^{13}CO_2$ are listed in **Table 4-3**. For the ^{13}C resonance at site 1, the span value (Ω) increases from 245(2) ppm at 373 K to 300(3) ppm at 173K. All span values are non-

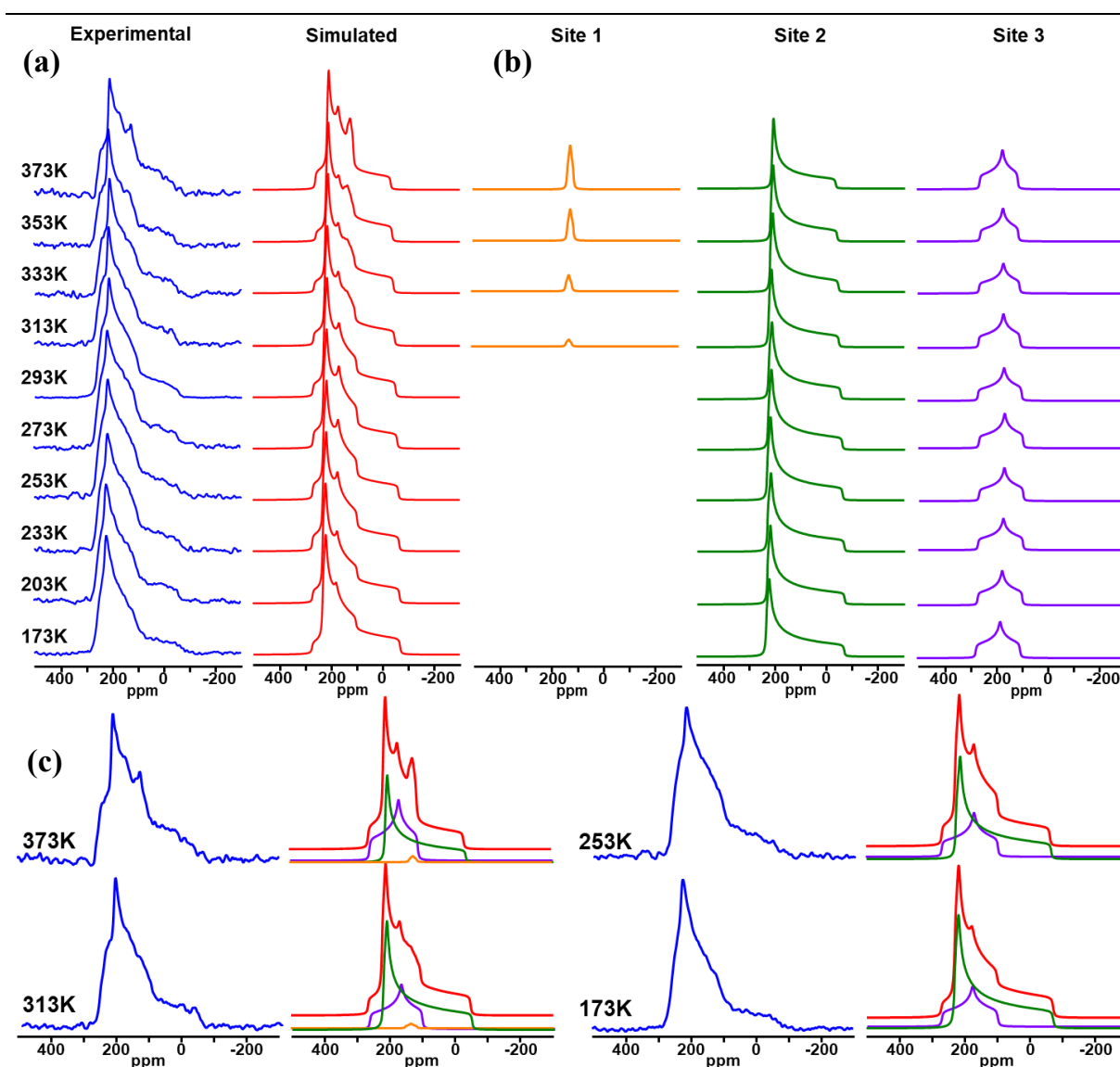


Figure 4-10 (a). The experimental (blue) and simulated (red) static ^{13}C VT SSNMR spectra of UTSA-280 loaded with $^{13}\text{CO}_2$. (b). The specific patterns for free (orange) and adsorbed (green and purple) $^{13}\text{CO}_2$ at two different sites. (c). comparison of experimental and stacked simulated spectra of $^{13}\text{CO}_2$.

zero and but less than that of static CO_2 (335 ppm),²¹ which indicates that CO_2 adsorbed within UTSA-280 is not static but highly restricted on its mobility. Additionally, the span values are relatively large when comparing with that with other MOFs (such as SDB-MOFs in section 4). It is explained by the much stronger interaction between CO_2 and framework, consistent with the fact that UTSA-280 has relatively smaller porous channels, whose cross-section area is just slight larger than that of CO_2 molecule. As the temperature decreases, there is no obvious change on the skew value (κ), from 0.95(1) at 373 K to 0.92(1) at 173 K, which suggest the

MOF-CO₂ interaction strength is not altered a lot. For the ¹³C resonance at site 2, the chemical shift values have large deviation from the normal chemical shift value for CO₂, which may result from the existence of different species. A likely assumption is the formation of -COOH. As determined that the resonance at site 2 does not originate from the adsorbed CO₂, this resonance will not be discussed in CO₂ dynamic section and further investigation can help to obtain a better information on this species.

Table 4-3 The ¹³C chemical shift parameters of adsorbed ¹³CO₂ in UTSA-280 at various temperature.

Site	Temperature (K)	Intensity (%)	δ_{iso} (ppm)	Ω (ppm)	κ
1	373	58	129.0(5)	245(2)	0.95(1)
	353	75	129.0(5)	255(2)	0.93(1)
	333	73	129.0(5)	263(2)	0.92(1)
	313	70	129.0(5)	270(2)	0.92(1)
	293	71	129.0(5)	277(2)	0.91(1)
	273	65	128.0(5)	285(3)	0.91(1)
	253	67	127.0(5)	290(3)	0.91(1)
	233	68	127.0(5)	295(3)	0.91(1)
	203	73	127.5(5)	297(3)	0.92(1)
	173	76	128.0(5)	300(3)	0.92(1)
2	373	37	180.0(5)	147(2)	-0.20(1)
	353	22	178.0(5)	149(2)	-0.20(1)
	333	24	180.0(5)	156(2)	-0.20(1)
	313	28	180.0(5)	160(2)	-0.20(1)
	293	29	178.0(5)	168(2)	-0.20(1)
	273	35	177.0(5)	170(2)	-0.17(1)
	253	33	179.0(5)	171(2)	-0.15(1)
	233	32	180.0(5)	173(2)	-0.13(1)
	203	27	180.0(5)	172(2)	-0.11(1)

173	24.0	185.0(5)	170(2)	-0.10(1)
-----	------	----------	--------	----------

To obtain deeper information on CO₂ motion, the EXPRESS software package was used to simulate the resonances on site 1 as well. The CO₂ motional data obtained from the EXPRESS simulation are listed in **Table 4-4** and they fit analytical simulated spectra well (**Figure 4-11**). According to the motional data, CO₂ undergoes two types of motion in UTSA-280, localized rotation upon adsorption site (threefold (*C*₃) wobbling) and fourfold (*C*₄) non-localized hopping symmetry-equivalent adsorption sites. The angle between the CO₂ molecule and the *C*₃ wobbling axis is defined as α , while the β denotes the equivalent rotation angle for *C*₄ hopping. The *C*₄ hopping sites are exhibited in **Figure 4-12**. It is worth mentioning that all wobbling rotations with more than 3 folds will result in the same powder pattern.

Table 4-4 The CO₂ motional data of adsorbed ¹³CO₂ in UTSA-280 at various temperature. All motion rates are $\geq 10^7$ Hz.

Temperature (K)	α (<i>C</i> ₃ wobbling angle, °)	β (<i>C</i> ₄ hopping angle, °)
373	22.0(5)	10(1)
353	22.0(5)	10(1)
333	21.0(5)	10(1)
313	20.5(5)	10(1)
293	20.0(5)	10(1)
273	19.0(5)	10(1)
253	18.0(5)	10(1)
233	18.0(5)	10(1)
203	18.0(5)	10(1)
173	17.5(5)	10(1)

The motional rate of CO₂ sits in the fast motion regime ($\geq 10^7$ Hz) at all temperature that performed in this experiment. With the temperature increases from 173K to 373K, the wobbling angle value (α) slightly increases from 17.5(5)° to 22.0(5)°, which indicates that CO₂

wobbles with a larger angle. In this case, a larger volume of space is occupied by CO₂ wobbling within the channel as more thermal energy is given, which is available to compete with the adsorptive interaction. As for the fourfold hopping angle value (β), as the temperature varies, it is always determined as 10(1)°. The unchanged orientation of CO₂ molecules with respect to *C4* rotational axis can also be explained by the limited space of channels within UTSA-280 and the extremely close cross-section area of channels and CO₂ molecules.

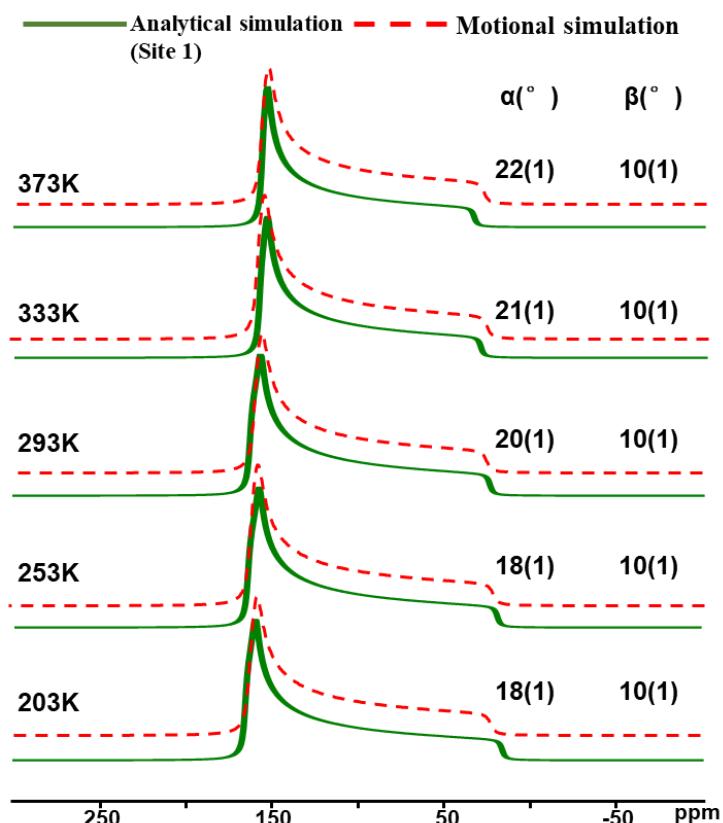


Figure 4-11 Analytical simulated and motional simulated static ¹³C SSNMR spectra of ¹³CO₂ loaded UTSA-280, including both threefold wobbling angles (α) and twofold hopping angles (β) at different temperatures.

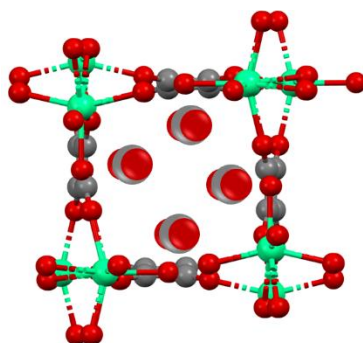


Figure 4-12 The model of CO₂ *C4* hopping within UTSA-280. (CO₂ molecules are zoomed out for the clearer view of four sites)

4.4 Conclusion

^2H SSNMR experiments have been performed to understand the structure of UTSA-280 and $\text{Zn}(\text{bipy})(\text{C}_4\text{O}_4)(\text{H}_2\text{O})_2$. The coordinated water molecules within UTSA-280 can easily exchange with solvent water molecule, and it is proved that there are two distinct H_2O position in one unit cell in UTSA-280. More work is required to obtain the detailed information on the structure of $\text{Zn}(\text{bipy})(\text{C}_4\text{O}_4)(\text{H}_2\text{O})_2$ in future. However, the large channels of $\text{Zn}(\text{bipy})(\text{C}_4\text{O}_4)(\text{H}_2\text{O})_2$ were confirmed, as the various adsorbed D_2O associated resonances shown in the ^2H SSNMR powder patterns. As the hydrogen bonds play the significant roles molecules adsorption within $\text{Zn}(\text{bipy})(\text{C}_4\text{O}_4)(\text{H}_2\text{O})_2$, C_2H_2 and CO_2 cannot be easily kept within the channels. A series of ^2H SSNMR experiments have been performed to obtain the detailed information on C_2H_2 adsorption and dynamics in UTSA-280. C_2H_2 was found to undergo a combination of a localized rotation (C_3 wobbling) and a non-localized motion (C_4 hopping between symmetry-equivalent adsorption sites) with the π -interaction between four-member ring of C_4O_4 ligand and triple bond of C_2H_2 . A series of ^{13}C SSNMR experiments have been used to obtain the detailed information on CO_2 adsorption and dynamics in the UTSA-280. Although UTSA-280 does not feature open metal sites or any functional groups, CO_2 was found to undergo a combination of a localized rotation (C_3 wobbling) and a non-localized motion (C_4 hopping) like the C_2H_2 behaviors in UTSA-280 with the π -interaction between four-member ring of C_4O_4 ligand and the double bond of CO_2 . With the help of single crystal x-ray diffraction experiments, the accurate CO_2 adsorption site can be determined as the future study. An uncommon ^{13}C resonance and an uncommon ^2H resonance were also found in either $^{13}\text{CO}_2$ or C_2D_2 loaded UTSA-280, which need the further investigation.

4.5 Reference

1. K. Sumida, D. L. Rogow, J. A. Mason, T. M. McDonald, E. D. Bloch, Z. R. Herm, T.-H. Bae & J. R. Long, Carbon Dioxide Capture in Metal–Organic Frameworks. *Chem. Rev.*, 2011, **112**, 724-781.
2. S. Ma & H.-C. Zhou, Gas storage in porous metal–organic frameworks for clean energy applications. *Chem. Commun.*, 2010, **46**, 44-53.

3. N. L. Rosi, J. Eckert, M. Eddaoudi, D. T. Vodak, J. Kim, M. O'keeffe & O. M. Yaghi, Hydrogen Storage in Microporous Metal-Organic Frameworks. *Science*, 2003, **300**, 1127-1129.
4. Q. Yang & C. Zhong. Understanding Hydrogen Adsorption in Metal-Organic Frameworks with Open Metal Sites: A Computational Study. *J. Phys. Chem. B*, 2006. **110 (2)**, 655-658.
5. L. J. Murray, M. Dincă & J. R. Long, Hydrogen storage in metal–organic frameworks. *Chem. Soc. Rev.*, 2009, **38**, 1294-1314.
6. Y. Li & G. Wen. Advances in Metal-Organic Frameworks for Acetylene Storage. *Eur. J. Inorg. Chem.* 2020, **24**, 2303–2311
7. H. Schobert. Production of Acetylene and Acetylene-based Chemicals from Coal. *Chem. Rev.* 2014, **114(3)**, 1743–1760
8. R. Matsuda, R. Kitaura, S. Kitagawa, Y. Kubota, R. V. Belosludov, T. C. Kobayashi, H. Sakamoto, T. Chiba, M. Takata, Y. Kawazoe & Y. Mita. Highly controlled acetylene accommodation in a metal-organic microporous material. *Nature*, 2005, **436**, 238–241.
9. X. Duan, Y. Cui, Y. Yang & G. Qian, Advances in Metal-Organic Frameworks for Acetylene Storage. *CrystEngComm*, 2017, **19**, 1464– 1469.
10. A. M. Plonka, D. Banerjee, W. R. Woerner, Z. Zhang, N. Nijem, Y. J. Chabal, J. Li & J. B. Parise, Mechanism of Carbon Dioxide Adsorption in a Highly Selective Coordination Network Supported by Direct Structural Evidence. *Angew. Chem. Int. Ed.*, 2013, **52**, 1692-1695.
11. B. Zheng, Z. Yang, J. Bai, Y. Li & S. Li, High and selective CO₂ capture by two mesoporous acylamide-functionalized rht-type metal–organic frameworks. *Chem. Commun.*, 2012, **48**, 7025-7027
12. J. Yu, L. H. Xie, J. R. Li, Y. Ma, J. M. Seminario & P. B. Balbuena, CO₂ Capture and Separations Using MOFs: Computational and Experimental Studies. *Chem. Rev.*, 2017, **117**, 9674-9754.
13. R. Lin, L. Li, A. Alsalmé & B. Chen. An Ultramicroporous Metal-Organic Framework for Sieving Separation of Carbon Dioxide from Methane. *Small structures*, 2020, **1(3)**.
14. R. Lin, L. Li, H. Zhou, H. Wu, C. He, S. Li, R. Krishna, J. Li, W. Zhou & B. Chen.

-
- Molecular sieving of ethylene from ethane using a rigid metal–organic framework. *Nature Materials*, 2018, **17**, 1128-1133.
15. L. Li, L. Guo, S. Pu, J. Wang, Q. Yang, Z. Zhang, Y. Yang, Q. Ren, S. Alnemrat & Z. Bao. A calcium-based microporous metal-organic framework for efficient adsorption separation of light hydrocarbons. *Chemical Engineering Journal*. 2019, **358**, 446-455.
16. C. Wang, S. Ke, Y. Hsieh, S. Huang, T. Wang, G. Lee & Y. Chuang. Water de/adsorption associated with single-crystal-to-single-crystal structural transformation of a series of two-dimensional metal–organic frameworks, $[M(\text{bipy})(\text{C}_4\text{O}_4)(\text{H}_2\text{O})_2]3\text{H}_2\text{O}$ ($M = \text{Mn}(1), \text{Fe}(2),$ and $\text{Zn}(3)$, and $\text{bipy}=4,4\text{-bipyridine}$). *J Chin Chem Soc.* 2019, **66**, 1031–1040.
17. R. J. Wittebort, M. G. Usha, D. J. Ruben, D. E. Wemmer & A. Pines. Observation of molecular reorientation in ice by proton and deuterium magnetic resonance. *J. Am. Chem. Soc.* 1988, **110:17**, 5668–5671.
18. F. S. Millett, B. P. Dailey, F. Spencer & M. And. NMR Determination of Some Deuterium Quadrupole Coupling Constants in Nematic Solutions. *J. Chem. Phys.* 2003, **56**, 3249.
19. X. Kong, E. Scouff, W. Ding, J. A. Maon, J. R. Long & J. A. Reimer. CO₂ dynamics in a metal-organic framework with open metal sites. *J Am Chem Soc.* 2012, **134(35)**, 14341-14344.
20. L. Lin, J. Kim, X. Kong, E. Scott, T. M. McDonald, J. R. Long, J. A. Reimer & B. Smit. Understanding CO₂ Dynamics in Metal–Organic Frameworks with Open Metal Sites. *Angewandte Chemie (International ed.)*, 2013. **52 (16)**, 4410-4413.
21. A. J. Beeler, A. M. Orendt, D. M. Grant, P. W. Cutts, J. Michl, K. W. Zilm, J. W. Downing, J. C. Facelli, M. S. Schindler & W. Kutzelnigg, Low-temperature carbon-13 magnetic resonance in solids. 3. Linear and pseudolinear molecules. *J. Am. Chem. Soc.*, 1984, **106**, 7672-7676.

Chapter 5

5. Overall conclusions

5.1 Summary and critical analysis

Six s-block metals-based MOFs with SDB ligands and two MOFs based on squarate ligands were synthesized and characterized in this thesis. CO₂ dynamics (and C₂H₂ dynamic, which is only in UTSA-280) were also investigated within five porous MOFs with various temperature.

Overall, the larger s-block metal give a higher coordination number within MOFs. Except Mg, all other five s-block metals show the similar coordination behavior with the same organic ligand. The reason that Mg gives the distinct structure when coordinating with SDB ligands may be: (1). Mg has the charge of 2+ when comparing with alkali metals (Li, Na and Cs). (2). Mg has the relatively smaller ionic radius when comparing with other two alkaline earth metals (Ca and Sr). The inversion center of unit cell in all MOFs (except as-made MgSDB) were not observed, which is inconsistent with the results obtained from X-ray diffraction. The inconsistency may result from the different technique. Since the X-ray diffraction is a simpler technique that focus on the position of atoms in the structure, but the surroundings of nuclei cannot be revealed. Instead, SSNMR provides deeper information on the nuclei, such as the alignment, involved interaction and coordination environment. Thus, XRD and SSNMR are complimentary to each other.

Additionally, in MOFs based on s-block metals, there is no direct interaction between metal center and small guest molecules. The physical interaction between molecules and framework dominantly assists the gas adsorption in MOFs based on s-block metals.

5.2 Future work

Most of the structure of SDB MOFs that discussed in this thesis were characterized, and ⁸⁷Sr MAS NMR will be useful to further study the metal local environment in SrSDB with the possible restructured framework after activation. Additionally, more work is required to obtain the detailed information on the structure of Zn(bipy)(C₄O₄)(H₂O)₂ in future.

The single crystal X-ray diffraction is needed to reveal the accurate locations of adsorbed

CO₂, especially in CaSDB and SrSDB where two adsorption sites were observed.

As the next step, s-block metals-based MOFs need to be further explored with other organic ligands, which can help to build the systematic study on the s-block metals-based MOFs. Especially, with the involvement of other organic ligands, comparing the Mg coordination behavior with other s-block metals is one of the most significant projects.

Curriculum Vitae

Yihao Shen

Post-secondary Education and Degrees

University of Western Ontario

London, Ontario, Canada

HONOUR BACHELOR OF SCIENCE Sept. 2016 - June 2020

MASTER OF SCIENCE (CHEMISTRY) Sept. 2020 – Present

Research Experience

Department of Chemistry, University of Western Ontario

Working with Dr. Yining Huang's research group on the water effect on CO₂ adsorption behaviors within MOFs based on triazolate-BDC. Sept. 2019 - June 2020

Supervised by Dr. Yining Huang and studying the structure and gas sorption of s-block MOFs based on SDB ligand and UTSA-280. Sept. 2020 – Present

Related Work Experience

Zhejiang Tongyuan Co., Ltd

Zhejiang, China

Product development and Research assistant May 2019 – Aug. 2019

University of Western Ontario

London, ON

Teaching Assistant Sept. 2020 – June 2022

Summary of Course Work

CHEM9507Q: Advanced CHEM Communications (Quarter course, Fall 2020)

CHEM9754R: Powder Diffraction (Quarter course, Fall 2020)

CHEM9784S: Synchrotron Radiation and MAT. (Quarter course, Winter 2021)

CHEM9581R: Basics of Solid-State NMR (Quarter course, Fall 2021)

CHEM9541B: Crystallography I (Half course, Winter 2022)

Presentation

(Poster) "Studying the structure and CO₂ sorption of Metal-organic Frameworks based on s-block metals" 33rd MOOT NMR Conference. Guelph, ON. Oct.22-23, 2022.